

THESIS

COMPUTATIONAL ANALYSIS OF AIRCRAFT PRESSURE RELIEF DOORS

Submitted by

Tyler Schott

Department of Mechanical Engineering

In partial fulfillment of the requirements

For the Degree of Master of Science

Colorado State University

Fort Collins, Colorado

Summer 2016

Master's Committee:

Advisor: Xinfeng Gao

Co-Advisor: Stephen Guzik

Allan Kirkpatrick

Jianguo Liu

Copyright by Tyler Schott 2016

All Rights Reserved

## ABSTRACT

### COMPUTATIONAL ANALYSIS OF AIRCRAFT PRESSURE RELIEF DOORS

Modern trends in commercial aircraft design have sought to improve fuel efficiency while reducing emissions by operating at higher pressures and temperatures than ever before. Consequently, greater demands are placed on the auxiliary bleed air systems used for a multitude of aircraft operations. The increased role of bleed air systems poses significant challenges for the pressure relief system to ensure the safe and reliable operation of the aircraft. The core compartment pressure relief door (PRD) is an essential component of the pressure relief system which functions to relieve internal pressure in the core casing of a high-bypass turbofan engine during a burst duct over-pressurization event. The successful modeling and analysis of a burst duct event are imperative to the design and development of PRD's to ensure that they will meet the increased demands placed on the pressure relief system.

Leveraging high-performance computing coupled with advances in computational analysis, this thesis focuses on a comprehensive computational fluid dynamics (CFD) study to characterize turbulent flow dynamics and quantify the performance of a core compartment PRD across a range of operating conditions and geometric configurations. The CFD analysis was based on a compressible, steady-state, three-dimensional, Reynolds-averaged Navier-Stokes approach. Simulations were analyzed, and results show that variations in freestream conditions, plenum environment, and geometric configurations have a non-linear impact on the discharge, moment, thrust, and surface temperature characteristics. The CFD study revealed that the underlying physics for this behavior is explained by the interaction

of vortices, jets, and shockwaves. This thesis research is innovative and provides a comprehensive and detailed analysis of existing and novel PRD geometries over a range of realistic operating conditions representative of a burst duct over-pressurization event. Further, the study provides aircraft manufacturers with valuable insight into the impact that operating conditions and geometric configurations have on PRD performance and how the information can be used to assist future research and development of PRD design.

## ACKNOWLEDGEMENTS

I would like to thank Dr. Xinfeng Gao for providing me with an opportunity to work in the CFD and Propulsion Lab. Dr. Gao consistently challenged me to strive for the best and made me a better person because of it. I am grateful for my committee members, Dr. Stephen Guzik, Dr. Allan Kirkpatrick, and Dr. James Liu. You provided me with insightful questions and guidance along the way.

I would also like to thank the Boeing Company for their support of my research. In particular, Brad Olmstead, Ben Campbell, Jeff Harasha, and Kim Miller who provided invaluable support and guidance throughout the project. Without the support of Boeing and Boeing engineers, the project never would have been possible. I appreciate your patience, guidance, and allowing me to grow and learn as an engineer.

I would also like to thank the members of the CFD and Propulsion Lab for a number of entertaining lunch conversations and for providing the extra motivation to continue on. The friendships I gained will last a lifetime and I hope the traditions of “Lunch Club” and “Coffee Club” will continue on.

I am forever grateful to my family. They have supported me throughout this journey and motivated me to further my studies. My family has always been there for me, from the good times to the bad; they truly encouraged me to be the best that I could be.

## TABLE OF CONTENTS

Abstract .....	ii
Acknowledgements .....	iv
List of Tables .....	viii
List of Figures .....	ix
Chapter 1. Introduction .....	1
1.1. Background .....	1
1.1.1. Project Motivation .....	4
1.2. Thesis Layout .....	6
1.3. Literature Review .....	6
Chapter 2. RANS Modeling Approach .....	19
2.1. CFD++ Solver and Solution Methods .....	19
2.2. Compressible Reynolds Averaged Navier Stokes Equations .....	19
2.3. Realizable $k$ - $\epsilon$ Turbulence Model .....	22
2.4. Wall Functions .....	24
2.5. Convergence .....	25
2.6. Computational Resources and Costs .....	25
2.7. Post Processing .....	26
2.7.1. Post Processing Calculations .....	27
2.7.1.1. Minimum Geometric Flow Area .....	28
2.7.1.2. Discharge Coefficient .....	28
2.7.1.3. Effective Area .....	29

2.7.1.4.	Corrected Mass Flow Rate.....	30
2.7.1.5.	Discharge Flow Ratio.....	30
2.7.1.6.	Hinge Moment Coefficient.....	30
2.7.1.7.	Thrust and Lift Coefficient.....	31
2.7.1.8.	Average Wall Temperature.....	31
2.7.1.9.	Non-dimensional High Temperature Area.....	32
Chapter 3.	Modeling of Pressure Relief Door.....	33
3.1.	Physical Component Geometries and Configurations.....	33
3.1.1.	Modeling Challenges.....	38
3.2.	Boundary Conditions.....	40
3.3.	Computational Grids.....	43
3.3.1.	Background Grid.....	44
3.3.2.	Door Grid.....	45
3.3.2.1.	Grid Metrics.....	49
3.3.2.2.	Door Grid Challenges.....	49
3.4.	Grid Refinement.....	50
Chapter 4.	Results and Discussion.....	55
4.1.	Comprehensive Parameter Study Hinge Type Comparison.....	55
4.1.1.	Hinge Moments.....	56
4.1.2.	Hinge Moment Equilibrium.....	63
4.1.3.	Exit Mass Flow Rate.....	67
4.1.3.1.	Minimum Geometric Flow Area.....	75
4.1.3.2.	Discharge Coefficient.....	76

4.1.3.3. Effective Flow Area .....	84
4.1.3.4. Mass Flow Rate Distribution .....	88
4.1.4. Thrust .....	103
4.1.5. Surface Temperature .....	106
4.1.5.1. Non-dimensional High-Temperature Area .....	107
4.1.6. Flow Structure .....	117
4.2. Geometric Comparison Study .....	127
4.2.1. Gooseneck-hinge Geometric Comparison .....	127
4.2.2. Mid-hinge Geometric Comparison .....	132
4.2.3. Piano-hinge Geometric Comparison .....	140
Chapter 5. Conclusions and Future Work .....	150
5.1. Conclusions .....	150
5.1.1. Moments .....	150
5.1.2. Discharge .....	150
5.1.3. Thrust .....	151
5.1.4. Surface Temperature .....	152
5.2. Future Work .....	153
Bibliography .....	154

## LIST OF TABLES

3.1	Boundary conditions corresponding to Figure 3.7 and Figure 3.8.....	42
3.2	Mass flow rate comparison for grid refinement study.....	53
3.3	Hinge moment comparison for grid refinement study.....	54
3.4	Door force comparison for grid refinement study.....	54
4.1	Details of comprehensive parameter study.....	56

## LIST OF FIGURES

1.1	Pressure relief door locations [2].....	1
1.2	On engine PRD with latch and hinge mechanism visible [3] (left) and bleed air duct separation (right) [2].....	2
1.3	Core compartment pressure relief doors on a Boeing 777 (left) and Boeing 787 (right) [4, 5].....	3
1.4	Schematic of test fixture used in NACA TN4007 [6]. ....	9
1.5	Computational domain used in Pratt et al. studies [12].....	11
1.6	Pratt et al. result of Mach number contours on symmetry plane [12].....	13
1.7	Comparison of rectangular and trapezoidal geometry [20].....	16
1.8	Geometric pressure relief door geometry and non-dimensional temperature comparison presented in a patent awarded to Balzer in 1997 [20].....	17
2.1	Total temperature contours on bottom wall of freestream domain with contour line of temperatures greater than 400 °F indicated. ....	32
3.1	Symmetry plane view of the computational domain.....	34
3.2	Hinge type comparison.....	35
3.3	Hinge type comparison for vertical hinge offset. ....	36
3.4	Geometrical configurations of Goosneck-hinge type. ....	37
3.5	Geometrical configurations of Mid-hinge type.....	38
3.6	Piano-hinge geometries compared. ....	39
3.7	Isometric view of computational domain.....	41

3.8	Isometric view of internal mass flow surfaces; leading edge (green), lateral edge (orange) and trailing edge (purple).....	41
3.9	Multi-block grid approach with door block (red) and multi-block structured background grid.....	44
3.10	Symmetry plane grid coarsening strategy.....	45
3.11	Structured surface grids on door.....	47
3.12	Symmetry plane door block grid detail.....	48
3.13	Refinement study comparison of Mach contours on symmetry plane of trailing edge jet.....	51
3.14	Refinement study comparison of total temperature contours on freestream bottom wall.....	52
4.1	Total hinge moment comparison for Gooseneck-hinge (square) and Mid-hinge (diamond) types for variations in freestream, plenum, and geometric configurations.	57
4.2	Total pressure contours comparing the Gooseneck-hinge and Mid-hinge geometries on the symmetry plane at a door angle of 30° and baseline operating conditions. .	59
4.3	Total moment equilibrium angle comparison for Gooseneck-hinge and Mid-hinge types.....	64
4.4	Exit mass flow rate comparison for Gooseneck-hinge and Mid-hinge types.....	68
4.5	Contours of Mach number on the symmetry plane for variations in freestream altitude at 30 ° for Mid-hinge type. Note the dashed black contour line of $Ma_\infty = 1$ .....	70

4.6	Contours of static pressure on the symmetry plane for variations in door angle at a freestream altitude of 45,000 ft. for Mid-hinge type. Note the dashed black contour line of $Ma_\infty = 1$ . . . . .	72
4.7	Streamlines colored by total temperature for freestream Mach number variation at $15^\circ$ for Gooseneck-hinge type. . . . .	73
4.8	Area comparison for Gooseneck-hinge and Mid-hinge types, minimum geometric flow area is limited by door opening area. . . . .	76
4.9	Discharge coefficient comparison for Gooseneck-hinge and Mid-hinge types. . . . .	77
4.10	Comparison of streamlines colored by total temperature for freestream $Ma_\infty = 0.9$ and $45^\circ$ door angle observed from the symmetry plane for Gooseneck-hinge and Mid-hinge types. Note the variation in leading edge flow behavior. . . . .	81
4.11	Effective area comparison for Gooseneck-hinge and Mid-hinge types. . . . .	85
4.12	Leading edge mass flow rate comparison for Gooseneck-hinge and Mid-hinge types. . . . .	89
4.13	Leading edge reverse massflow distribution comparison for Gooseneck-hinge and Mid-hinge types. . . . .	92
4.14	Lateral edge mass flow distribution comparison for Gooseneck-hinge and Mid-hinge types. . . . .	95
4.15	Trailing edge relative mass flow distribution comparison for Gooseneck-hinge and Mid-hinge types. . . . .	98
4.16	Lateral to trailing equilibrium comparison for Gooseneck-hinge and Mid-hinge types. . . . .	101
4.17	Thrust coefficient comparison for Gooseneck-hinge and Mid-hinge types. . . . .	104

4.18	Comparison of total temperature contours on bottom wall surface for Gooseneck-hinge type baseline case. Note the black contour line corresponds to temperatures greater than 400°F. ....	107
4.19	Comparison of total temperature contours on symmetry plane at 30 ° for Gooseneck-hinge and Mid-hinge type baseline case.....	108
4.20	Non-dimensional high surface temperature area comparison for Gooseneck-hinge and Mid-hinge types. ....	109
4.21	Comparison of streamlines colored by total temperature (left) and total temperature contours (right) for Mid-hinge type at 15 ° for variation in freestream altitude. ....	110
4.22	Comparison of streamlines colored by total temperature (left) and total temperature contours (right) for Gooseneck-hinge type at 15 ° for variation in freestream Mach number. ....	112
4.23	Comparison of total temperature contours for Gooseneck-hinge type at 30 ° for variation in plenum pressure; bottom wall view (top) symmetry plane (bottom)...	113
4.24	Comparison of total temperature contours on bottom wall for variation in door aspect ratio at 15 ° for Mid-hinge type.....	115
4.25	Comparison of total temperature contours and streamlines colored by total temperature for Gooseneck-hinge type at 15 ° for variation in vertical hinge offset.	116
4.26	Contours of Mach number on the symmetry plane view for baseline Gooseneck-hinge 45 ° case. ....	118

4.27	Contours of Mach number for door angles ranging from 15-60°, baseline case, Gooseneck-hinge type. ....	119
4.28	Contours of total pressure for Gooseneck-hinge type at 30 ° and 60 °. ....	120
4.29	Contours of Mach number for door angles ranging from 15-60°, baseline case, Mid-hinge type. ....	121
4.30	Streamlines colored by total temperature for baseline Gooseneck-hinge and Mid-hinge geometries at 15 °. ....	122
4.31	Streamlines colored by total temperature for baseline Gooseneck-hinge 15 ° geometry observed from symmetry plane. ....	123
4.32	Detailed slice view of streamlines colored by total temperature at varying mid-plane slices for 15 deg door angle Gooseneck-hinge type with view looking upstream. ...	124
4.33	Streamlines colored by total temperature for varying door angle for Gooseneck- hinge hinge with views looking downstream (left) and upstream (right). ....	125
4.34	Detailed comparison views of streamlines colored by total temperature for varying door angle for Gooseneck-hinge type. Slice view observed looking upstream from a slice 12.5 in. downstream of the trailing edge opening (left) and symmetry plane view (right). ....	126
4.35	Surface temperature comparison plots for Gooseneck-hinge types. ....	127
4.36	Total temperature contours for 15° (left) and 45° (right) Gooseneck-hinge geometric hinge type comparison. ....	129
4.37	Streamlines colored by total temperature for comparison of Gooseneck-hinge type square corner geometry at 15 ° door angle. ....	131

4.38	Gooseneck-hinge geometric comparison of discharge, thrust, and moment characteristics.....	133
4.39	Gooseneck-hinge geometric comparison of relative mass flow rate distribution.....	134
4.40	Surface temperature comparison plots for Mid-hinge types.....	135
4.41	Total temperature contours for 15 ° (left) and 45 ° (right) Mid-hinge geometric hinge type comparison. ....	137
4.42	Streamlines colored by total temperature for 15 ° door angle for Mid-hinge type geometric embodiments for views looking downstream (top) and from symmetry plane (right). ....	139
4.43	Mid-hinge geometric comparison of discharge, thrust, and moment characteristics.	141
4.44	Mid-hinge geometric comparison of relative mass flow rate distribution. ....	142
4.45	Surface temperature comparison plots for Piano-hinge types.....	143
4.46	Streamlines colored by total temperature for 15 ° door angle for Piano-hinge type geometric embodiments for views looking downstream (left) and upstream (right).	145
4.47	Total temperature contours for 15 ° (left) and 45 ° (right) Piano-hinge geometric hinge type comparison. ....	147
4.48	Piano-hinge geometric comparison of discharge, thrust, and moment characteristics.	148
4.49	Piano-hinge geometric comparison of relative mass flow rate distribution.....	149

# CHAPTER 1

## INTRODUCTION

### 1.1. BACKGROUND

Aircraft manufacturers are striving to develop innovative and cutting edge techniques to improve specific fuel consumption and emissions while keeping a strong focus on reliability and safety of the aircraft. The advancement of high-performance modern turbine aircraft engines places significantly greater demands on auxiliary air systems to maintain reliable and safe operation. An essential component of the auxiliary airflow system is the pressure relief door (PRD). In the event of a burst duct scenario, high-pressure and high-temperature gases from the auxiliary air lines over pressurize the engine under cowling as shown in Figure 1.1. Multiple PRD's function to relieve those internal pressures to prevent structural damage or failure to the nacelle structure. The FAA requires PRD's for aircraft certification under FAR 25.1103 [1].

The advancement of aircraft engines has placed a greater demand on the operation and design of PRD's for aerospace applications. Pressure relief doors are used in various capacities in multiple locations on an aircraft including the fuselage, struts, nacelle casing, and engine shroud as shown in Figure 1.1.

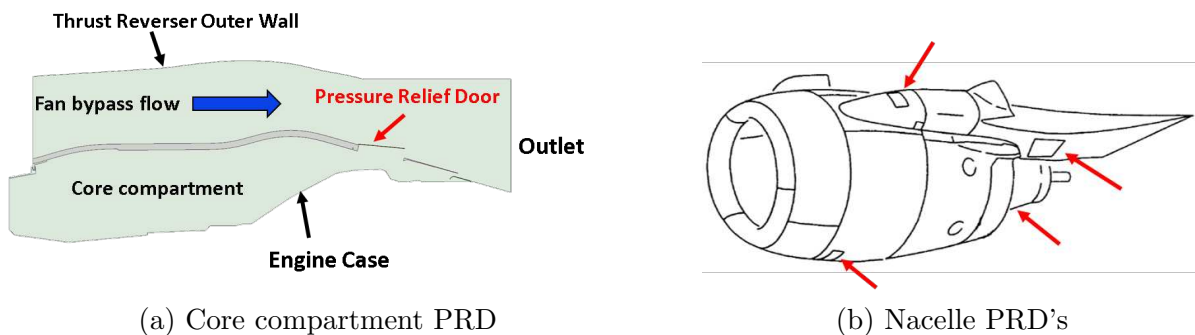


FIGURE 1.1. Pressure relief door locations [2].

The design of PRD's has remained relatively unchanged since the 1960's; a spring loaded rectangular door with a rectangular opening that opens when a predetermined differential pressure is encountered. When the door opens, transient flow dynamics settle out, and the resultant flow phenomenon observed results in complex three-dimensional flow dynamics characterized by vortices, jets, and shockwaves. The development of these flow features and door behavior is dependent on the geometrical configuration of the door, core compartment environment, and freestream conditions. This thesis work focuses on the core compartment PRD which presents a unique challenge; to relieve internal pressure to prevent an over-pressurization event and to withstand high-temperature gases escaping through the PRD. High-temperature gases, on the order of 1200°F, can remain attached to the surface surrounding the door opening necessitating expensive and heavy high-temperature materials or thermal blankets to prevent a compromised core compartment structure. The work aims to characterize PRD performance to gain a deeper understanding of PRD behavior to assist the aircraft manufacturer for future PRD design.

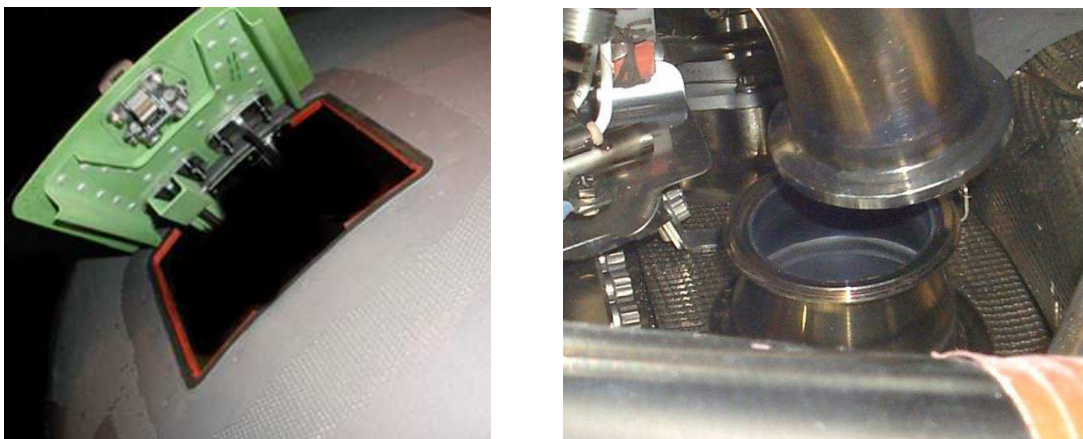


FIGURE 1.2. On engine PRD with latch and hinge mechanism visible [3] (left) and bleed air duct separation (right) [2].

The goal of this research is to improve current knowledge of PRD characteristics by determining discharge, moment, thrust, and surface temperature characteristics across a wide range of flow parameters and door designs through a comprehensive three-dimensional, steady-state, CFD analysis. The study aims to contribute a body of knowledge regarding core compartment PRD behavior to the aerospace community as there has been minimal published research surrounding experimental and computational studies of PRD's. Aircraft designers have historically taken a conservative approach in developing pressure relief systems. While these designs have not seriously impacted aircraft performance, the cumulative effect of many PRD's discharging large volumes of air may have a pronounced impact on the performance of the aircraft. Modern aircraft operate at significantly higher pressures and temperatures compared to aircraft developed in the 1950's. Consequently, greater demands are placed on auxiliary airflow systems resulting in an increased role of PRD's for safe aircraft operation.



(a) 777 PRD



(b) 787 PRD

FIGURE 1.3. Core compartment pressure relief doors on a Boeing 777 (left) and Boeing 787 (right) [4, 5].

1.1.1. PROJECT MOTIVATION. Pressure relief doors are imperative to the operational safety and reliability of an aircraft. Accurate modeling and simulation are essential to the design and development of PRD's. Minimal published research exists examining realistic operating conditions and geometric configurations. The primary experimental investigation, which featured unrealistic flow conditions and geometric configurations, was performed by Vick in 1957 [6] and recreated computationally by Pratt et al. in 2003 [7]. Developing an experimental test fixture is prohibitively expensive and can only provide a glimpse of the resulting flow. Current industry practice in developing PRD's relies on a highly simplified quasi-1D code that fundamentally ignores the complexities and non-linearities associated with PRD performance. The lack of experimental and computational studies of PRD behavior motivated the work presented in this thesis. The three-dimensional comprehensive CFD study allows for realistic operating conditions and geometric configurations indicative of a burst duct event to be simulated. Furthermore, a detailed analysis of the discharge, moment, thrust, and surface temperature characteristics and the ability to visualize and characterize the complex flow dynamics associated with PRD operation make the work in this thesis foundational to future PRD research and development. The work presented in this thesis was just one part of a larger program for an aircraft manufacturer to improve the modeling and simulation of PRD behavior.

Pressure relief doors are used in numerous locations on an aircraft. This thesis primarily focused on the core compartment PRD, but data obtained from the analysis applies to PRD's used in other places on the aircraft. A rectangular freestream and plenum domain was specified to isolate the impact of operating conditions and geometric configuration on the resulting flow characteristics. Typical on-engine PRD geometry varies depending on

engine requirements as shown in Figure 1.3. The comprehensive study analyzed a rectangular shaped door with one-inch rounded corners for door angles from  $0^\circ$  to  $60^\circ$  in  $15^\circ$  increments. The broad range of door angles was chosen to accurately obtain the equilibrium moment angle where the door achieves a trimmed balance. Three PRD hinge locations were examined. The Gooseneck hinge type pivots around a hinge upstream of the leading edge of the door opening while the Midhinge hinge type pivots around a hinge downstream of the leading edge of the door opening. A third hinge location was explored that pivoted at the leading edge of the door opening denoted as “Pianohinge” hinge type, though it is not commonly used. The Gooseneck and Midhinge hinge types are the most commonly used in current on-engine configurations and were the primary focus of the comprehensive study. The study investigated door aspect ratios from 0.75 to 1.5 and vertical hinge offsets from 0 to 0.75-inches. An additional study presented in this thesis examines the impact of geometric features including door shape, corner rounding, hinge type, and the addition of lateral edge fence on the wall temperature characteristics associated with the PRD opening. The comprehensive study investigated variations in both freestream and plenum conditions representative of what a typical commercial aircraft may encounter. Freestream pressure altitudes ranged from -2000 feet to 45,000 feet and Mach numbers ranged from 0 to 0.9. Bleed air is extracted at numerous location in the compressor stages; thus a wide range of bleed air pressure and temperatures exist. Plenum gage pressures varied from 1 psig to 12 psig and plenum temperatures from  $-80^\circ\text{F}$  to  $1500^\circ\text{F}$  were investigated. Previous studies [6, 7] only examined negative plenum gage pressures, making for difficult comparisons to a burst duct over-pressurization event. For all of the cases investigated, only a single parameter was varied to isolate the impact of that parameter on the solution. The extraction of

steady state data at a given angle allowed for PRD performance to be characterized across a wide range operating conditions and geometric configurations independent of the typically transient flow behavior.

## 1.2. THESIS LAYOUT

This thesis is composed of five chapters. Chapter 1 provides an introduction and background related to PRD's including a comprehensive literature review exploring experimental and computational studies and related patents. Chapter 2 provides a thorough overview of the fundamental equations of the computational model including the RANS equations, realizable  $k$ - $\epsilon$  turbulence model, and the primary elements of the finite-volume method (FVM) solver. Chapter 3 discusses the details of the geometric modeling, boundary conditions, grids, refinement study, and case setup. Chapter 4 presents results and in-depth discussion of the comprehensive parameter study and the geometrical configuration study. Chapter 5 presents final conclusions and an outline for future work.

## 1.3. LITERATURE REVIEW

Minimal experimental or computational work has been performed regarding the discharge and force characteristics of PRD's. Several studies carried out by NACA experimentally investigated auxiliary outlets, flapped outlets, and general discharge characteristics for generalized airflow systems. Current PRD research has aimed to experimentally and computationally recreate experiments developed by NACA for validation purposes. There has been minimal published academic work mainly due to the competitive and classified nature of the aerospace industry; however, several patents provide insight into the developments of PRD design.

The advancement of the aerospace industry during the 1940's was primarily driven by the push to develop aircraft for World War II. Several experimental investigations aimed to develop a database of knowledge for aircraft designers. In 1941, Rogallo et al. published "Internal-flow systems for aircraft," [8] which briefly covered several experimental analyses of internal airflow systems in a NACA 5-foot vertical wind tunnel. Rogallo investigated "adjustable-flap openings in a flat plate" and performed a simple analysis on a piano-hinge, opposite hinged-piano, and dual hinge piano configuration. The experimental setup consisted of 1/16" plate and a door with a 1.5" chord length at door angles of 15°, 30°, and 45°. The limited study only examined two cases, with free stream velocities of 40 mph and 80 mph. The 80 mph case was only investigated at 30°. The primary conclusions from Rogallo indicated that the "skin friction on the plate behind the opening would tend to increase drag with the flow coefficient," where the flow coefficient was defined as  $\frac{Q}{AV}$  where  $Q$  is the volumetric flow rate,  $A$  is the area, and  $V$  is the free stream velocity. The work Rogallo performed provided a basis to further investigate the performance of outlets for internal aircraft flow systems.

A research program was developed to experimentally determine the discharge coefficients and drag characteristics of auxiliary air outlets in the 1950's. Dewey initially examined the aerodynamic characteristics of small inclined air outlets exhausting into transonic freestream Mach numbers [9] where it was determined that inclined outlets tended to have higher discharge coefficients than those perpendicular to the air stream. Freestream Mach number was shown to have minimal impact on the discharge coefficient at constant values of discharge flow ratio (DFR) defined as  $\frac{\dot{m}}{\rho AV}$ .

A subsequent study carried out by Dewey and Vick examined thin plate and ducted outlets [10]. The thin plate outlets examined various geometrical shapes including circular, elliptical, and varying aspect ratio rectangular outlets. It was determined that the discharge coefficient for rectangular thin-plate outlets decreased with increasing aspect ratio, where aspect ratio was defined as  $\frac{t^2}{A}$  where  $t$  = throat width and  $A$  is the throat area. The ducted outlet study investigated inclination, curvature, and recessed depth configurations. As discovered in the previous Dewey study, varying freestream Mach had minimal impact on the discharge coefficients of flush ducted outlets. Interestingly, the recessed outlets tended to have higher discharge coefficients due to the difference in exit static pressure and the ambient pressure. Inclined and curved outlets preconditioned the flow to discharge nearly parallel to the freestream flow thereby promoting greater discharge coefficients at lower DFR values. The thin-plate and ducted outlet research provided a basic test procedure and database to draw upon when investigating flapped outlets.

In 1957, Vick experimentally determined discharge and thrust characteristics for flush curved ducted flapped air outlets discharging into a transonic freestream [6]. The study investigated flap angle, hinge location, and aspect ratio, across a range of duct pressure variations and freestream Mach numbers. The study has been the most comprehensive analysis of flapped outlets and has proven to be the foundational experimental research surrounding PRD's.

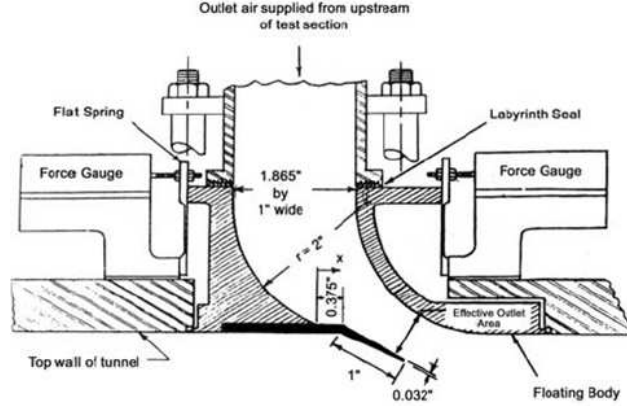


FIGURE 1.4. Schematic of test fixture used in NACA TN4007 [6].

The experimental test fixture built upon the same transonic wind tunnel employed by Dewey and Vick [9]. The plenum chamber was connected to a vacuum pump below a slotted wall, where a flap projected downward from the top wall of the tunnel as seen in Figure 1.4. The secondary plenum air entered the rectangular duct that curved  $90^\circ$  in a circular arc before exhausting through the flapped outlet to the primary freestream air. The preconditioned nature of the air exiting the flapped outlet is a concern when using the results to develop PRD's, where a core casing over-pressurization event would likely not have a curved or ducted exhaust flow. The mass flow rate to the plenum was metered upstream of the rectangular inlet and a force dynamometer measured force characteristics on the flap. The results of the study indicated that at a flap angle of  $0^\circ$ , a non-zero mass flow rate existed, due to a gap between the flap tip and the top wall of the test fixture. The larger exit area likely contributed to potential error in the analysis. The results of the study primarily looked at the discharge flow ratio, defined as  $DFR = \frac{\dot{m}}{\rho AV}$  where  $\dot{m}$  is the exit mass flow rate,  $\rho$  is the freestream density,  $A$  is the minimum cross sectional area between the downstream end of the flap and the outlet wall, and  $V$  is the freestream velocity. The minimum cross-sectional area assumed two-dimensional flow behavior and neglected air that

exhausted out of the lateral edges of the flapped outlet. This assumption provided a potential source of error in calculating exit mass flow rate, particularly at higher door angles.

Vick concluded that the total-pressure ratio required to attain a given DFR decreased markedly with increasing door angle and varied strongly with freestream Mach number. The lower pressure regions created aft of the flap opening promotes greater flap suction and thus greater exiting mass flow. It was concluded that as the hinge point moved rearward, DFR values were shown to increase at a fixed door angle and pressure ratio. Flaps of aspect ratio one were shown to produce better discharge characteristics than those of aspect ratio equal to two, due to the higher aspect ratio doors having a shorter chord and less exposed flap in the higher velocity freestream flow. However, the higher aspect ratio doors were shown to have a higher thrust coefficient. It was also determined that the apparent thrust generated by the flapped outlet exhaust air was greater than that calculated from the momentum of the exhaust air. The increase in thrust is due in large part to the exiting jet acting on the flap.

While the study performed by Vick provided valuable insight into thrust and discharge characteristics of flapped outlets, the experimental model did not accurately model a core casing over-pressurization event. The flow was highly preconditioned as it was exhausted through the curved duct and a significant gap existed between the flap tip and the closing door of the wall resulting in skewed results. In a core casing over-pressurization event, it is unlikely that the flow will maintain a constant inlet velocity similar to what was specified in the study. The over-pressurization event will likely feature highly transient flow dynamics that will eventually settle out and reach equilibrium. The preconditioned nature of the exhaust flow limits the exiting flow to a two-dimensional behavior when in reality the

exhaust flow is a fundamentally three-dimensional event. The study neglected to discuss flow structures formed around or downstream of the flap opening and minimal discussion was provided to the PRD designer in considering door angle, hinge type, door type, pressure ratio, or Mach number. The results of the study were summarized in a report by Young et al. in 1981 [11], highlighting that door angle, aspect ratio, and door area were important factors in the design of protruding outlets. The Vick study provided a comprehensive experimental analysis of flapped outlets that provided the fundamental basis of future computational and experimental analysis by Pratt et al. and Benard et al.

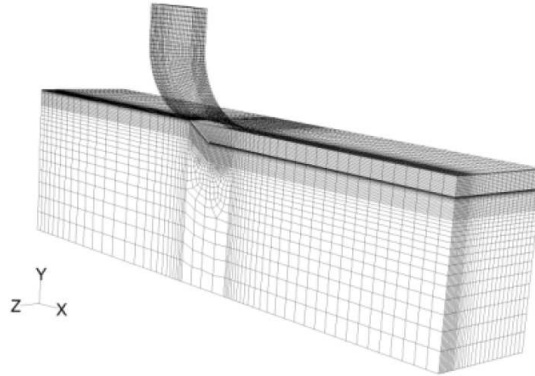


FIGURE 1.5. Computational domain used in Pratt et al. studies [12].

Pratt et al. sought to computationally recreate the results presented by Vick in NACA TN4007 as described in two papers published in 2003 and 2004, [7, 3]. The study aimed to gain better insight into the performance and associated flow physics of flapped outlets presented in the 1957 Vick study [6]. The computational model was developed with the notion that it could be validated with the experimental results presented by Vick. The parameter study analyzed varying freestream Mach number from 0.4–0.85, varying the total pressure ratios between 0.64–0.97, and door angles between  $15^\circ$  and  $45^\circ$ . The computational

domain was designed to simulate the transonic wind tunnel presented in NACA TN4007, assuming a fixed flap angle and a flap with negligible weight. The computational grid, developed in Gambit, comprised of both structured and unstructured elements as shown in Figure 1.5. A bulk of the grid was structured except for in the region near the flap outlet where an unstructured grid was used due to intolerable levels of skew. The grid size was around 160,000 elements with  $y_1^+$  values between 30–60 at the cell centers.

The computational analysis was performed in ANSYS Fluent 6 and used a steady state, compressible, RANS, unstructured finite volume method solver that employed the SIMPLE pressure-velocity coupling algorithm and a second order upwinding discretization scheme. The realizable  $k$ - $\epsilon$  turbulence model was used with standard wall functions. The primary and secondary (plenum) inlets were specified as pressure inlets while the outlet was specified as a pressure outlet. The analysis took advantage of the symmetry condition as the mid-plane was defined as a symmetry plane. The computational analysis was in good agreement with the experimental analysis presented in NACA TN4007. The computational analysis tended to under-predict the DFR by 5–20% while the thrust coefficient was typically over-predicted. It was concluded that a pair of longitudinal vortices were shed from the edges of the flap and interacted with a strong jet from exhausting from the flapped outlet.

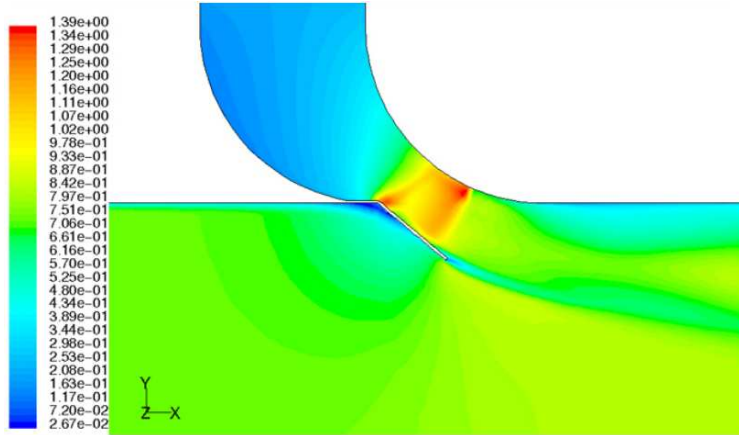


FIGURE 1.6. Pratt et al. result of Mach number contours on symmetry plane [12].

The strength of the vortices increased with increasing angle until a maximum angle was reached, after which flow separated and had minimal impact on the size and strength of the vortices. Smaller flap angles resulted in a thinning effect on the boundary layer downstream of the outlet due to the interaction of the vortices with the exhaust flow jet. The flow features generated were dependent on flap angle, pressure ratio, and freestream Mach number. It was noted that at certain conditions, a normal shock would develop and consequently choke the flow of air exiting the flapped outlet. DFR was shown to increase with increasing door angle until a maximum was reached and then began to fall with increasing angle. The optimal door angle to achieve DFR was shown to increase with greater freestream Mach number and decreased with increasing pressure ratio. The behavior was attributed to the vortex pair created downstream of the door. The equilibrium pitching moment defined as the point where the flap achieves a trimmed balance, was determined to lay in the range of  $10^\circ - 15^\circ$  for all cases. An increase in Mach number reduced the equilibrium angle while increased pressure ratio increased it.

In 2008, a research program at the Queens University of Belfast lead by Benard et al. [13] was set up to expand upon the experimental database presented in NACA TN4007

[6]. The work was an extension of the computational analysis performed by Pratt in 2003 [12] which provided the foundational knowledge for developing a test fixture to model a wider array of cases. The experimental investigations employed a similar test fixture to that presented in NACA TN4007, however, a transonic suckdown tunnel that featured a cavity beneath the pressure relief orifice was used. The experimental work was limited to a freestream Mach=0.7, to minimize blockage effects, and primarily investigated stagnation pressure ratios greater than one. The paper provides a vague description of the results from the experimental analysis but concludes that discharge coefficients decreased with increasing flap angles at a given pressure ratio. Benard attributes the behavior to the interaction of flow dynamics. It was also concluded that DFR increased linearly at a given flap angle and freestream Mach number. A subsequent experimental analysis was presented by Vedeshkin et al. in 2012 [14] related to PRD's. The paper provided a thorough description of a test fixture to analyze aerodynamic forces and discharge coefficients of piano hinge PRD's and vented outlets. Results of the paper were vague and did not provide any beneficial results other than an overview of the development of an experimental test fixture to analyze the performance of PRD's.

The aerospace industry is highly competitive and often conservative in publishing results. The work performed by Benard in 2008 [13] was supported by Bombardier Aerospace while the work by Vedeshkin et al. [14] and Verseux et al. [15] was sponsored by Airbus. To gain a better understanding of PRD's, several patents related to PRD's were investigated. In 1956, Siems, on behalf of Boeing, patented the concept of "blowout safe aircraft doors" [16]. The patent discussed methods to prevent aircraft doors from opening too far resulting in structural damage and the concept of redundant latches to minimize unintended door

openings. While the patent did not directly target PRD's, the same technology is employed to prevent doors from exceeding a maximum opening angle. Pressure relief doors often provide multiple functions; not only for pressure relief capabilities but also as an access opening for routine maintenance checks. Abeel patented this concept in 1971 [17]. The patent also covered a dual function latch mechanism that would open when a predetermined differential pressure was met or with an external tool like a screwdriver.

Pressure relief door assemblies are comprised of a multitude of parts including the door, door springs, latch, and latch mechanism thus an opportunity exists to develop an alternative approach for pressure relief functions. In 1980, Pearson patented the concept of a pressure relief composite disc that would break into several pieces when a specified differential pressure was achieved [18]. While the idea is good in theory, developing a reliable high-temperature composite disc that can withstand high core casing temperatures yet is fragile enough to break consistently when a differential pressure is met, is a challenge. The frangible disc would break into several small pieces would prove to be a concern for potential ingestion into the engine.

In 1989, Bubello patented the concept of a ventilation system for a nacelle [19]. The patent highlighted the need to have ventilation systems for turbofan engines that included pressure relief doors and mechanisms to limit the maximum door opening yet prevent the door from closing after it had been opened to provide a visual indication that there was a problem in the nacelle [19]. It was indicated that the optimum door opening was at  $40^\circ$  for what is assumed to be a Pianohinge hinge type, though the actual hinge type was not specified. The primary patent regarding PRD door design was published in 1997 by Balzer [20]. The primary invention in the patent was a trapezoidal door geometry as depicted in

Figure 1.7b. The patent suggested that the wider leading edge of the trapezoidal geometry allowed for cool bypass air to flow more closely to the lateral edges of the door opening compared to a rectangular shaped door as illustrated in Figure 1.7. The altered airflow associated with the trapezoidal geometry allows for improved thermal mixing and reduced high-temperature contact area downstream of the door.

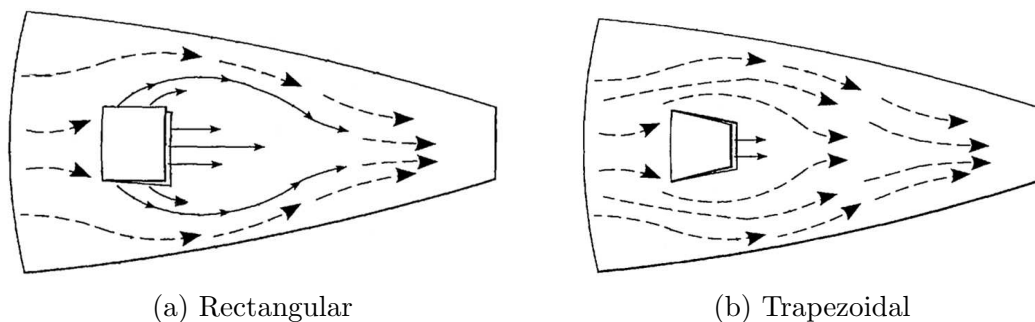


FIGURE 1.7. Comparison of rectangular and trapezoidal geometry [20].

The inventions presented in the patent suggest that the addition of lateral fences function to redirect flow rearward so that a large volume of engine gases exit out of the trailing edge of the cutout and consequently improve wall surface temperatures. The fence geometry is a wall that extends between the bottom lateral surface of the door and the top of the core casing wall and greater than 50% of the door length. Figure 1.8a provides a comparison of three geometric embodiments presented in the patent where Fig. 4A and 4B correspond to a rectangular door with lateral edge fences, Fig. 5A and 5B correspond to a trapezoidal geometry with no fences, and Fig. 6A and 6C correspond to a trapezoidal geometry with lateral edge fences. A non-dimensional temperature plot shown in Figure 1.8b compares the downstream wall surface temperatures for four geometric embodiments; line 39 corresponds to a rectangular door with no fences, line 50 corresponds to the rectangular door with fences as shown in Fig. 4A and 4B, line 52 corresponds to a trapezoidal door with no fences as

shown in Fig. 5A and 5B, and line 54 corresponds to the trapezoidal geometry with fences as shown in Fig. 6A and 6B. The patent suggests that the addition of lateral edge fences dramatically reduces the wall surface temperatures. The trapezoidal geometry with lateral fences provided the best result for downstream wall surface temperatures. Details of the experimental test fixture were not presented in the patent and locations of data extraction were also not provided. The Balzer patent motivated further study of novel PRD designs that is discussed in this thesis.

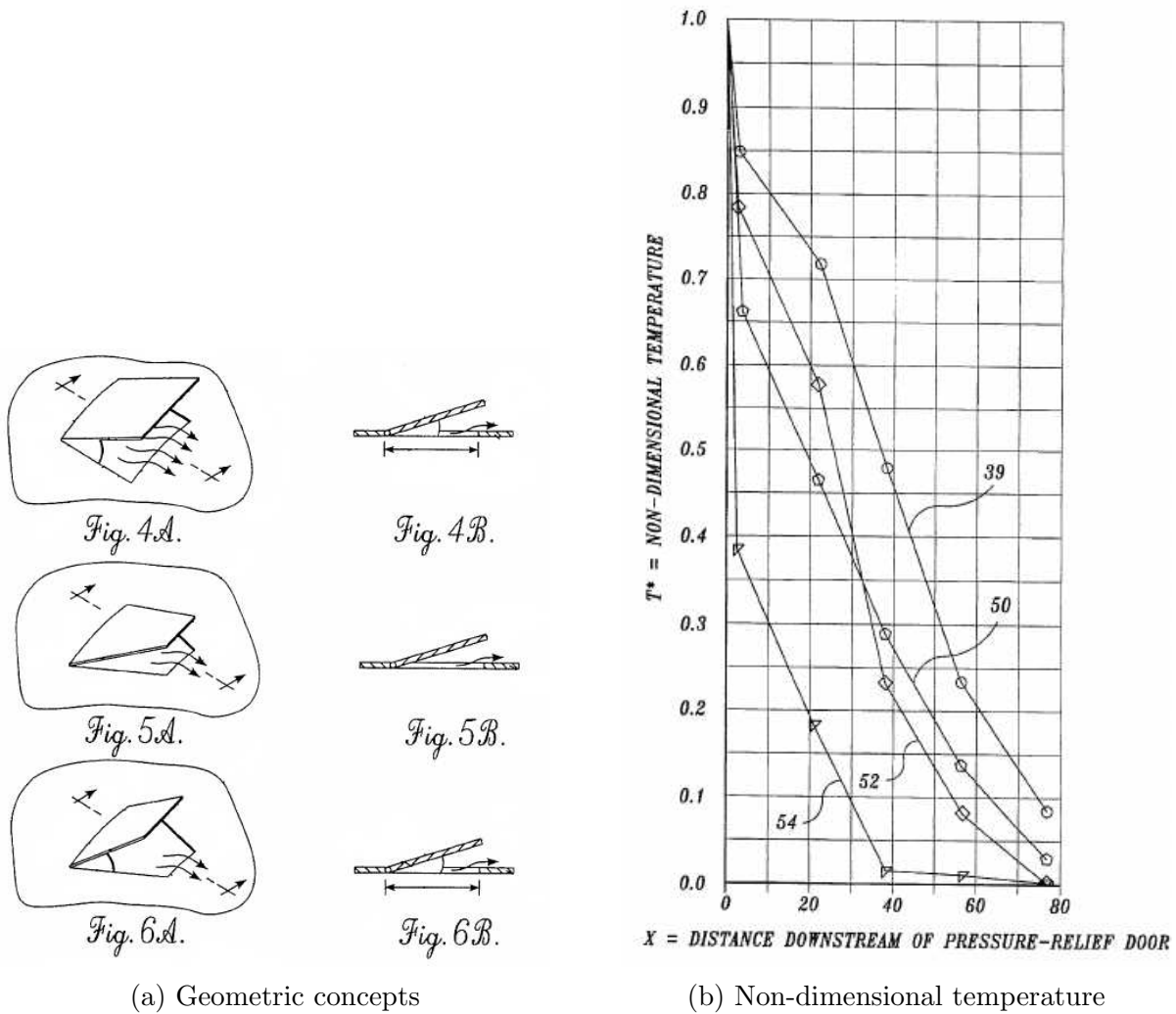


FIGURE 1.8. Geometric pressure relief door geometry and non-dimensional temperature comparison presented in a patent awarded to Balzer in 1997 [20].

Armstrong patented the concept of a novel design of a spring loaded PRD where dual canister springs are attached to the PRD; the patent was awarded in the US in 2013 [21] and in Europe in 2012 [22]. Tuchimaa patented the concept of a pressure management system which broadly applied to PRD behavior in 2014 [23].

Minimal published research has been performed in the realm of PRD's. Many studies carried out by NACA in the 1950's aimed to characterize discharge and thrust characteristics of various outlets, with the primary experimental analysis of flapped outlets presented by Vick in NACA TN4007. A computational analysis was carried out by Pratt et al. in 2003 to recreate the experimental results of NACA TN4007, which provided a look at the complex flow physics associated with flapped outlets. Further experimental analyses aimed to improve the understanding of PRD behavior but provided minimal contributions to the existing body of literature. Very little has been published concerning a core casing over-pressurization event with appropriate boundary conditions and flow conditions. This thesis to develop a computational model to investigate the complex flow phenomenon of modern PRD behavior using realistic boundary conditions to accurately model a burst duct event. This thesis research is innovative and provides a comprehensive and detailed analysis of existing and novel PRD geometries over a range of realistic operating conditions representative of a burst duct over-pressurization event. Further, the study provides aircraft manufacturers with valuable insight into the impact that operating conditions and geometric configurations have on PRD performance and how the information can be used to assist future research and development of PRD design.

## CHAPTER 2

# RANS MODELING APPROACH

### 2.1. CFD++ SOLVER AND SOLUTION METHODS

The commercial CFD solver CFD++ [24], version 15.1, from Metacomp Technologies was used in this study. The cell centered finite-volume method was used to solve the three-dimensional, compressible Reynolds-averaged Navier-Stokes equations (RANS). A brief review of the compressible RANS modeling approach is discussed in Section 2.2 The steady state solution was obtained using a point implicit time integration scheme with local time-stepping. Convergence was accelerated using a multi-grid W-cycle method with a maximum of 4 cycles and a maximum of 20 grid levels. Temporal smoothing was used to increase solution stability, particularly with strong transients. Inviscid fluxes were handled by a second-order accurate, upwind scheme that used the Harten-Lax-van Leer-Contact (HLLC) approximate Riemann solver with a multi-dimensional continuous Total-Variation-Diminishing (TVD) flux limiter. The CFL number was ramped from 0.1 to 50 over the first 100 iterations and remained at 50 for the remaining iterations.

### 2.2. COMPRESSIBLE REYNOLDS AVERAGED NAVIER STOKES EQUATIONS

The work presented in this thesis is based on the RANS modeling approach in CFD++. A brief review of the RANS approach is discussed below. Turbulent flows are characterized by chaotic, irregular, three-dimensional motion that is time-dependent and spans a range of time and length scales. For many engineering problems, a direct numerical simulation (DNS) is prohibitively expensive, as it is necessary to resolve all physically relevant turbulent scales down to Kolmogorov scales. Therefore for practical engineering flows, it is necessary to

take advantage of turbulence models to approximate solutions. Turbulence models adopt a statistical treatment to the fundamentally random motion. Reynolds Averaging takes statistical averages to simplify the modeling of turbulence.

Reynolds introduced the concept that the flow velocity vector,  $u_i$  can be decomposed and represented as a fluctuation,  $u'_i$ , about a mean component  $U_i$ , as follows:

$$u_i = U_i + u'_i \tag{2.1}$$

A conservation equation can be developed and solved for the mean quantities, one such method is the Reynolds-averaged Navier Stokes (RANS) approach which includes the influence of the fluctuations on the mean flow via turbulence modeling [25]. For compressible flows, Reynolds averaging significantly alters the original form of the Navier-Stokes equations and complicates turbulence modeling and closure; thus CFD++ uses Favre-averaging for solving the compressible Navier-Stokes equations. The Favre-averaged Navier-Stokes equations are commonly referred to as the compressible RANS equations, despite the semantic inaccuracy. The Favre time averaging, is a mass weighted time averaging procedure that circumvents the high-order correlations that are introduced with Reynolds averaging. Favre averaging decomposes the instantaneous solution variable,  $\phi$ , into a mean quantity,  $\tilde{\phi}$ , and a fluctuating component,  $\phi''$ , shown by:

$$\phi = \tilde{\phi} + \phi'' \tag{2.2}$$

The derivation of the Favre-averaged Navier-Stokes (FANS) equations is not provided, but it is recommended that the reader explore the work presented by Groth [25]. The FANS equations are given by:

$$\frac{\partial}{\partial t} (\bar{\rho}) + \frac{\partial}{\partial x_i} (\bar{\rho} \tilde{u}_i) = 0 \quad (2.3)$$

$$\frac{\partial}{\partial t} (\bar{\rho} \tilde{u}_i) + \frac{\partial}{\partial x_j} (\bar{\rho} \tilde{u}_i \tilde{u}_j + \bar{p} \delta_{ij}) = \frac{\partial}{\partial x_j} (\bar{\tau}_{ij} - \overline{\rho u_i'' u_j''}) \quad (2.4)$$

$$(2.5)$$

$$\begin{aligned} \frac{\partial}{\partial t} \left[ \bar{\rho} \left( \tilde{e} + \frac{1}{2} \tilde{u}_i \tilde{u}_i \right) + \frac{1}{2} \overline{\rho u_i'' u_i''} \right] + \frac{\partial}{\partial x_j} \left[ \bar{\rho} \tilde{u}_j \left( \tilde{h} + \frac{1}{2} \tilde{u}_i \tilde{u}_i \right) + \frac{\tilde{u}_j}{2} \overline{\rho u_i'' u_i''} \right] \\ = \frac{\partial}{\partial x_j} \left[ (\bar{\tau}_{ij} - \overline{\rho u_i'' u_j''}) \tilde{u}_i - \bar{q}_j \right] \\ + \frac{\partial}{\partial x_j} \left[ -\overline{\rho u_j'' h''} - \frac{1}{2} \overline{\rho u_j'' u_i'' u_i''} + \overline{\rho u_i'' \tau_{ij}} \right] \end{aligned} \quad (2.6)$$

where (2.3) represents the continuity equation, (2.4) is the momentum equation, and (2.6) is the energy equation.

The Favre-Averaged Reynolds stress tensor is given by:

$$\lambda = -\overline{\rho u_i'' u_j''} \quad (2.7)$$

which is a symmetric tensor that incorporates the effects of the unresolved turbulent fluctuations on the mean flow. The Reynolds stress tensor provides six unknown values leading to the closure problem for the FANS equation set. Turbulence modeling provides a means for specifying  $\lambda$  in terms of mean flow solution quantities. The turbulent kinetic energy is given by:

$$\frac{1}{2} \overline{\rho u_i'' u_i''} = -\frac{1}{2} \lambda_{ii} = \bar{\rho} \tilde{k} \quad (2.8)$$

A brief review of the FANS equations has been provided. It is recommended that the reader investigate works by Wilcox [26], Pope [27], and Groth [25] for further study.

### 2.3. REALIZABLE $k$ - $\epsilon$ TURBULENCE MODEL

The realizable  $k$ - $\epsilon$  turbulence model was used for all simulations in this study. The realizable  $k$ - $\epsilon$  model has been a benchmark for practical engineering flows as it is robust, computationally efficient, and capable of handling a range of turbulent flows. Furthermore, the  $k$ - $\epsilon$  model was used in a previous computational study by Pratt et al. [7] for modeling the discharge of flapped outlets. A brief review of the realizable  $k$ - $\epsilon$  turbulence model is provided below.

Turbulence modeling provides a mathematical framework for determining additional terms and correlations introduced by the FANS equations [25]. The realizable  $k$ - $\epsilon$  model, adds two additional transport equations, one for  $k$  and another for  $\epsilon$ . The two equation realizable  $k$ - $\epsilon$  model employs the Boussinesq relation to obtain Reynolds-stresses algebraically from the modeled eddy viscosity,  $\mu_t$ , and the mean-strain rate tensor  $S_{ij}$  given by:

$$\overline{\rho u_i u_j} = \frac{2}{3} \delta_{ij} \rho k - \mu_t S_{ij} \quad (2.9)$$

where

$$S_{ij} = \left( \frac{\partial U_i}{\partial x_j} + \frac{\partial U_j}{\partial x_i} - \frac{2}{3} \frac{\partial U_k}{\partial x_k} \delta_{ij} \right) \quad (2.10)$$

The model consists of the following transport equations for turbulent kinetic energy,  $k$ , and the rate of dissipation of turbulent kinetic energy,  $\epsilon$ , given by:

$$\frac{\partial(\rho k)}{\partial t} + \frac{\partial(U_j \rho k)}{\partial x_j} = \frac{\partial}{\partial x_j} \left[ \left( \mu + \frac{\mu_t}{\sigma_k} \right) \frac{\partial k}{\partial x_j} \right] + P_k - \rho \epsilon \quad (2.11)$$

$$\frac{\partial(\rho \epsilon)}{\partial t} + \frac{\partial(U_j \rho \epsilon)}{\partial x_j} = \frac{\partial}{\partial x_j} \left[ \left( \mu + \frac{\mu_t}{\sigma_\epsilon} \right) \frac{\partial \epsilon}{\partial x_j} \right] + (C_{\epsilon_1} P_k - \rho \epsilon C_{\epsilon_2} + E) T_t^{-1} \quad (2.12)$$

where the rate of production of turbulent energy,  $P_k$ , is given by:

$$P_k = -\rho \overline{u_i u_j} \frac{\partial U_i}{\partial x_j} \quad (2.13)$$

and  $T_t$  is the realizable estimate of the turbulence time scale given by:

$$T_t = \frac{k}{\epsilon} \max(1, \zeta^{-1}) \quad (2.14)$$

$$\zeta = \sqrt{\frac{R_t}{2}} \quad (2.15)$$

and the turbulent Reynolds number,  $R_t$ , is given by:

$$R_t = \frac{\rho k^2}{\mu \epsilon} \quad (2.16)$$

The additional energy term,  $E$ , in the dissipation-rate equation is designed to improve the model response to adverse pressure-gradient flows. The term is given by:

$$E = A_E \rho \sqrt{\epsilon T_t} \psi \max\left(k^{\frac{1}{2}}, (\nu \epsilon)^{\frac{1}{4}}\right) \quad (2.17)$$

$$\psi = \max\left(\frac{\partial k}{\partial x_j} \frac{\partial \tau}{\partial x_j}, 0\right) \quad (2.18)$$

$$\tau = \frac{k}{\epsilon} \quad (2.19)$$

The model constants are given by:

$$C_\mu = 0.09, \quad C_{\epsilon_1} = 1.44, \quad C_{\epsilon_2} = 1.92, \quad \sigma_k = 1.0, \quad \sigma_\epsilon = 1.3, \quad A_E = 0.3$$

The eddy viscosity,  $\mu_t$ , is obtained from:

$$\mu_t = \min \left( C_\mu, \frac{f_\mu \rho k^2}{\epsilon}, \frac{\phi \rho k}{S} \right)$$

$$\phi = \begin{cases} 2/3, & \text{Schwartz} \\ 0.31, & \text{Bradshaw} \end{cases} \quad (2.20)$$

where the dimensional strain magnitude,  $S$ , is given by:

$$S = \sqrt{\frac{S_{kl} S_{kl}}{2}} \quad (2.21)$$

and  $f_u$  is a low-Reynolds number function designed to account for viscous and inviscid damping of turbulent fluctuations in the proximity of solid surfaces given by:

$$f_\mu = \frac{1 - e^{-0.00084R_t}}{1 - e^{-\sqrt{R_t}}} \max \left[ 1, \left( \frac{2}{R_t} \right)^{\frac{1}{2}} \right] \quad (2.22)$$

## 2.4. WALL FUNCTIONS

In many practical engineering flows, wall functions are necessary to model near wall turbulence due to computational limitations. The realizable  $k$ - $\epsilon$  turbulence model can be solved to the wall, however, the computational costs for appropriate grid resolution  $y_1^+ < 1$  and reasonable boundary layer stretching ratios of 1 to 1.3 was prohibitively expensive for the approximately 700 cases that were simulated. Wall functions were used to obtain momentum and energy fluxes for all wall boundaries. In this thesis, the wall  $y_1^+$  was between 20-40, depending on flow conditions. Due to the complex and varying flow physics, a fixed first layer height was used for all cases, thus depending on flow conditions the wall  $y_1^+$  will vary. The advanced two-layer wall function in CFD++ was utilized for all cases. The two-layer

wall function incorporates elements from the formulation suggested by Laufer and Spalding and is based on a velocity scale of  $\sqrt{k}$ , where  $k$  is the turbulent kinetic energy predicted by the  $k$ - $\epsilon$  closure. The two-layer wall function is immune to reversed flow regions, including the separation and reattachment points where  $\tau_w = 0$  and avoids iterative solutions in solving for the friction velocity as  $k$  is directly available from the turbulence model [24].

## 2.5. CONVERGENCE

Convergence was determined by examining the behavior of the normalized residuals, door forces, hinge moments, and mass flow rates exiting the internal mass flow surface with increasing iteration count. A solution was deemed converged after a 4-5 order decrease in the magnitude of the normalized residuals. Hinge moments, door forces, and internal mass flow rates were examined to ensure that the calculated quantities were not changing with increasing iteration count. The mass flow rate would typically converge before the door forces, hinge moments, or the desired reduction in normalized residuals was achieved. Simulations converged after 500-2500 iterations, with higher free stream Mach number, plenum pressure, and altitude cases requiring more iterations.

## 2.6. COMPUTATIONAL RESOURCES AND COSTS

Simulations were carried out on two high performance compute servers at Colorado State University. The primary compute server, Atlantis, was maintained by the CFD and Propulsion Laboratory and consisted of 9 compute nodes and 24 TB of storage connected by a 40 Gbps Infiniband network. Four of the compute nodes, contained 20 Intel Sandy Bridge CPU cores, and NVIDIA Tesla K20 GPU, and 128 GB of memory. The remaining 5 compute nodes contained 24 Intel Haswell cores and 64 GB of memory each. The other compute server was

maintained by the Information Science and Technology Center (ISTeC) at Colorado State University. The ISTeC Cray is a Model XE6 with 2,688 compute cores, 2.5 TB of main memory, a Gemini 3D-torus interconnect and 32 TB of disk storage. The computational cost for a single simulation with a grid size on the order of  $5 \times 10^6$  cells was approximately 4 hours on 120 CPU cores on Atlantis. In total, there were approximately 700 cases run for the work presented in this thesis.

## 2.7. POST PROCESSING

Analysis of data extracted from CFD solutions was post-processed to evaluate the discharge and moment characteristics of PRD's at varying flow and geometrical conditions. Mass flow rates through the leading, lateral, and trailing surfaces along with hinge moments and door forces were extracted within CFD++. Mass flow rates, moments, and forces were doubled to account for the symmetry condition. A brief review of the equations used for post processing are discussed below. The exit mass flow rate within CFD++ was computed as:

$$\dot{m} = \rho \vec{u} \cdot \hat{n}A \quad (2.23)$$

where  $\rho$  is the density,  $\vec{u}$  is the velocity vector, and  $\hat{n}A$  is the normal component of area. The forces acting on the door included both viscous and inviscid components and were computed as:

$$\begin{aligned} F_{tot} &= F_{inv} + F_{vis} \\ F_{inv} &= p\hat{n}A \\ F_{vis} &= \vec{\tau} \cdot \hat{n}A \end{aligned} \quad (2.24)$$

where  $p$  is the pressure and  $\vec{\tau}$  is the viscous stress tensor. The forces acting on the door were extracted for thrust and lift coefficient calculations. The forces were also used in the moment calculations given by:

$$\begin{aligned}\vec{F} &= \sum \vec{f} \\ \vec{f} &= f_x \hat{i} + f_y \hat{j} + f_z \hat{k}\end{aligned}\tag{2.25}$$

where the moments were calculated by:

$$\sum \vec{r} \times \vec{f} = \sum \left( \vec{r}_0 + (\vec{P}_0 - \vec{P}) \right) \times \vec{f}\tag{2.26}$$

where  $\vec{r}_0$  is a position vector on the body surface relative to the origin  $\vec{P}_0$ , and  $\vec{P}$  is the reference hinge moment point defined as the hinge location. The opening moment was defined as the moment acting on the bottom surface of the door, while the closing moment was defined as the moment acting on the top surface of the door. The total moment was the sum of the moments acting on the top, side, and bottom surfaces of the door.

**2.7.1. POST PROCESSING CALCULATIONS.** Post processing of the CFD data was carried out through extensive use of Bash scripting. Scripts were implemented to transfer data, post process results, and generate figures. Bash scripts provide an efficient and consistent method for handling large quantities of data. Scatter and surface plots were generated with the open source software Tikz. Contour plots, streamlines, and surface temperature extraction was performed with the open source software VisIt, originating from Lawrence Livermore National Lab [28]. A brief review of the calculated quantities is provided below.

2.7.1.1. *Minimum Geometric Flow Area.* The minimum geometric flow area,  $A_{\min}$  was calculated as:

$$A_{\min} = \min (A_{\text{geo}}, A_{\text{door}}) \quad (2.27)$$

where  $A_{\text{geo}}$  is the geometric flow area created by the door opening and  $A_{\text{door}}$  is the area of the door. For all cases examined, the door area is equivalent to the door opening area.

2.7.1.2. *Discharge Coefficient.* The discharge coefficient is a measure of the effectiveness of a particular opening and is based on isentropic relationships assuming an ideal gas. Depending on flow conditions, the discharge coefficient is deemed to be choked or unchoked depending on the pressure ratio and critical pressure ratio. In the choked calculations, the Mach number is assumed to be 1.

The pressure ratio is calculated as:

$$\alpha_P = \frac{P_{0,\text{plen}}}{P_{\infty}} \quad (2.28)$$

where  $P_{0,\text{plen}}$  is the plenum total pressure and  $P_{\infty}$  is the freestream static pressure. For the burst duct analysis, the plenum static pressure is always equal to the plenum total pressure due to the quiescent flow assumption. The critical pressure ratio,  $\alpha_{P,\text{CR}}$  is calculated as:

$$\alpha_{P,\text{CR}} = 1 + \left( \frac{\gamma - 1}{2} \right)^{\left( \frac{\gamma}{\gamma - 1} \right)} \quad (2.29)$$

where  $\gamma$  is the ratio of specific heats based on the plenum conditions. The discharge coefficient is obtained by evaluating if the pressure ratio  $\alpha_P$  is greater than the critical pressure ratio  $\alpha_{P,\text{CR}}$ ; if it is, the discharge coefficient is based on the choked discharge coefficient calculation

otherwise it is based on the unchoked discharge coefficient calculation as given by:

$$C_d = \begin{cases} C_{d,\text{choked}} & \alpha_P > \alpha_{P,\text{CR}} \\ C_{d,\text{unchoked}} & \alpha_P \leq \alpha_{P,\text{CR}} \end{cases} \quad (2.30)$$

where the choked discharge coefficient,  $C_{d,\text{choked}}$  is calculated as:

$$C_{d,\text{choked}} = \frac{\dot{m}}{P_{0,\text{plen}} A_{\text{min}} \left[ \left( \frac{\gamma G}{RT_{0,\text{plen}}} \right) \left( \frac{2}{1+\gamma} \right)^{\frac{\gamma+1}{\gamma-1}} \right]^{0.5}} \quad (2.31)$$

where  $\dot{m}$  is the exit mass flow rate,  $P_{0,\text{plen}}$  is the plenum total pressure,  $A_{\text{min}}$  is the minimum geometric flow area,  $G$  is a gravitational conversion factor, and  $R$  is the specific gas constant for air. The unchoked discharge coefficient,  $C_{d,\text{unchoked}}$  is calculated by:

$$C_{d,\text{unchoked}} = \frac{\dot{m}}{P_{0,\text{plen}} A_{\text{min}} \left[ \left( \frac{2G}{RT_{0,\text{plen}}} \right) \frac{\gamma}{\gamma-1} \left( \left( \frac{1}{\alpha_P} \right)^{\frac{2}{\gamma}} - \left( \frac{1}{\alpha_P} \right)^{\frac{\gamma+1}{\gamma}} \right) \right]^{0.5}} \quad (2.32)$$

2.7.1.3. *Effective Area.* An important parameter in evaluating PRD performance is the effective area,  $A_{\text{eff}}$ , which accounts for the minimum geometric flow area and the discharge coefficient. The effective area is calculated as:

$$A_{\text{eff}} = A_{\text{min}} C_d \quad (2.33)$$

The effective area was non-dimensionalized by dividing by door area given by:

$$A_{\text{eff},x} = \frac{A_{\text{eff}}}{A_{\text{door}}} \quad (2.34)$$

2.7.1.4. *Corrected Mass Flow Rate.* The corrected mass flow rate,  $\dot{m}_{\text{corr}}$ , is calculated as:

$$\dot{m}_{\text{corr}} = \frac{\dot{m}\sqrt{T_{0,\text{plen}}}}{\sqrt{P_g}} \quad (2.35)$$

where  $\dot{m}$  is the exit mass flow rate,  $T_{0,\text{plen}}$  is the plenum total temperature, and  $P_g$  is the plenum gauge pressure. The corrected mass flow rate collapses the data associated with changes in plenum quantities. It should be noted that the corrected mass flow rate is only applicable to unchoked flow conditions, which a majority of the cases are.

2.7.1.5. *Discharge Flow Ratio.* An important parameter in several literature cases is the discharge flow ratio,  $DFR$ , which is calculated as:

$$DFR = \frac{\dot{m}}{\rho_\infty U_\infty A_{\text{min}}} \quad (2.36)$$

where  $\rho_\infty$  is the freestream density and  $U_\infty$  is the freestream velocity. Discharge flow ratio compares the discharge through the minimum geometric flow area compared to mass flow through the same minimum area in the freestream.

2.7.1.6. *Hinge Moment Coefficient.* The total moment acting on the hinge was non-dimensionalized as the hinge moment coefficient,  $C_{\text{m,hinge}}$ , which is calculated as:

$$C_{\text{m,hinge}} = \frac{M_0}{\frac{1}{2}\rho_\infty U_\infty^2 A_{\text{min}} L_D} \quad (2.37)$$

where  $M_0$  is the total door moment,  $\frac{1}{2}\rho_\infty U_\infty^2$  is the freestream dynamic head,  $A_{\text{min}}$  is the minimum geometric flow area, and  $L_D$  is the door chord length.

2.7.1.7. *Thrust and Lift Coefficient.* Thrust and lift characteristics for the CFD cases were evaluated. The thrust coefficient,  $C_T$  was calculated as:

$$C_T = \frac{F_x}{\frac{1}{2}\rho_\infty U_\infty^2 A_{\min}} \quad (2.38)$$

where  $F_x$  is the streamwise component of force acting on the door,  $\frac{1}{2}\rho_\infty U_\infty^2$  is the freestream dynamic head, and  $A_{\min}$  is the minimum geometric flow area. Negative values of thrust coefficient indicate that the door is creating drag while positive values indicate a thrust force is generated. The lift coefficient,  $C_L$ , was calculated as:

$$C_L = \frac{F_y}{\frac{1}{2}\rho_\infty U_\infty^2 A_{\min}} \quad (2.39)$$

where  $F_y$  is the vertical component of force acting on the door. The lift coefficient value does not play a significant role in the performance of the PRD.

2.7.1.8. *Average Wall Temperature.* A post processing method was developed to compare the average wall surface temperatures on the bottom wall of the freestream domain. The average wall surface temperature of the bottom wall surface was extracted from a slice on the bottom wall of the three-dimensional domain and the average value on that slice was obtained using the area average value query within VisIt. The average wall temperature provides a metric for observing the impact of geometric and flow conditions on the surface temperatures near the PRD opening. The non-dimensional average wall temperature,  $\overline{T}_x$  was calculated as:

$$\overline{T}_x = \frac{\overline{T_{0,\text{wall}}} - T_{0,\infty}}{T_{0,\text{plen}} - T_{0,\infty}} \quad (2.40)$$

where  $\overline{T_{0,\text{wall}}}$  is the average wall temperature extracted from VisIt,  $T_{0,\infty}$  is the freestream total temperature, and  $T_{0,\text{plen}}$  is the plenum total temperature.

2.7.1.9. *Non-dimensional High Temperature Area.* A method was developed to examine the non-dimensional high temperature contact area. The threshold temperature was defined as a wall temperature greater than 400 °F, above which, insulating blankets or high temperature materials are required. The high temperature area was obtained using VisIt by plotting the total temperature on the bottom wall surface and extracting the surface area enclosed by the contour line for wall temperatures greater than or equal to 400 °F. The high temperature contact area was non-dimensionalized by a reference area equal to the door surface area. Figure 2.1 illustrates an example of the total temperature contours at a 15° door angle where the dashed black lines encompass the regions of temperature greater than 400 °F.

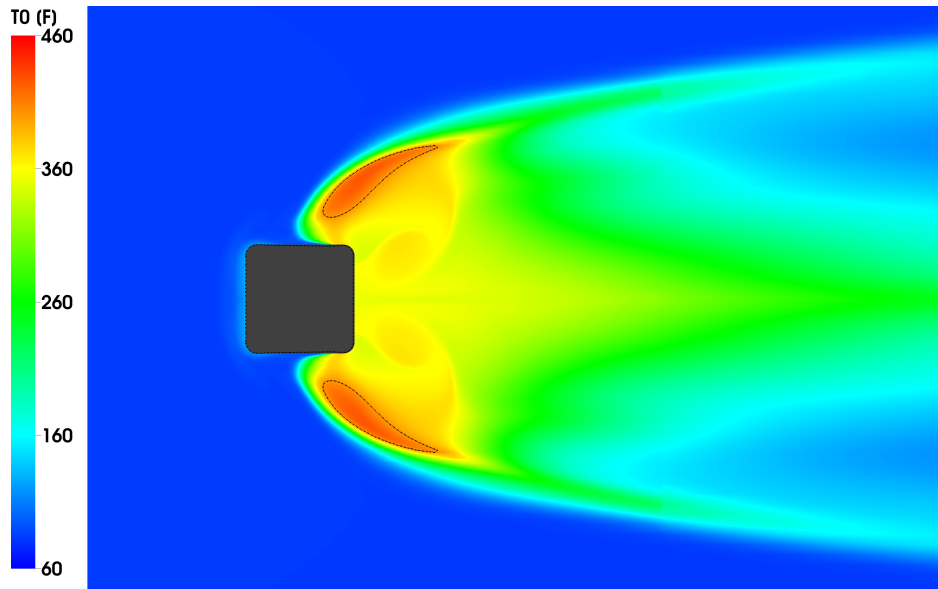


FIGURE 2.1. Total temperature contours on bottom wall of freestream domain with contour line of temperatures greater than 400 °F indicated.

## CHAPTER 3

# MODELING OF PRESSURE RELIEF DOOR

The expensive nature of a high-speed wind tunnel experiments is cost prohibitive for experimental analysis. With the advancement of computational models and high-performance computing, a CFD analysis provides a cost and time efficient method to develop a solid understanding of PRD flow behavior. The CFD analysis allows for novel geometric configurations across a wide range of operating conditions to be investigated in a timely manner. A comparable experimental study would be difficult to design and instrument in a cost efficient manner. From the CFD simulations, PRD performance can be quantified and 3D flow features can be visualized that would otherwise be difficult to determine. An overview of the physical component geometry, boundary conditions, and the computational grids are provided below.

### 3.1. PHYSICAL COMPONENT GEOMETRIES AND CONFIGURATIONS

The initial step in creating a computational model was to generate a physical component geometry representative of a realistic PRD configuration. The computational geometry used in this thesis was developed in collaboration with a team of engineers from the Boeing company. The computational domain consisted of three primary components; a rectangular freestream domain, rectangular plenum compartment, and a fixed angle pressure relief door as shown in Figure 3.1.

The freestream domain extended 52 in. upstream of the leading edge of the door opening, 178 in. downstream of the trailing edge of the door opening, and 55 in. spanwise from the symmetry plane. The domain extended farther downstream than upstream due to the

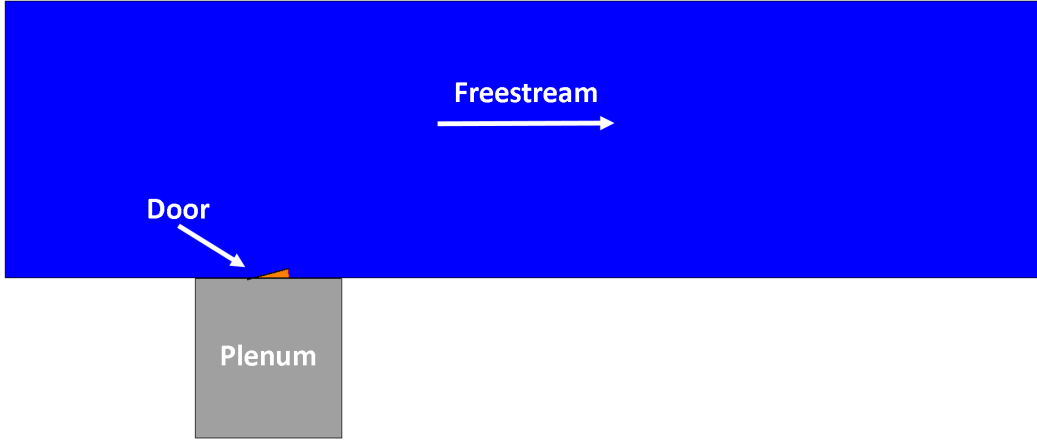


FIGURE 3.1. Symmetry plane view of the computational domain.

relative difference in leading edge and trailing edge flow. The top surface of the freestream domain is located 61 in. wall-normal from the bottom wall. A uniform  $\frac{1}{8}$  in. gap between the freestream bottom wall and the upper plenum wall was modeled to reflect the wall thickness of the core casing. A simplification was made in assuming a uniform wall thickness as on-engine PRD's will have varying wall thicknesses depending on location. The door thickness was assumed to be the same wall thickness, thus at  $0^\circ$  no perturbations in the surface exist and no mass flow exits the plenum. The static plenum chamber extends 12 in. upstream and downstream of the door opening and is 37 in. in height. All geometries had a uniform door area of  $100 \text{ in}^2$  to maintain consistency across all geometric configurations. Due to the symmetric nature of the flow, half of the computational domain was modeled to minimize computational expense. The symmetry plane assumption may result in the loss of resolving flow features downstream of the door, but the tradeoff was deemed necessary for the decreased computation time.

The work presented in this thesis examined three unique hinge types. The “Gooseneck-hinge” type pivoted 1.5 in. upstream of the leading edge of the door opening as shown in Figure 3.2a. The “Piano-hinge” type pivoted at the leading edge of the door opening as

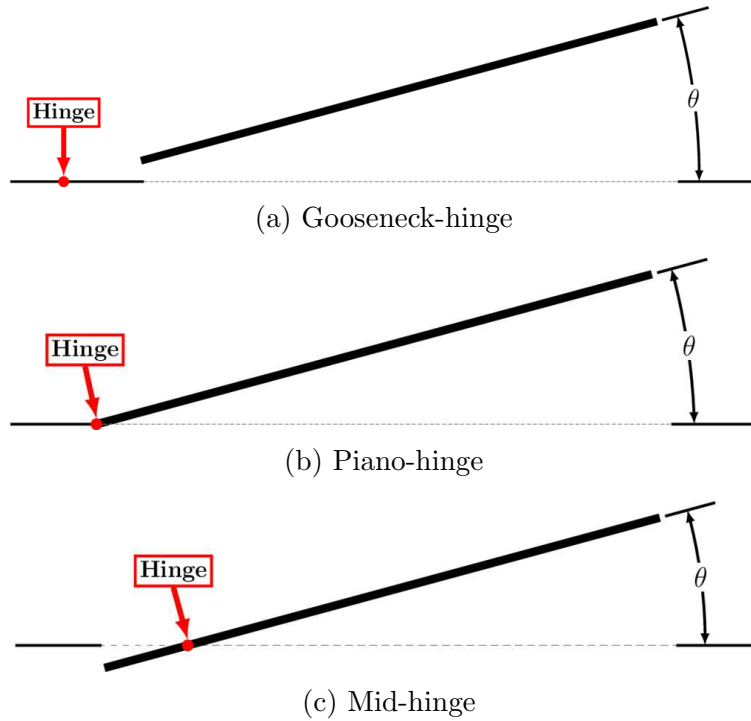


FIGURE 3.2. Hinge type comparison.

shown in Figure 3.2b. The “Mid-hinge” hinge type pivoted 1.5 in. downstream of the leading edge of the door opening as depicted in Figure 3.2c. The vertical location of the hinge is located at the midpoint of the wall thickness,  $\frac{1}{16}$  in. below the freestream bottom wall.

The comprehensive parameter study examined the Gooseneck-hinge and Mid-hinge types for rectangular shaped doors with 1 in. rounded corners. The geometry provides a realistic representation of currently used on-engine geometries. Door aspect ratios of 0.75, 1.0, 1.25, and 1.5 are examined where the aspect ratio is defined as the chord length divided by the span width. The parameter study also examined vertical hinge offset; where the hinge is offset 0.75 in. into the plenum domain as shown in Figure 3.3.

Various geometrical configurations for the Gooseneck-hinge, Mid-hinge, and Piano-hinge types were also investigated. The study examined variations in door shape, corner rounding, and the addition of lateral edge fences. The fence geometry extended approximately

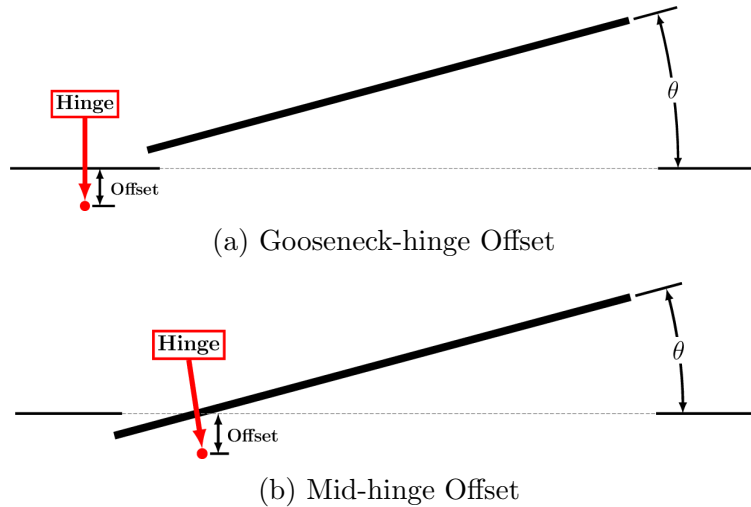


FIGURE 3.3. Hinge type comparison for vertical hinge offset.

perpendicular to the bottom surface of the door to the top surface of the freestream wall for the length of the lateral edge of the door. Trapezoidal geometries had a trailing edge width that is 80% of the leading edge width.

The Gooseneck-hinge geometric comparison investigated four unique geometries as shown in Figure 3.4. The first embodiment, denoted as the baseline geometry, is a rectangular door with 1 in. rounded corners as shown in Figure 3.4a. The baseline rectangular geometry was the same as that used in the comprehensive parameter study. The second embodiment featured a trapezoidal geometry with 1 in. rounded corners as shown in Figure 3.4b. A third embodiment featured a rectangular door with square corners as shown in Figure 3.4c. The fourth embodiment featured the same square corner geometry as the third embodiment with the addition of lateral edge fences as shown in Figure 3.4d.

The Mid-hinge geometric comparison investigated three unique geometries as shown in Figure 3.5. The first embodiment, denoted as the baseline geometry, featured a rectangular door with 1 in. rounded corners as shown in Figure 3.5a. The rectangular baseline geometry is the same as that used in the comprehensive parameter study. The second embodiment

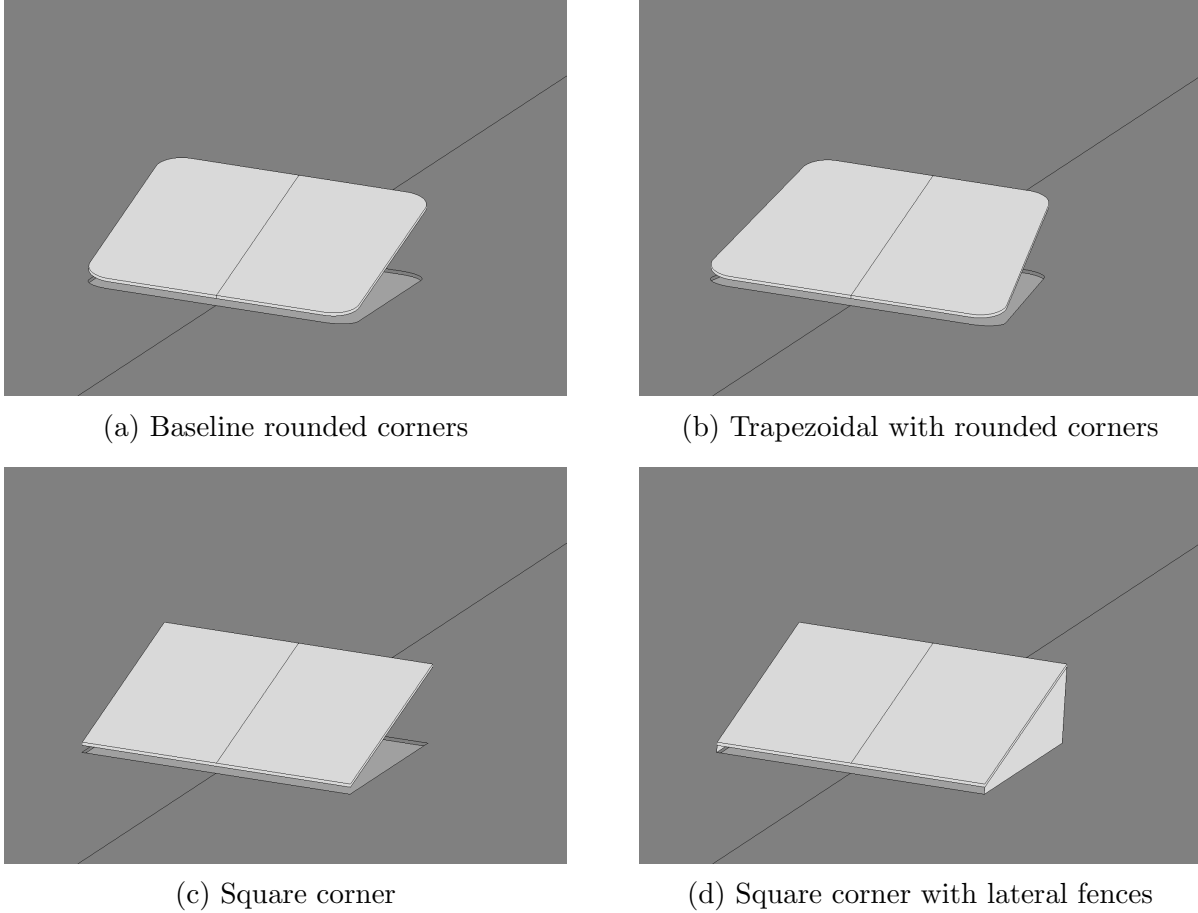
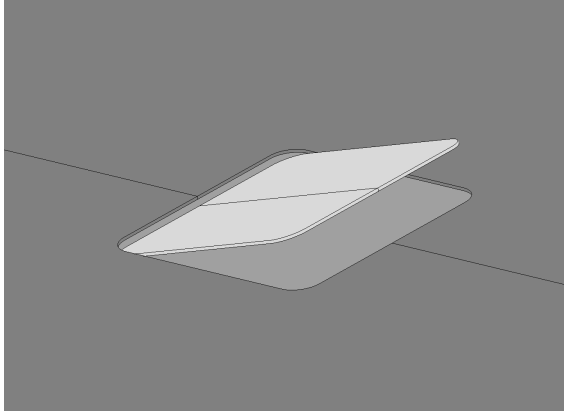


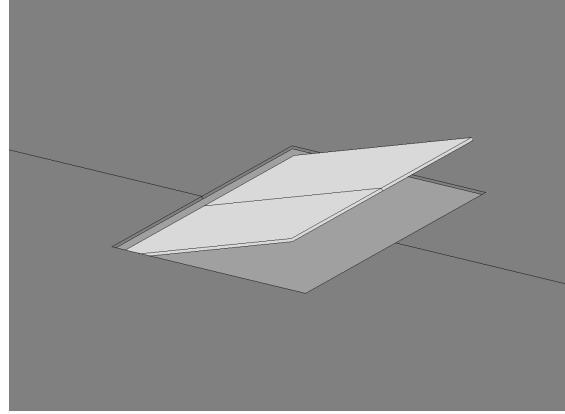
FIGURE 3.4. Geometrical configurations of Goosneck-hinge type.

features a rectangular door with square corners as shown in Figure 3.5b. The third embodiment features the same square corner geometry with the addition of lateral edge fences downstream of the hinge point as shown in Figure 3.5c. The lateral edge fences are only applied downstream of the hinge point as the lateral surface upstream of the hinge point was immersed in the plenum chamber and did not have a significant contribution to the exit flow characteristics.

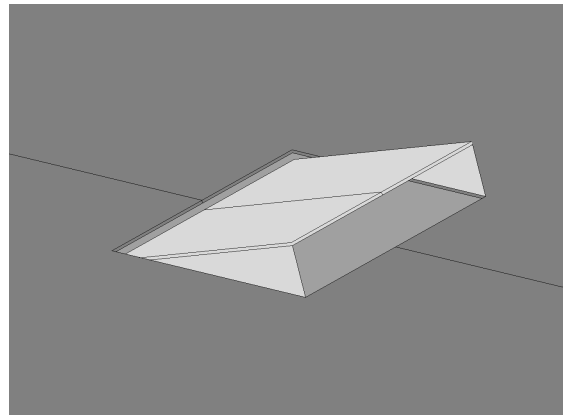
The Piano-hinge geometric comparison investigated four unique geometries as shown in Figure 3.6. The first embodiment featured a rectangular door with square corners as shown in Figure 3.6a. The second embodiment featured the same square corner geometry with the addition of lateral edge fences as shown in Figure 3.6b. The third embodiment



(a) Baseline rounded corners



(b) Square corner

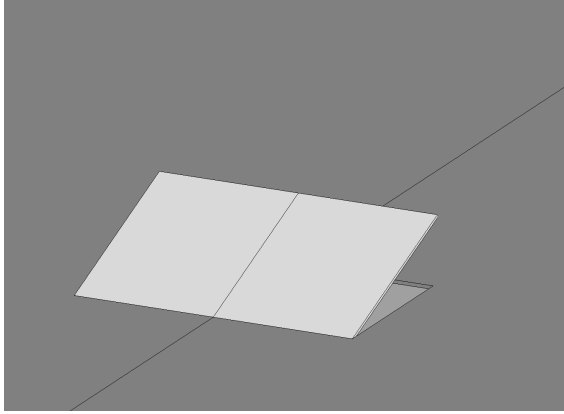


(c) Square corner with lateral fences

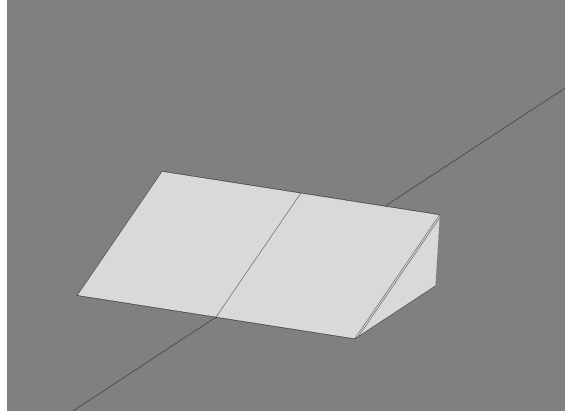
FIGURE 3.5. Geometrical configurations of Mid-hinge type.

featured a trapezoidal door geometry with square corners as shown in Figure 3.6c. The fourth embodiment featured the same trapezoidal geometry with the addition of lateral edge fences as shown in Figure 3.6d.

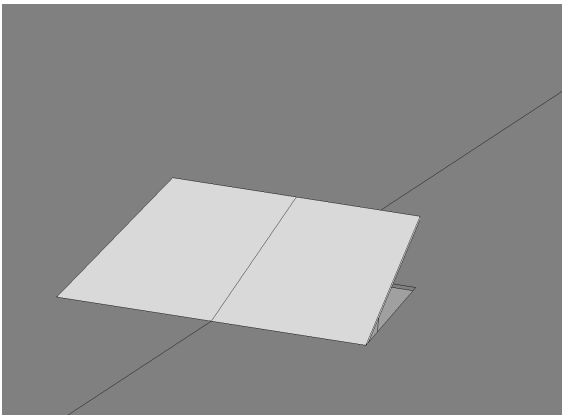
3.1.1. MODELING CHALLENGES. Several challenges were encountered in developing the geometric configuration. The most challenging aspect was developing internal surfaces around the door opening that allowed for the internal mass flow rates to be extracted. A detailed discussion is provided in the following sections. Several iterations were required to determine the appropriate freestream and plenum domain size. Modeling the curvature of the core casing compartment adds additional difficulty but is not believed to significantly affect



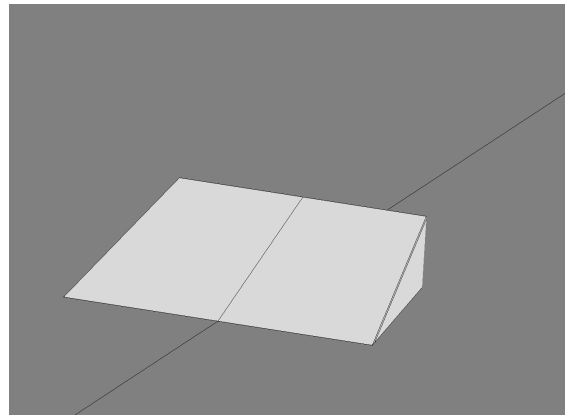
(a) Square Corner



(b) Square Corner with Lateral Fences



(c) Square Corner Trapezoidal



(d) Square Trapezoidal with Lateral Fences

FIGURE 3.6. Piano-hinge geometries compared.

the solution therefore, a rectangular freestream domain and plenum were assumed. Hinge and latch geometries are continually changing as novel designs are developed. The hinge and latch mechanisms include several small intricate flow paths and variations in thickness that require a highly resolved grid. A simplification was made that excludes the hinge and latch geometry, a significant simplification compared to a realistic PRD assembly. Depending on desired PRD and engine type, variable wall thicknesses exists so a uniform thickness was assumed to simplify the modeling complexity. While these simplifications may limit the applicability to modeling a realistic core-casing flow, the trends observed are helpful to the aircraft designer for analysis and development of future PRD designs.

## 3.2. BOUNDARY CONDITIONS

Once the geometric model was developed, it was necessary to define appropriate boundary conditions for the CFD analysis. Boundary conditions for CFD++ were defined in Pointwise and exported using a CAE utility. The boundary conditions for the flow domain are labeled in Figure 3.7 with the corresponding boundary condition described in Table 3.1. The characteristics-based inflow/outflow boundary condition was specified for all freestream boundaries in the computation where the velocity and static quantities were known. An operating pressure was defined for the entire system equal to the freestream static pressure. The plenum chamber was specified as a reservoir boundary condition where total pressure and total temperature were specified. It was assumed that the plenum flow remained static, similar to a burst duct event. The plenum pressure was defined as a gauge pressure relative to the freestream operating static pressure. Based on input from a Metacomp representative, the turbulence quantities  $k$ - $\epsilon$  were specified using a known freestream turbulence level of 0.002 for both the freestream and plenum. The freestream turbulence was specified using a known length scale equivalent to 1/4 of the freestream domain height and the freestream velocity. The plenum domain turbulence was specified with a length scale equivalent to 1/4 of the plenum length and a velocity of 4m/s. The non-zero plenum velocity was used to prevent unnecessarily large values of  $k$ - $\epsilon$  from being specified. Wall boundaries were assumed to be adiabatic and viscous wall functions were used.

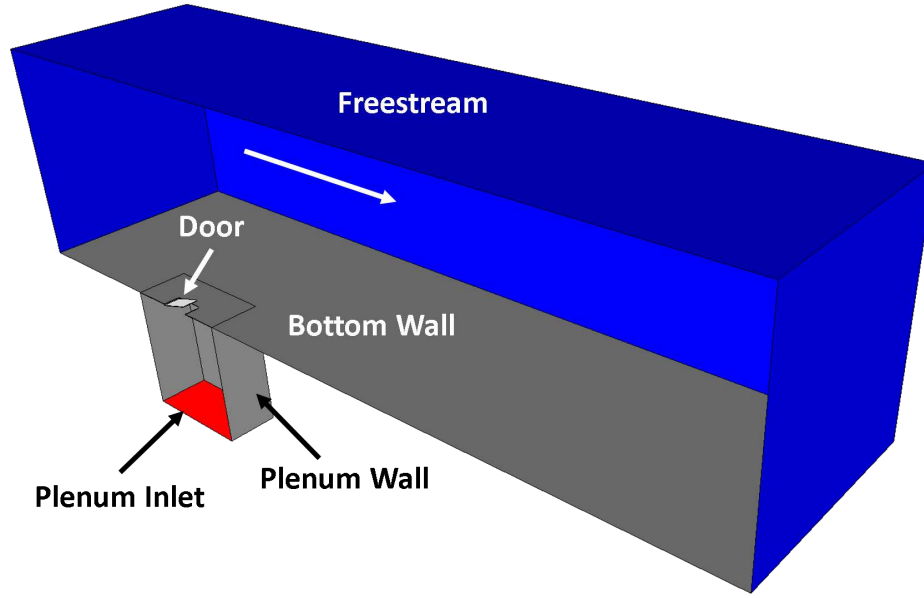


FIGURE 3.7. Isometric view of computational domain.

The internal mass flow rate surfaces (shown in Figure 3.8) were defined as a simple flow through continuous zonal boundary. The specified boundary condition allowed for mass flow rates to be extracted at the desired internal boundaries. Due to the multi-block nature of the grid, zonal boundaries were specified at all block interfaces. A comprehensive list of the boundary conditions used are listed in Table 3.1.

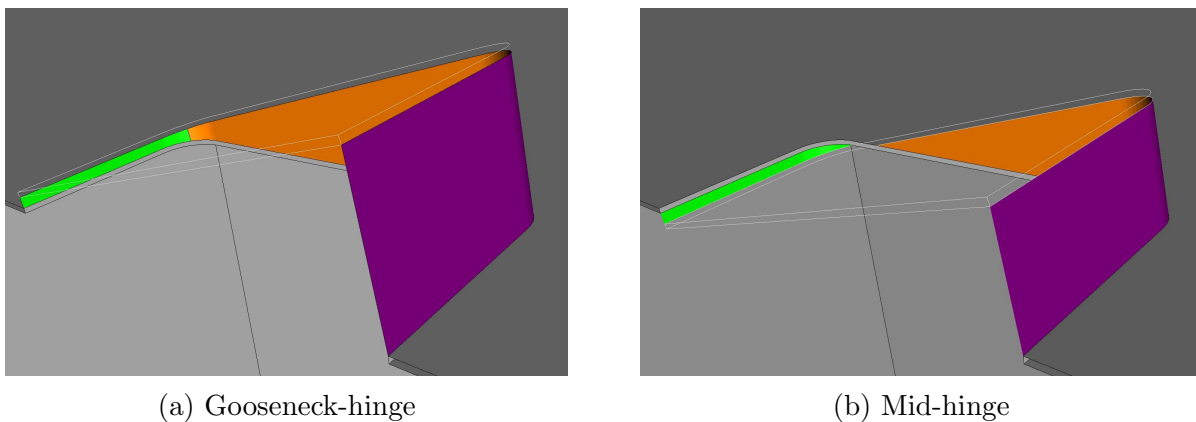


FIGURE 3.8. Isometric view of internal mass flow surfaces; leading edge (green), lateral edge (orange) and trailing edge (purple).

TABLE 3.1. Boundary conditions corresponding to Figure 3.7 and Figure 3.8.

<b>Boundary</b>	<b>Color</b>	<b>Boundary Condition</b>
<b>Freestream</b>	Blue	Characteristics-based inflow/outflow
<b>Plenum inlet</b>	Red	Reservoir $P_{tot}$ - $T_{tot}$
<b>Freestream bottom wall</b>	Dark Gray	Adiabatic viscous wall function
<b>Pressure relief door</b>	White	Adiabatic viscous wall function
<b>Plenum walls</b>	Light Gray	Adiabatic viscous wall function
<b>Leading mass flow surface</b>	Green	Zonal, simple flow through continuous
<b>Lateral mass flow surface</b>	Orange	Zonal, simple flow through continuous
<b>Trailing mass flow surface</b>	Purple	Zonal, simple flow through continuous
<b>Internal zonal boundaries</b>	NA	Zonal, simple flow through continuous
<b>Symmetry plane</b>	NA	Symmetry

### 3.3. COMPUTATIONAL GRIDS

Once the domain and boundary conditions were established, grids were generated using Pointwise V17.1, a commercial grid generation software. The most difficult part of the computational analysis was developing the computational grids. In particular, developing grids that adhered to the desired internal mass flow surfaces that maintained appropriate boundary layer resolution and provided adequate grid resolution away from the wall surface. Developing an approach that would facilitate the internal surfaces shown in Figure 3.8 proved to be time-consuming and challenging to accomplish. Multiple commercial grid generation software packages were investigated, but none were capable of creating an acceptable grid for the PRD analysis except for Pointwise. The benefit of Pointwise is that it offered complete control over the structured and unstructured grid generation process due to the bottoms-up approach; where the user specifies node distributions on connecting lines, generates surface domains, and then creates volume blocks. A multi-block hybrid grid approach was used as it effectively balanced the computational efficiency of structured grids and the flexibility of unstructured grids in especially difficult regions near the door opening.

The computational domain was broken up into a “background” grid that remained constant for all cases and a “door” grid that would allow for different geometrical configurations to be modeled as shown in Figure 3.9. The red block illustrates the door grid in Figure 3.9 while the blue, green, orange, and pink blocks comprise the background grid.

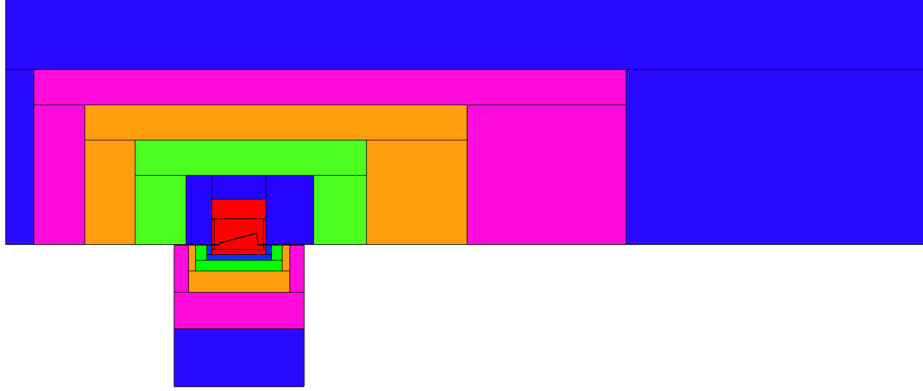


FIGURE 3.9. Multi-block grid approach with door block (red) and multi-block structured background grid.

The unique approach of separating the background and door grids allowed for multiple door grids to be generated for varying geometric configurations in a timely manner. The ability to accommodate door aspect ratios ranging from 0.75 to 1.5, door angles from 0–60°, and variations in hinge location without having to generate new background grids was essential to the success of the project. An overview of the strategies and motivations for the multi-block grid approach are discussed below.

3.3.1. BACKGROUND GRID. The background grid featured exclusively H-topology structured grids due to the rectangular nature of the freestream and plenum domains. Structured grids require fewer cells for a given node count and the cell faces are implicitly aligned with the flow thereby reducing discretization error. The H-grid topology allowed for unique coarsening strategies away from the door opening and complete control of the boundary layer meshing and stretching ratio. The grid coarsening strategy coarsened the grid away from the door. Note that the background grid was coarsened in streamwise and spanwise directions. The wall-normal spacing remained the same across all refinement blocks to ensure that the boundary layer was well resolved and to increase grid density upstream and downstream of the door opening near the bottom wall.

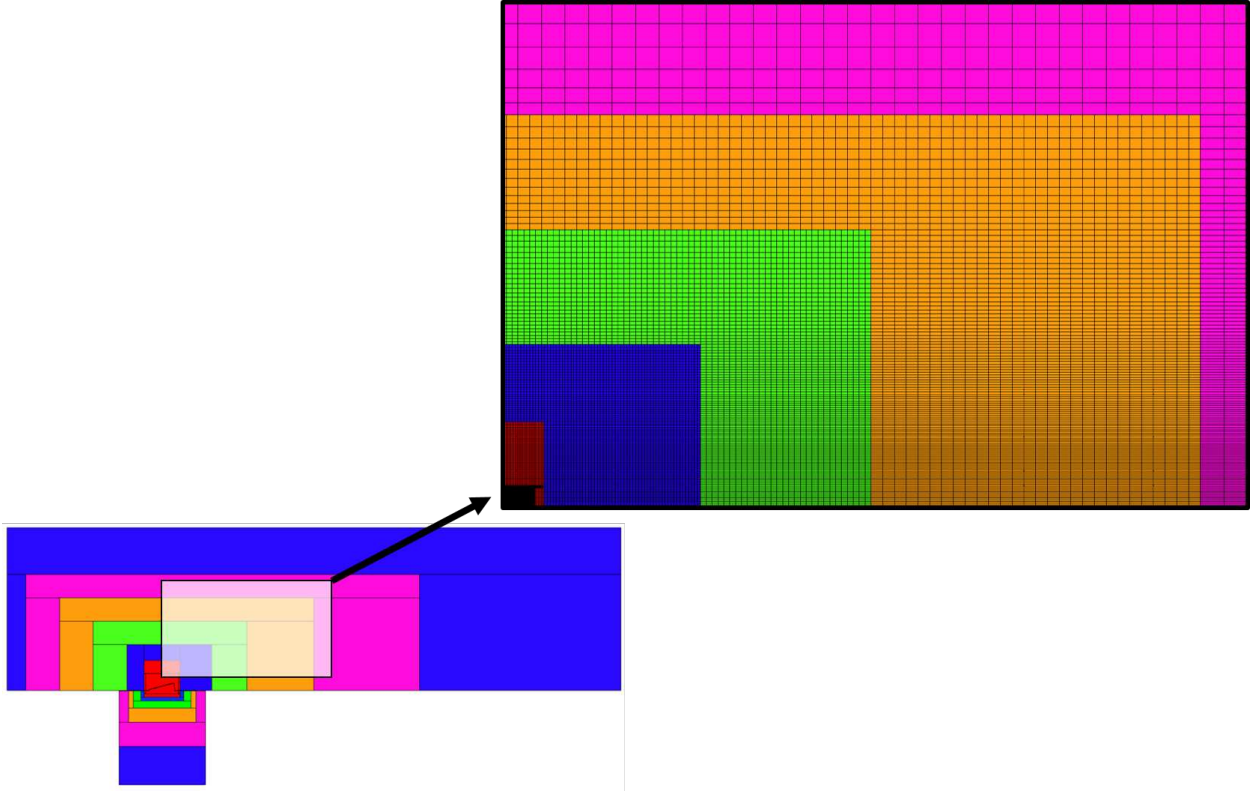


FIGURE 3.10. Symmetry plane grid coarsening strategy.

Figure 3.10 provides an example of the streamwise coarsening strategy on the symmetry plane. Each block, indicated by the blue, green, orange, and pink surfaces, was twice coarsened in the streamwise direction but maintained constant wall-normal spacing. Conformal interfaces exist between the streamwise interfaces for the coarsened blocks away from the door opening which resulted in high-quality isotropic cells near the door block region where it was necessary to resolve the complex flow features and anisotropic higher aspect ratio cells for the grid downstream of the door in the coarsest refinement blocks. The approach to develop the refinement regions was tedious and time consuming but provided appropriate grid distribution to adequately resolve the complex flow phenomena.

3.3.2. DOOR GRID. The door grid featured structured surface grids but unstructured volume grids. Structured volume grids work well on simple geometries or studies where

the focus is on a single geometric configuration, however, for the PRD analysis nearly 60 unique grids were required. Furthermore, small gaps and pinched corners were frequently encountered which would prove difficult and too complex for structured grids to handle in a time effective manner. The structured surface door grid was generated using a combination C-H topology as shown in Figure 3.11. The symmetry condition and the rounded corners of the baseline geometry lent itself to a C-topology. A similar approach was taken for the surface grid near the door opening. A C-topology grid was fitted around the perimeter of the door opening. A second block in the door block featured a C-H topology that would ensure that the door grid and background grids were point matched. The point matched behavior allowed for a simple flow through zonal boundary condition which minimized the interpolation error across the boundary in CFD++. The cell quality of the C-grid was improved by using the elliptic PDE smoothing in Pointwise to improve cell orthogonality and minimize equiangle skewness. Structured blocks were generated both above and below the unstructured blocks to reduce the total cell count in the unstructured door region. Structured grids were used on all domains interfacing the door block grid and the background grid.

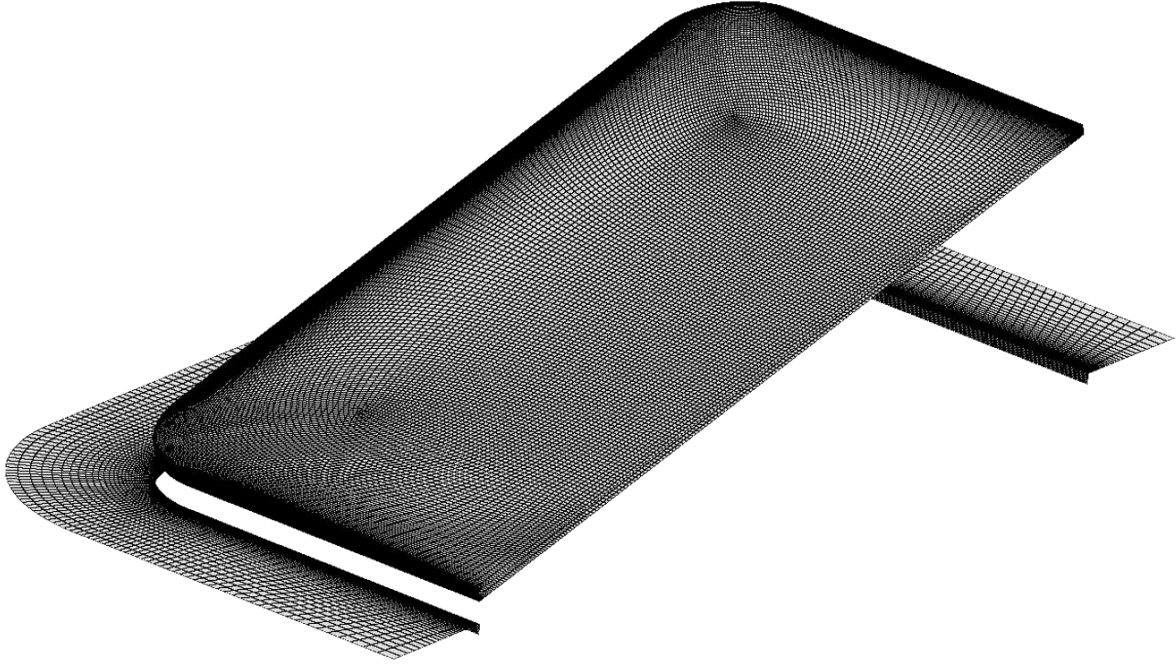
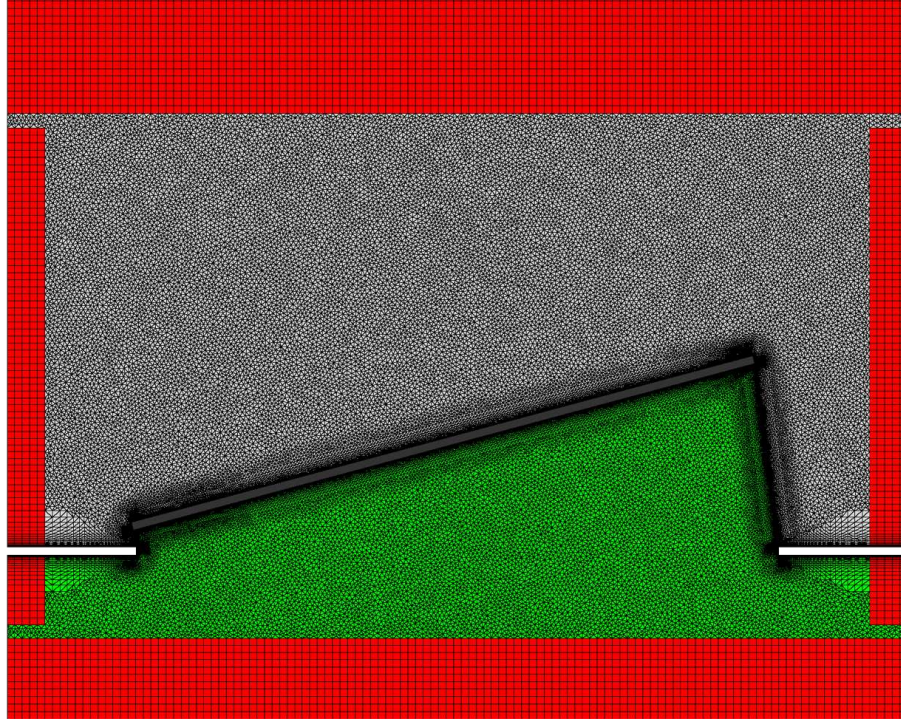


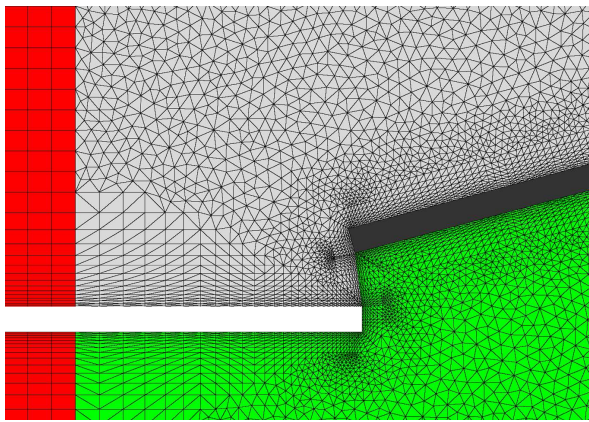
FIGURE 3.11. Structured surface grids on door.

Once structured surface grids were developed, unstructured volume grids were generated. The unstructured volume grids were generated using the advancing front 3D anisotropic tetrahedral extrusion (T-Rex) method in Pointwise. The T-Rex method extruded layers of high-quality tetrahedra from wall boundaries that were then post-processed into high-quality prism and hex elements in the boundary layer region. The post processing procedure resulted in improved accuracy and reduced cell count due to more cells implicitly aligned with the flow direction which improved the computational efficiency [29]. Point-to-point conformal interfaces existed between the structured background grids and unstructured surface grids. Pyramid cells were automatically generated and built off of the structured surface domain.

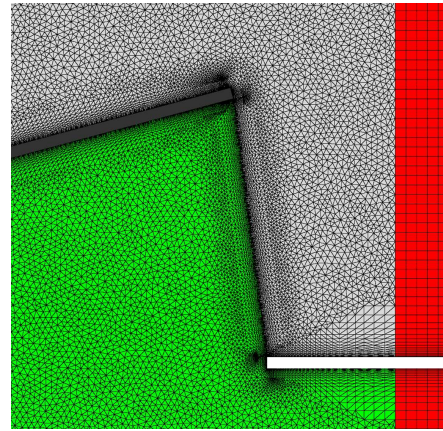
The most challenging aspect of generating the door grids was incorporating internal mass flow boundaries that maintained an appropriate boundary layer mesh. The ability to measure the mass flow rate through the internal boundaries located at the leading, lateral, and trailing edge surfaces made the work in this thesis novel.



(a) Overall view of door block grid



(b) Leading Edge Detail View



(c) Trailing Edge Detail View

FIGURE 3.12. Symmetry plane door block grid detail.

To accurately model the internal mass flow surfaces, a database surface was imported to ensure that the internal surfaces remained consistent for all studies. The unstructured volume grid had a tendency to warp the internal surfaces if the surfaces were not attached to a database. The database surfaces were created by importing structured surface grids based on the same geometry. Recall that in Figure 3.8, the internal flow surfaces were split

at the apex of the corner rounds and divided into leading, lateral, and trailing components. Grids were generated on the internal surfaces that would facilitate the boundary layer grids of the unstructured volume grid. The clever specification of meshing boundary conditions on the faces of the internal surface domains was used to generate wall boundary conditions on opposing sides of the internal surface. An unstructured volume grid was generated in two separate blocks, separated by the internal mass flow surfaces as indicated by the gray and green domains in Figure 3.12a. Note the increased grid density near the internal mass flow surfaces where the internal boundaries exist. The novel approach results in a boundary layer mesh that adheres to the internal database surfaces described above allow for the internal boundary to be specified as a zonal boundary condition within CFD++, and more importantly for the internal mass flow rates to be extracted.

3.3.2.1. *Grid Metrics.* The quality of the grids was measured by closely examining the equiangle skewness and stretching ratios. Equiangle skewness was kept below 0.85 for a majority of the grids, however at the intermediate mass flow surfaces, cells with skewness of 0.93 were observed. Stretching ratios were strictly kept to 1.2 for all cases examined. Note that the metrics observed were before the post-processing function of combining tetrahedra into layers of hexahedral and prismatic cells. At the time of this writing, no functionality existed in Pointwise to evaluate grid quality after the post-processing function was performed, thus making it difficult to determine grid quality metrics for the final grid before it was exported to CFD++.

3.3.2.2. *Door Grid Challenges.* Several challenges were encountered in developing the door grids. As mentioned previously, the most challenging aspect of the door grid was developing the internal mass flow rate surfaces for both hinge types. Several different approaches

across numerous commercial grid generation software packages were investigated. An alternate post-processing interpolation technique was developed that interpolated the solution onto a separate "solution grid" consisting of the desired internal surfaces. However, an unacceptable level of interpolation error was introduced. The internal boundary approach provides a dramatic improvement in the calculation of fluxes across the boundary and reduces the complicated post-processing operation in an external program. The leading edge gap between the door and the plenum and bottom wall domains of both the Gooseneck-hinge and Mid-hinge types required several cells to exist across the gap to ensure the leading edge jet flow behavior was adequately resolved. The grid density was increased along the internal mass flow rate surfaces to ensure that flow features were adequately resolved. Appropriately modeling the leading edge flow behavior was further complicated by the vertical hinge offset cases where the internal mass flow surface was at a sharp angle relative to the door surface and the plenum wall surface. The Mid-hinge type proved challenging near the lateral edge of the door where the door intersects with the gap between the top of the plenum domain and the bottom of the freestream domain. This was overcome by the clever specification of boundary conditions and increasing the grid density near the intersection point.

### 3.4. GRID REFINEMENT

A grid refinement study was performed by comparing two grids, a coarse grid that consisted of approximately 7 million cells with a wall  $y_1^+ \sim 25$ , and stretching ratio of 1.2, and a fine grid that contained approximately 70 million cells, a wall  $y_1^+ \sim 18$ , and a stretching ratio of 1.1. The fine grid was universally refined in all directions using a script developed in Pointwise [29]. Due to prior experience in developing grids for the PRD analysis, coarser grids were not generated as they would insufficiently resolve features in the critical regions. A

qualitative comparison of the Mach contours of the trailing edge jet is shown in Figure 3.13. The trailing edge jet is important in determining the exit mass flow rate the resulting flow behavior. The fine grid is illustrated in Figure 3.13a while the coarse grid is shown in Figure 3.13b where a qualitative comparison shows very similar behavior between both cases. The gradients of Mach number are shown in the zoomed in views as shown in Figure 3.13c and Figure 3.13d. A subtle amount of smearing is evident in the gradients of the exiting jet. The increased grid density of the fine grid results in better resolution of gradients, however, the coarse grid captures the same flow behavior and provides adequate resolution of the critical feature.

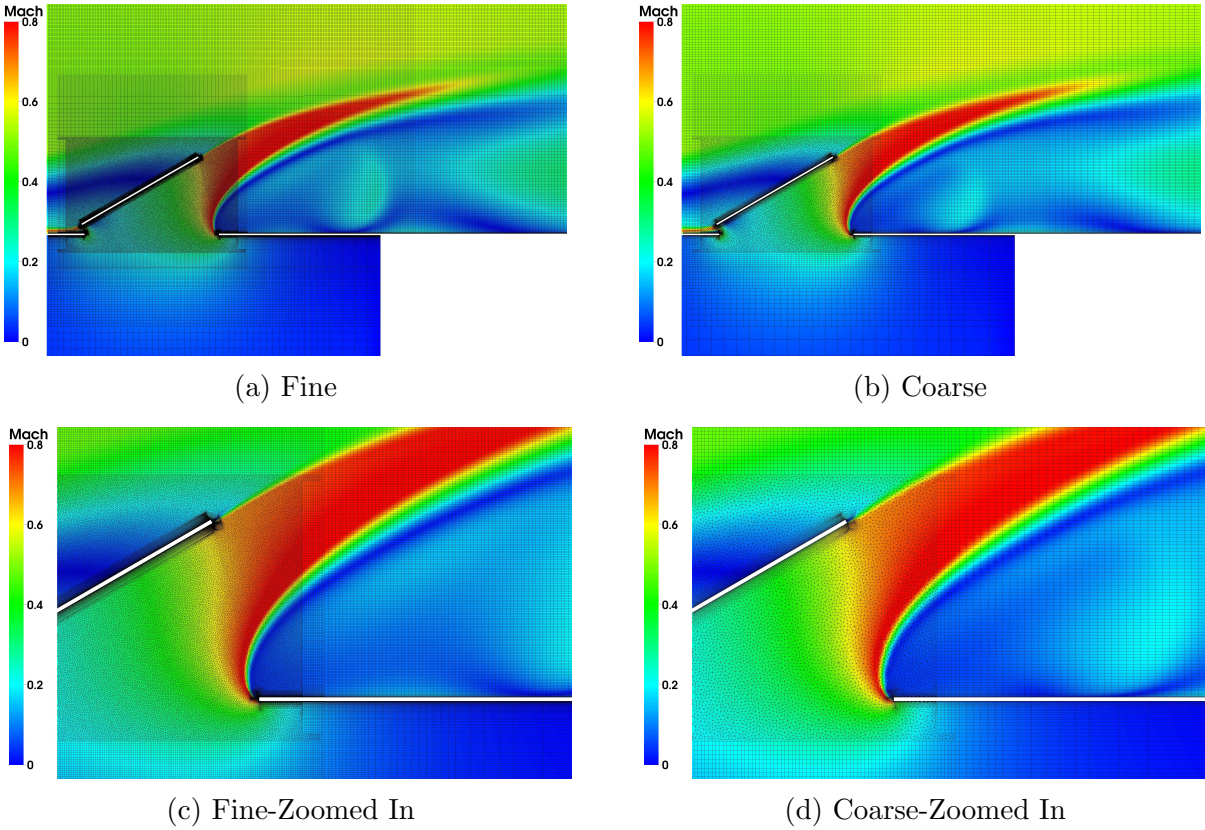


FIGURE 3.13. Refinement study comparison of Mach contours on symmetry plane of trailing edge jet.

Total temperature contours on the bottom wall surface are compared in Figure 3.14. An overview of the total temperature gradients is shown in Figure 3.14a and Figure 3.14b for the fine and coarse grids respectively. The fine grid resolves the high-temperature gradients better than the coarse grid particularly at the downstream portion of the high-temperature region. This is depicted at the leftmost high-temperature region where the increased dissipation associated with the coarse grid limits the resolution on the wall. Zoomed-in views near the door region are shown in Figure 3.14a and Figure 3.14b for the fine and coarse grids respectively. The fine grid provides a better resolution of the high-temperature gradients at the lateral edges of the door; however, the coarse grid adequately predicts the wall surface temperature contours.

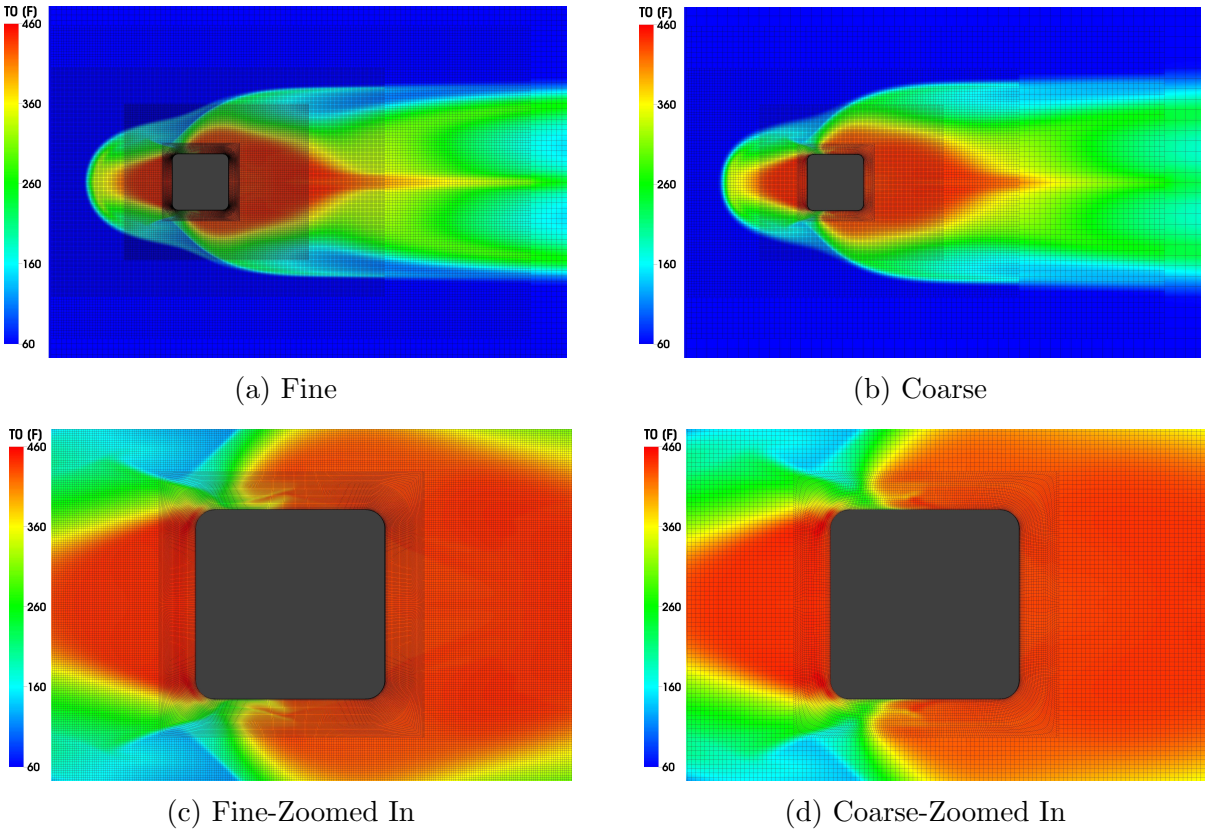


FIGURE 3.14. Refinement study comparison of total temperature contours on freestream bottom wall.

While qualitative comparisons provide a visual comparison of the grid refinement, a quantitative comparison is equally as important. The refinement study compared exit mass flow rate, moment, and thrust characteristics as shown in Table 3.2, Table 3.3, and Table 3.4, respectively. The exit mass flow rate through the leading, lateral, and trailing surfaces was examined. The greatest deviation between the coarse grid and the fine grid was in the leading edge mass flow rate where the coarse grid over-predicted the exit mass flow by 2.75%. Note that the exit mass flow rate through the leading edge surface contributes to less than 5% of the overall exit mass flow rate. The total exit mass flow rate, total moment, and thrust force were found to be within 0.13%, 0.25%, and 0.07%, respectively.

The coarse grid was determined to be grid independent based on qualitative and quantitative comparisons with the fine grid. Given the computational cost and negligible loss in solution accuracy, the coarse grid was used for all PRD simulations.

TABLE 3.2. Mass flow rate comparison for grid refinement study.

<b>Case</b>	<b>Grid Size</b>	$y_1^+$	<b>Leading [kg/s]</b>	<b>Lateral [kg/s]</b>	<b>Trailing [kg/s]</b>	<b>Total [kg/s]</b>
<b>Fine</b>	$70 \times 10^6$	18	0.327	3.80	3.30	7.45
<b>Coarse</b>	$7 \times 10^6$	25	0.336	3.75	3.38	7.44
<b>Difference</b>			2.75%	1.3%	2.4%	0.13%

TABLE 3.3. Hinge moment comparison for grid refinement study.

Case	Grid Size	$y_1^+$	Opening [N-m]	Closing [N-m]	Total [N-m]
Fine	$70 \times 10^6$	18	872.5	715.1	157.3
Coarse	$7 \times 10^6$	25	872.0	715.0	157.0
<b>Difference</b>			0.06%	0.01%	0.19%

TABLE 3.4. Door force comparison for grid refinement study.

Case	Grid Size	$y_1^+$	Thrust	Lift
Fine	$70 \times 10^6$	18	577.3	1003.9
Coarse	$7 \times 10^6$	25	576.8	1002.9
<b>Difference</b>			0.07%	0.1%

## CHAPTER 4

# RESULTS AND DISCUSSION

### 4.1. COMPREHENSIVE PARAMETER STUDY HINGE TYPE COMPARISON

A comprehensive parameter study was carried out to examine the moment, discharge, thrust, and surface temperature characteristics across a range of freestream, plenum, and geometrical configurations for the Gooseneck-hinge and Mid-hinge types. The parameter study was developed in collaboration with engineers at Boeing based on previous PRD research investigations. The comprehensive study investigated six parameters including freestream altitude, freestream Mach number, plenum gauge pressure, plenum temperature, door aspect ratio, and vertical hinge offset, for the Gooseneck-hinge and Mid-hinge types and door angles ranging from 0–60° in 15° increments. A summary of all cases involved in the parameter study is shown in Table 4.1. A baseline analysis was carried out for the Gooseneck-hinge and Mid-hinge types across door angles ranging from 0–60° in 15° increments. The baseline analysis, denoted by the † symbol in Table 4.1, assumed sea level freestream altitude, freestream Mach number of 0.5, plenum pressure of 5 psig, plenum temperature of 450°F, door aspect ratio of one, and no vertical hinge offset. Subsequent cases in the parameter study varied a single parameter to examine the impact of the changing parameter on the solution. Only three varied parameters are shown in many of the quantitative results shown in Section 4.1 to improve clarity for the reader.

TABLE 4.1. Details of comprehensive parameter study.

<b>Parameter</b>	<b>Condition</b>
<b>Freestream altitude (kft)</b>	-2, 0 <sup>†</sup> , 10, 15, 25, 35, 45
<b>Freestream Mach</b>	0, 0.1, 0.25, 0.4, 0.5 <sup>†</sup> , 0.6, 0.75, 0.9
<b>Plenum pressure (psig)</b>	0, 1, 3, 4, 5 <sup>†</sup> , 6, 7, 8, 10, 12
<b>Plenum temperature (°F)</b>	-80, 450 <sup>†</sup> , 1200, 1500
<b>Door aspect ratio</b>	0.75, 1.0 <sup>†</sup> , 1.25, 1.5
<b>Vertical hinge offset (in)</b>	0 <sup>†</sup> , 0.75

4.1.1.1. HINGE MOMENTS. The moment created about the hinge is an important parameter in evaluating PRD performance. Increased moments necessitate higher strength materials and heavier hinge and latch mechanisms. An understanding of the hinge moment behavior allows for the PRD designer to optimize the hinge and latch mechanism for the expected operating conditions. The following section provides a comparison of hinge moments for variations in freestream, plenum, and geometric configurations for door angles ranging from 15–60°.

(a) Freestream altitude

(b) Freestream Mach

(c) Plenum pressure

(d) Plenum temperature

(e) Door aspect ratio

(f) Vertical hinge offset

FIGURE 4.1. Total hinge moment comparison for Gooseneck-hinge (square) and Mid-hinge (diamond) types for variations in freestream, plenum, and geometric configurations.

Figure 4.1 the total moment acting about the hinge for varying freestream altitude, freestream Mach number, plenum pressure, door aspect ratio, and vertical hinge offset conditions. The convention for the positive moment is defined as the door opening. For all figures, the Goosneck-hinge type is indicated by the while the Mid-hinge hinge type is indicated by the open diamond. It is evident that the the greatest hinge moments occurred at the minimum and maximum door angles of  $0^\circ$  and  $60^\circ$ , respectively. The opening moment is maximized at the  $0^\circ$  door angle while the closing moment is maximized at the  $60^\circ$  door angle. As the door angle is increased, the positive total moment created by the static pressure differential decays and the negative total moment due to the freestream dynamic pressure dominates. The equilibrium angle where the opening and closing moments are balances is an important parameter for PRD design and is discussed in further detail in Section 4.1.2. The Goosneck hinge type consistently has a greater magnitude of the total moment acting on the door due to the longer moment arm and distribution of forces acting on the door. Figure 4.2a illustrates that the increased plenum pressure acts on the entire bottom surface of the door thus, increasing the opening moment. However, for the Mid-hinge type, the opening moment forces act both downstream of the hinge on the bottom side of the door and upstream of the hinge on the top side of the door as shown in Figure 4.2b. Additionally, it is apparent that the entire top surface of the Goosneck-hinge type door area extends into the freestream domain while only the door area downstream of the hinge extends into the domain for the Mid-hinge type.

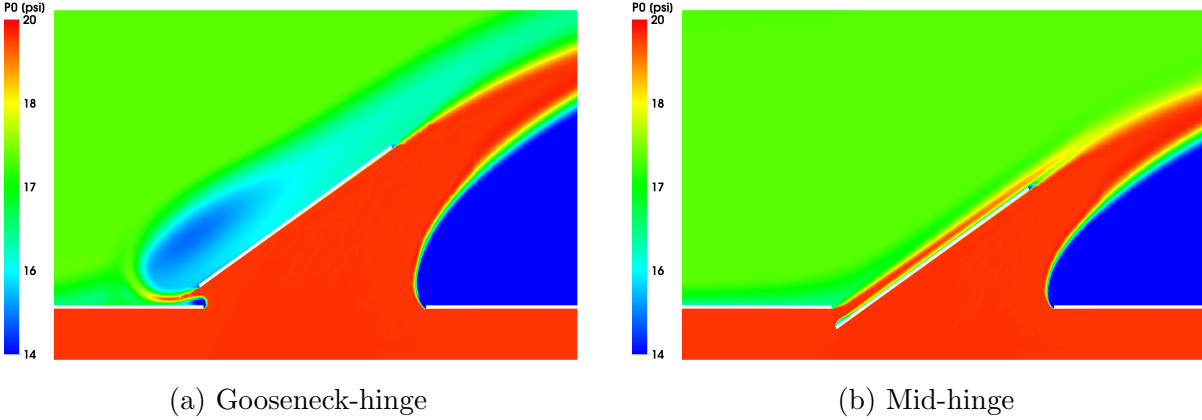


FIGURE 4.2. Total pressure contours comparing the Gooseneck-hinge and Mid-hinge geometries on the symmetry plane at a door angle of  $30^\circ$  and baseline operating conditions.

Figure 4.1a compares the total moment behavior for door angles ranging from  $15^\circ$  to  $60^\circ$  for the Gooseneck-hinge and Mid-hinge types at varying freestream altitudes. The symbol color corresponds to variations in freestream altitude. The red symbols correspond to sea level altitude, the blue symbols correspond to an altitude of 25,000 ft., and the green symbols correspond to an altitude of 45,000 ft. Additional altitude cases were simulated but were not included in the figure to improve reader clarity. The figure illustrates that an increase in freestream altitude results in a greater total moment due to the decreased freestream density and corresponding decreased freestream momentum which contribute to a reduced closing moment. For the Gooseneck-hinge type at  $30^\circ$ , the increase in altitude from sea level to 45,000 ft. corresponds to a 39% increase in the total moment. At the  $15^\circ$  door angle, the total moments for the Mid-hinge type are collapsed around a total moment near 157 N·m, whereas at the  $60^\circ$  door angle, the total moments vary from -47 N·m at sea level altitude to 40 N·m at an altitude of 45,000 ft. representing. The Gooseneck-hinge type exhibits greater magnitudes of the total moment. At sea level conditions, the Gooseneck-hinge type total moment is 1.9 times larger than that for the Mid-hinge type. Freestream altitude has an

impact on the total moment behavior with higher altitudes corresponding to increased total moments, particularly at higher door angles.

Figure 4.1b compares the total moment behavior for door angles ranging from  $15^\circ$  to  $60^\circ$  for the Gooseneck-hinge and Mid-hinge types at varying freestream Mach numbers. The symbol color corresponds to variations in freestream Mach number. The red symbols correspond to a freestream Mach number of 0.1, the blue symbols correspond to a Mach number of 0.5, and the green symbols correspond to a Mach number of 0.9. Additional Mach number cases were simulated but were not included in the figure to improve reader clarity. The figure shows that increasing freestream Mach number corresponds to an increase in freestream momentum acting on the top surface of the door resulting in a greater closing moment thus a greater negative total moment. Similar to the variations in freestream altitude, both types are more sensitive to changes in freestream Mach number at larger door angles compared to smaller angles. For the Gooseneck-hinge type at  $15^\circ$ , the total moment ranges from 283 N·m at a freestream, Mach number of 0.1, to 161 N·m at a freestream Mach number of 0.9. At the  $60^\circ$  door angle, the total moment ranges from 67 N·m at a freestream Mach number of 0.1 to -662 N·m at a freestream Mach number of 0.9. It is apparent that the increased door angle corresponds to a highly negative total moment. As more of the top surface of the door is exposed to the freestream flow, the greater the closing moment. The increased exposed freestream area of the Gooseneck-hinge type corresponds to a greater negative total moment. At the  $60^\circ$  door angle, the Gooseneck-hinge total moment is 2.2 times greater than the Mid-hinge total moment. Freestream Mach number has an impact on the total moment behavior with increasing freestream Mach number corresponding to greater closing moments and negative total moments, particularly at higher door angles.

Figure 4.1c compares the total moment behavior for door angles ranging from  $15^\circ$  to  $60^\circ$  for the Gooseneck-hinge and Mid-hinge types at varying plenum pressures. The symbol color corresponds to variations in plenum pressure. The red symbols correspond to a plenum pressure of 1 psig, the blue symbols correspond to a plenum pressure of 5 psig, and the green symbols correspond to a plenum pressure of 12 psig. Additional plenum pressure cases were simulated but were not included in the figure to improve reader clarity. The figure illustrates that an increase in plenum pressure results in a greater total moment due to the increased opening moment. With increasing door angle, the impact of the total moment decays. The effect of plenum pressure on the opening moment is apparent at a door angle of  $15^\circ$  for the Gooseneck-hinge type where for a plenum pressure of 12 psig the total moment is 24 times greater than the total moment for a plenum pressure of 1 psig. At the  $60^\circ$  door angle, the total moment at a plenum pressure of 1 psig is 8.6+ times greater than then total moment for a plenum pressure of 12 psig. Note that the negative total moment is greater for the lower plenum pressure case. Hinge type has an impact on the total moment behavior with the Gooseneck-hinge type having a total moment that is 1.9 times greater than the Mid-hinge type. Increasing plenum pressure corresponds to increased total moments particularly at lower door angles.

Figure 4.1d compares the total moment behavior for door angles ranging from  $15^\circ$  to  $60^\circ$  for the Gooseneck-hinge and Mid-hinge types at varying plenum temperatures. The symbol color corresponds to variations in plenum temperature. The red symbols correspond to a plenum temperature of  $-80^\circ\text{F}$ , the blue symbols correspond to a plenum temperature of  $450^\circ\text{F}$ , and the green symbols correspond to a plenum temperature of  $1200^\circ\text{F}$ . Additional plenum temperature cases were simulated but were not included in the figure to improve reader

clarity. Variations in plenum temperature did not have an impact on the total moment behavior. As mentioned previously, the Gooseneck-hinge type exhibited greater magnitudes of the total moment across all door angles. For a door angle of  $15^\circ$ , the Gooseneck-hinge type had a total moment that was 1.9 times greater than the Mid-hinge type. Variations in plenum temperature do not have an appreciable impact on the total moments behavior.

Figure 4.1e compares the total moment behavior for door angles ranging from  $15^\circ$  to  $60^\circ$  for the Gooseneck-hinge and Mid-hinge types at varying door aspect ratios. The symbol color corresponds to variations in door aspect ratio. The red symbols correspond to a door aspect ratio of 0.75, the blue symbols correspond to a door aspect ratio of 1, and the green symbols correspond to a door aspect ratio of 1.5. Additional door aspect ratio cases were simulated but were not included in the figure to improve reader clarity. The figure shows that increasing door aspect ratio corresponds to a greater total moment due to the longer chord length extending into the freestream flow. At a door angle of  $15^\circ$ , the  $AR = 1.5$  case had a total moment that was 1.2 times greater than the  $AR = 0.75$  case. An equilibrium point for the total moments exists for all aspect ratios near  $30^\circ$  for the Gooseneck-hinge type and  $47^\circ$  for the Mid-hinge type. It is important to remind the reader that door area remained constant for all door aspect ratio cases. Door aspect ratio has an impact on the total moment behavior with higher aspect ratio doors corresponding to increased total moments, particularly across all door angles.

Figure 4.1f compares the total moment behavior for door angles ranging from  $15^\circ$  to  $60^\circ$  for the Gooseneck-hinge and Mid-hinge types at varying vertical hinge offsets. The symbol color corresponds to variations in vertical hinge offset. The red symbols correspond to no vertical hinge offset and the blue symbols correspond to a vertical hinge offset of 0.75

inches. Vertical hinge offset decreases the total moment behavior compared with non-offset, however, the difference is small. For the Gooseneck-hinge type at  $15^\circ$ , the total moment for the non-offset case was 3% greater than the offset case. Similarly, for the Mid-hinge type the non-offset case had a total moment that was 5% greater than the offset case. As mentioned previously, the Gooseneck-hinge type had a total moment that was 1.9 times greater than the Mid-hinge type. Vertical hinge offset had an impact, though small, on the total moment behavior.

The total moment behavior was the most sensitive to variations freestream altitude, freestream Mach number, plenum pressure, and door aspect ratio. Variation in plenum temperature and vertical hinge offset did not have an appreciable impact on the total moment behavior. Variations in freestream operating conditions have a greater impact on the total moment at larger door angles while changes in plenum pressure have a greater impact at smaller door angles. Hinge location plays a significant role in the magnitudes of the total moments, with the Gooseneck-hinge type having a greater total moment than the Mid-hinge type. The in-depth analysis of the total hinge moment behavior provides valuable information to the PRD designer who can develop optimized hinge assemblies that can withstand worst case loading scenarios.

4.1.2. HINGE MOMENT EQUILIBRIUM. While having a solid understanding of the hinge total moments is important, understanding the hinge moment equilibrium angle is paramount to a PRD analysis. Recall that the hinge moment equilibrium angle is where the door achieves a trimmed balance and the opening and closing moments are in equilibrium. The equilibrium moment angle is an important parameter as it dictates the steady-state door angle for evaluating discharge and surface temperature characteristics.

(a) Freestream altitude

(b) Freestream Mach

(c) Plenum pressure

(d) Plenum temperature

(e) Door aspect ratio

(f) Vertical hinge offset

FIGURE 4.3. Total moment equilibrium angle comparison for Gooseneck-hinge and Mid-hinge types.

Figure 4.1 compares the hinge moment equilibrium angles for varying freestream altitude, freestream Mach number, plenum pressure, door aspect ratio, and vertical hinge offset conditions. For all figures, the open blue box indicates the Gooseneck-hinge type and the

open red diamond indicates the Mid-hinge type. Similar trends exist for both Gooseneck-hinge and Mid-hinge types. The Mid-hinge type has an equilibrium moment angle that is consistently 3–5° greater than the Gooseneck-hinge type.

Figure 4.3a compares the hinge moment equilibrium angles for freestream pressure altitudes ranging from -2,000 ft. to 45,000 ft. Increasing freestream altitude corresponds to a nearly linear increase in equilibrium angle for freestream altitudes less than 25,000 ft., above which, a non-linear increase in equilibrium angle is observed. The non-linear equilibrium angle behavior at freestream altitudes of 25,000 ft. or greater are attributed to a complex shock structure that develops in the leading, lateral, and trailing edge openings. Details of the complex shock structure are discussed in Section 4.1.3. The figures show that the equilibrium moment angle ranges from 45° to 70° at freestream altitudes of -2,000 ft. and 45,000 ft., respectively. Increasing freestream altitude corresponds to increasing hinge moment equilibrium angles.

Figure 4.3b compares the hinge moment equilibrium angles for freestream Mach numbers ranging from 0 to 0.9. The figure illustrates that increasing Mach number corresponds to a decrease in equilibrium moment angle. The total moment equilibrium angle is near 85° at a freestream Mach number of 0 and near 22° at a freestream Mach number of 0.9 for the Gooseneck-hinge type. The reduction in equilibrium angle illustrates the impact that the freestream momentum at higher Mach numbers has on the total moment behavior.

Figure 4.3c compares the hinge moment equilibrium angles for plenum pressures ranging from 1 psig to 12 psig. Increasing plenum pressure results in a non-linear increase in equilibrium moment angle that approaches an asymptotic value near 60° at high pressures. The asymptotic relationship is explained by the increase in the closing moment at larger

door angles. As mentioned previously, plenum pressure has the greatest impact at lower door angles. The figure illustrates that the equilibrium moment angles range from  $21^\circ$  at 1 psig to  $60^\circ$  at 12 psig. Increasing plenum pressure corresponds to an increase in the hinge moment equilibrium angles.

Figure 4.3d compares the hinge moment equilibrium angles for plenum temperatures ranging from  $-80^\circ\text{F}$  to  $1500^\circ\text{F}$ . Plenum temperature does not have an impact on the hinge moment equilibrium angles. The equilibrium angle was near  $46^\circ$  for the Gooseneck-hinge type and near  $49^\circ$  for the Mid-hinge type.

Figure 4.3e compares the hinge moment equilibrium angles for door aspect ratios ranging from 0.75 to 1.5. The equilibrium moment angle decreases with increasing door aspect ratio. For the Gooseneck-hinge type, the equilibrium angle for a door aspect ratio of 0.75 is near  $47^\circ$  while for an aspect ratio of 1.5 the equilibrium angle is near  $44^\circ$ . Similar behavior is observed for the Mid-hinge type where the equilibrium angle ranges from  $51^\circ$  to  $47^\circ$  at aspect ratios of 0.75 and 1.5, respectively. Recall that in Figure 4.1e door aspect ratios achieve an equilibrium point for all door aspect ratios near the moment equilibrium angle which explains the small variation in equilibrium angles. Door aspect ratio has an impact, though small, on the hinge moment equilibrium angle.

Figure 4.3f compares the hinge moment equilibrium angles for vertical hinge offset ranging from no offset to an offset of 0.75 inches. Vertical hinge offset corresponds to a subtle increase in the equilibrium angle. For the Gooseneck-hinge type, the equilibrium angle is near  $45^\circ$  for the non-offset case and near  $46^\circ$  for the 0.75-inch offset case.

The hinge moment equilibrium angle is the most sensitive to variations in freestream altitude, freestream Mach number, plenum pressure, and door aspect ratio. Changes in plenum

temperature and vertical hinge offset did not have an appreciable impact on the equilibrium moment angle. Typical values for the hinge moment equilibrium angle range from 40–60° depending on operating condition. Information obtained from the parameter study for the hinge moment equilibrium angle provides valuable input for aircraft designers to optimize hinge geometry and have an understanding of where the PRD will settle once transient flow dynamics settle out for analyzing the discharge and surface temperature characteristics. Furthermore, the PRD designer can specify door opening limits that are inclusive of the hinge moment equilibrium angle.

4.1.3. EXIT MASS FLOW RATE. One of the primary functions of a PRD is to relieve internal pressure as effectively as possible. It is necessary for the PRD designer to have a good understanding of the exit mass flow rate behavior depending on freestream, plenum, and geometric conditions. Previous studies by Pratt et. al. [7] and Vick [6] have not been able to fully characterize exit mass flow rate behavior; instead, they assumed a minimum calculated flow area and neglected flow that exits laterally from the door opening. The current work developed a novel approach to modeling internal surfaces to extract mass flow rates from the CFD simulation thus providing insight into the exit mass flow rate characteristics from the leading, lateral, and trailing edge surfaces. Comparisons for the exit mass flow rate, discharge coefficient, non-dimensional effective area for variations in freestream, plenum, and geometric configurations for door angles ranging from 15° to 60° are discussed below.

(a) Freestream altitude

(b) Freestream Mach

(c) Plenum pressure

(d) Plenum temperature

(e) Door aspect ratio

(f) Vertical hinge offset

FIGURE 4.4. Exit mass flow rate comparison for Gooseneck-hinge and Mid-hinge types.

Figure 4.4 compares the exit mass flow rate for varying freestream altitude, freestream Mach number, plenum pressure, door aspect ratio, and vertical hinge offset conditions. The convention for the total exit mass flow rate is the sum of the mass flow rate exiting the

plenum and entering the plenum domain. The total exit mass flow rate is the sum of the mass flow rate through the leading, lateral, and trailing edge surfaces. For all figures, the open box indicates the Gooseneck-hinge type and the open diamond indicates the Mid-hinge type. The figures show that exit mass flow rate increases with increasing door angle. For the Gooseneck-hinge type, the exit mass flow rate approaches a maximum near the  $60^\circ$  door angle. The Mid-hinge approaches a maximum exit mass flow rate that is outside of the  $60^\circ$  upper bound of the CFD simulations but is approximated to be near a door angle of  $75^\circ$ . The figures also show that the Gooseneck-hinge type consistently has a greater exit mass flow rate due to the increased exit flow area. A detailed discussion of the exit mass flow rate characteristics for variations in freestream, plenum, and geometric conditions is provided below.

Figure 4.4a compares the exit mass flow rate behavior for varying freestream altitudes. The figure illustrates that an increase in freestream altitude results in a decrease in exit mass flow rate. Due to the lower density and decreased static pressure associated with increased altitude, the flow is choked due to an expansion fan at the leading, lateral, and trailing edges which limits the flow exiting the plenum. Figure 4.5 compares the Mach number contours for the Mid-hinge geometry on the symmetry plane at  $30^\circ$  for sea level altitude as shown in Figure 4.5a and for an altitude of 45,000 ft. as shown in Figure 4.5b. Detailed views of the Mach contours are shown in Figure 4.5c and Figure 4.5d for freestream altitudes of sea level and 45,000 ft., respectively.

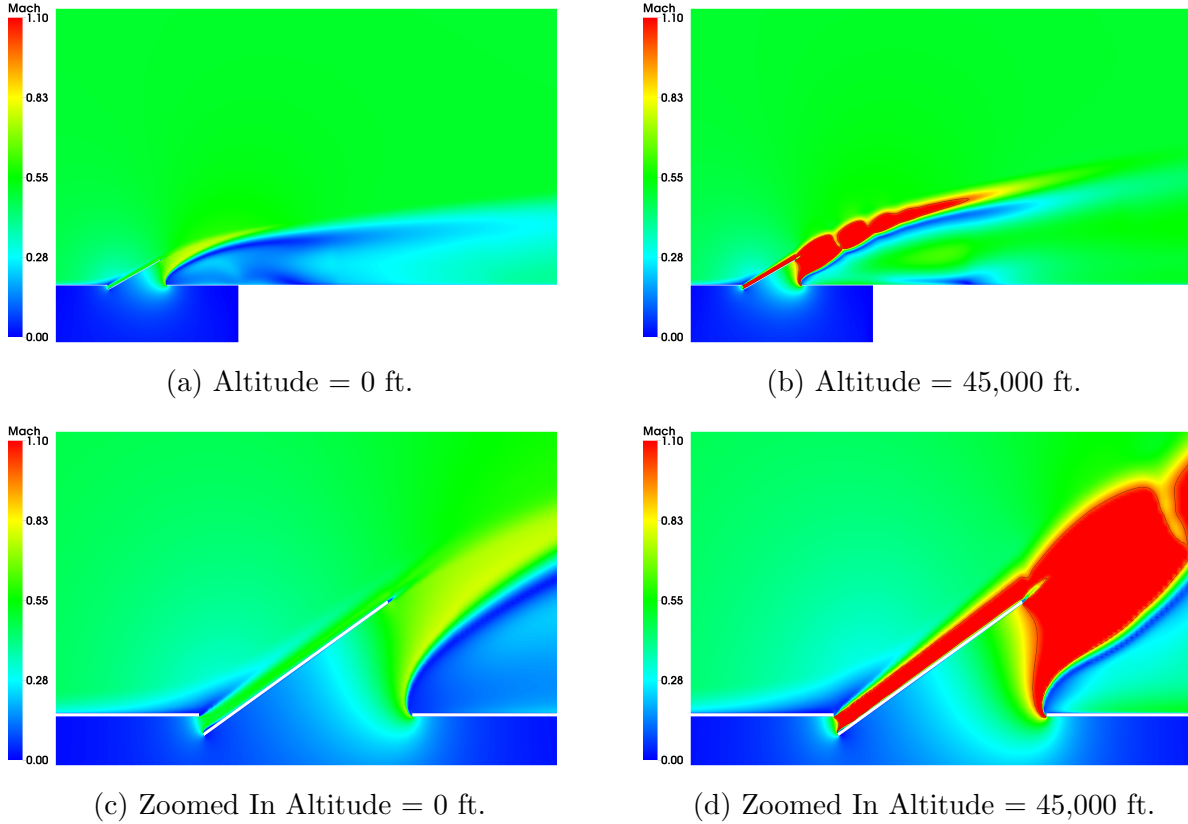


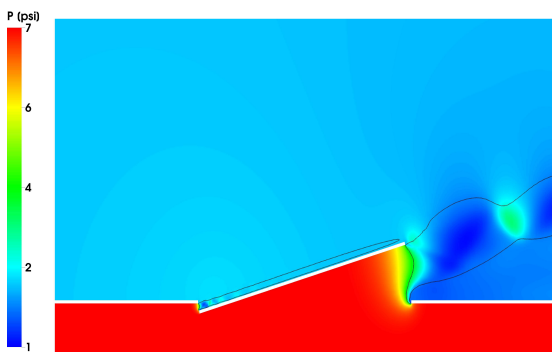
FIGURE 4.5. Contours of Mach number on the symmetry plane for variations in freestream altitude at  $30^\circ$  for Mid-hinge type. Note the dashed black contour line of  $Ma_\infty = 1$ .

Figure 4.6 compares static pressure contours on the symmetry plane for variations in door angle for the Mid-hinge type at an altitude of 45,000 ft. Note how the choked flow location, indicated by the black  $Ma_\infty = 1$  contour line, varies with increasing door angle. At the leading edge, the complex flow structure chokes the flow between the bottom of the gap between the plenum and freestream domain and the top surface of the door. With increasing angle, the structure transitions from the leading edge of the door to a point near the hinge location. At the trailing edge jet, the choked flow structure is normal to the bottom surface of the door and extends to the lower part of the gap between the plenum and freestream domains. With increasing door angle, the choked flow point shifts from the trailing edge of the door (Figure 4.6b) towards the hinge near the middle of the door (Figure 4.6e).

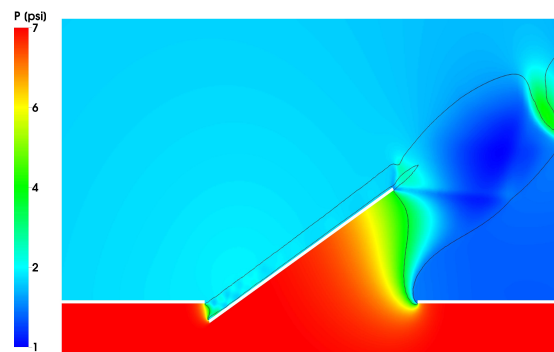
Figure 4.6a illustrates the complex flow structure in the trailing edge jet as indicated by the increased static pressure regions and the repeated expansion and contraction of the  $Ma_\infty = 1$  contour line. Increased altitude corresponds to a decrease in exit mass flow rate. The development of complex flow structures such as expansion and contraction fans near the door opening restrict the exit mass flow rate leaving the plenum.



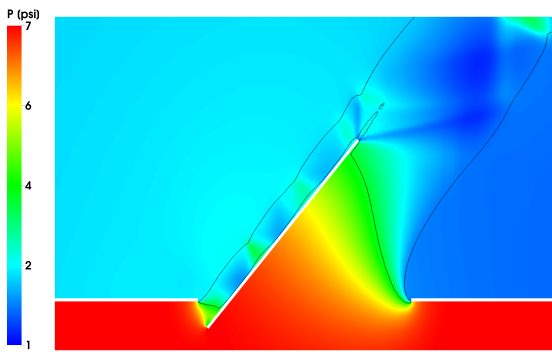
(a) Overall View 15°



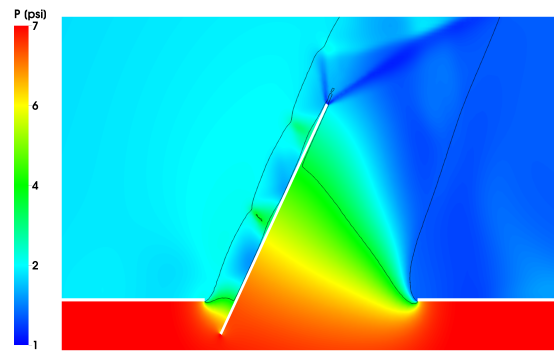
(b) 15°



(c) 30°



(d) 45°



(e) 60°

FIGURE 4.6. Contours of static pressure on the symmetry plane for variations in door angle at a freestream altitude of 45,000 ft. for Mid-hinge type. Note the dashed black contour line of  $Ma_\infty = 1$ .

Figure 4.4b compares the exit mass flow rate behavior for varying freestream Mach numbers. The figure shows that the maximum exit mass flow rate occurs for a freestream Mach number of 0.5 for both types. At lower door angles, Mach number has a minimal impact on the exit mass flow rates, however, at larger door angles a greater variation in exit mass flow rate is observed. For the Gooseneck-hinge type at a door angle of  $15^\circ$ , the mass flow rates vary by 2% while at a door angle of  $60^\circ$  the exit mass flow rates vary by 10% for the entire range of freestream Mach numbers. The relatively small range of exit mass flow rates is unexpected as the exit flow behavior is dramatically different as shown in Figure 4.7. The figure compares streamlines colored by total temperature for  $Ma_\infty = 0.1$  (left) and  $Ma_\infty = 0.9$  (right). Figure 4.7a illustrates that at  $Ma_\infty = 0.1$ , the leading and lateral edge flow behavior is unconstrained, and the freestream flow has a minimal impact on the flow exiting the plenum. At  $Ma_\infty = 0.9$ , as shown in Figure 4.7b, the leading edge exit flow is reversed and the freestream flow redirects flow exiting the lateral edge rearward, and reduces the height of the trailing edge vortices. Despite the difference in flow characteristics, the exit mass flow rates remained similar.

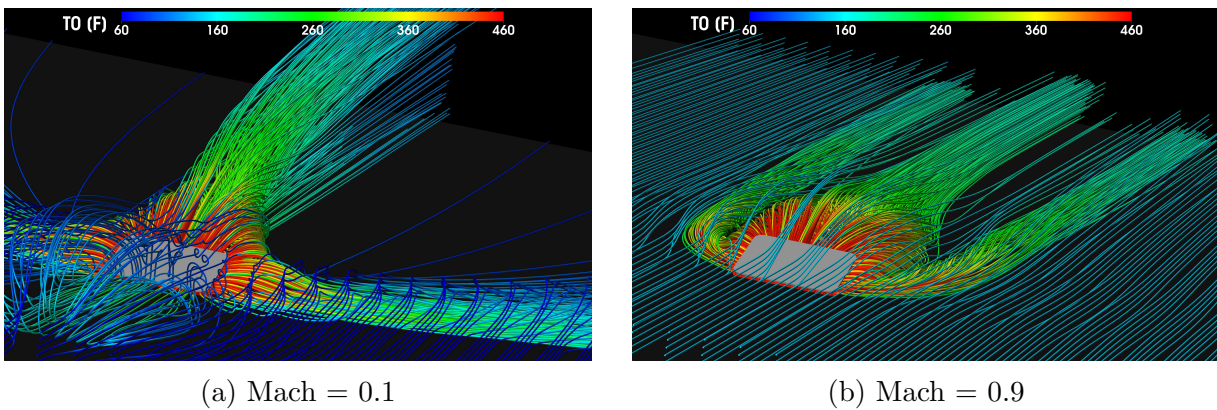


FIGURE 4.7. Streamlines colored by total temperature for freestream Mach number variation at  $15^\circ$  for Gooseneck-hinge type.

Figure 4.4c compares the exit mass flow rate behavior for varying plenum pressures. The symbol color corresponds to variations in plenum pressure. The figure illustrates that increasing plenum pressure results in an increase in exit mass flow rate. The exit mass flow rate for the Gooseneck-hinge type at  $60^\circ$  is 3.2 times greater at a plenum pressure of 12 psig compared to a plenum pressure of 1 psig. Exit mass flow rate has a strong correlation with plenum pressure.

Figure 4.4d compares the exit mass flow rate behavior for varying plenum temperatures. The symbol color corresponds to variations in plenum temperature. The figure illustrates that increasing plenum temperature results in a decrease in exit mass flow rate. The exit mass flow rate for the Gooseneck-hinge type at  $60^\circ$  is 2.1 times greater at a plenum temperature of  $-80^\circ\text{F}$  compared to a plenum temperature of  $1500^\circ\text{F}$ . The decreased density associated with the  $-1500^\circ\text{F}$  plenum temperature illustrates the impact that density has on the exit mass flow rate.

Figure 4.4e compares the exit mass flow rate behavior for varying door aspect ratios. The figure shows that increasing door aspect ratio corresponds to an increased exit mass flow rate. The increased chord length associated with the  $\text{AR} = 1.5$  case results in greater exit mass flow rate as illustrated by the 17% increase in exit mass flow rate compared with the  $\text{AR} = 0.75$  case for the Gooseneck-hinge type. For the Gooseneck-hinge type at a door of angle of  $60^\circ$ , the exit mass flow rate for all door aspect ratios approaches a constant near 10 kg/s. The Mid-hinge type appears to follow a similar trend, but data for door angles past  $60^\circ$  is not available. Observing the impact of door aspect ratio on the exit mass flow rate is an important observation for the PRD designer where at lower door angles increasing aspect

ratio allows for greater exit mass flow rates while at high door angles a near constant mass flow rate is observed.

Figure 4.4f compares the exit mass flow rate behavior for varying vertical hinge offset. The figure shows that vertical hinge offset corresponds to a subtle increase in exit mass flow rate. For the Gooseneck-hinge type at  $60^\circ$ , the vertically hinge offset case result in a 2% greater exit mass flow rate compared to the non-offset case. The Gooseneck-hinge type exit mass flow rate is 1.4 times greater than the Mid-hinge type at  $15^\circ$ , but only 1.1 times greater at  $60^\circ$ .

An understanding of the exit mass flow rate behavior is imperative to the analysis and design of PRD's. The exit mass flow rate is the most sensitive to variations in plenum pressure, plenum temperature, freestream altitude, and door aspect ratio. Increasing plenum pressure and decreasing plenum temperature correspond to the greatest exit mass flow rates. Complex shock structures observed in the variation of freestream altitude limit the exit mass flow rates, particularly at freestream altitudes greater than 25,000 ft. Freestream Mach number and vertical hinge offset do not have a significant impact on the resulting exit mass flow rate behavior.

4.1.3.1. *Minimum Geometric Flow Area.* An understanding of the minimum geometric flow area is helpful in understanding the discharge coefficient behavior. The minimum geometric area is defined as the minimum exit flow area between the area of the door and the flow area created by the door opening. Minimum geometric flow area has a direct impact on the discharge coefficient behavior as discussed below. Figure 4.8 compares the minimum geometric flow area for variations in geometrical configuration. Figure 4.8a compares the minimum geometric flow area for door aspect ratios ranging from 0.75 to 1.5. The longer

chord length associated with the  $AR = 1.5$  geometry results in greater lateral flow area and consequently a greater total flow area. At  $15^\circ$ , the geometric flow area for the  $AR = 1.5$  geometry is 1.3 times greater than the  $AR = 0.75$  geometry. The minimum geometric flow area is limited by the opening of the door area at a door angle of  $30^\circ$  for the Gooseneck-hinge type and  $45^\circ$  for the Mid-hinge type. Figure 4.8b compares the minimum geometric flow area for the vertical hinge offset and non-offset cases. Despite the difference in vertical hinge location, the minimum geometric flow area remains the same for both offset and non-offset geometries.

(a) Aspect Ratio

(b) Vertical hinge offset

FIGURE 4.8. Area comparison for Gooseneck-hinge and Mid-hinge types, minimum geometric flow area is limited by door opening area.

4.1.3.2. *Discharge Coefficient.* The discharge coefficient provides the PRD designer with a metric that indicates how well a given opening discharges flow in a non-dimensional manner. The discharge coefficient takes into account the real-gas effects for flow exiting an opening. A discharge coefficient of 1 indicates that no losses exist in the opening while a discharge coefficient of 0 indicates that no flow is exiting the opening. The discharge coefficient calculation is a function of plenum pressure, freestream temperature, and minimum

(a) Freestream altitude

(b) Freestream Mach

(c) Plenum pressure

(d) Plenum temperature

(e) Door aspect ratio

(f) Vertical hinge offset

FIGURE 4.9. Discharge coefficient comparison for Gooseneck-hinge and Mid-hinge types.

geometric flow area. Specific details regarding the discharge coefficient calculation can be found in (2.30).

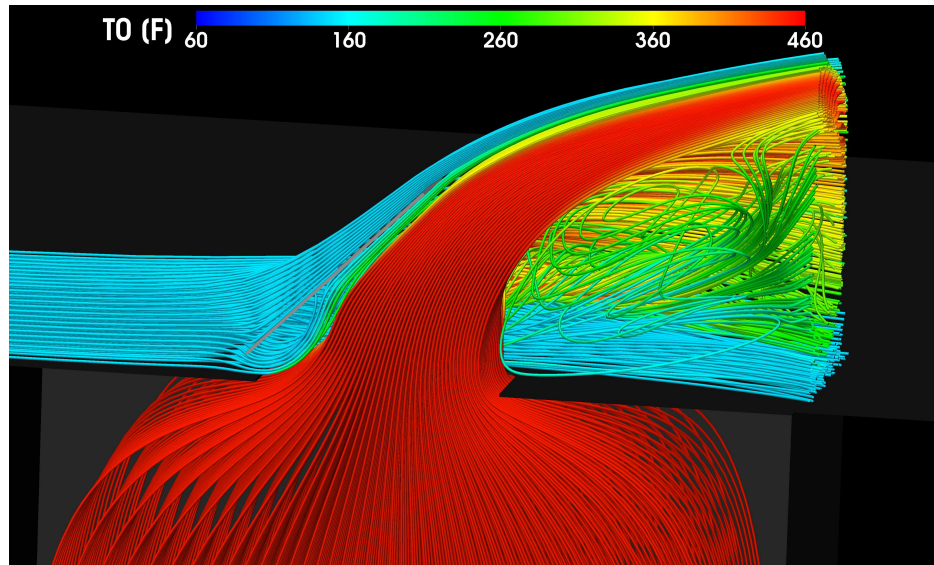
Figure 4.9 compares the discharge coefficients for varying freestream altitude, freestream Mach number, plenum pressure, door aspect ratio, and vertical hinge offset conditions. The Gooseneck-hinge type exhibits a near constant discharge coefficient for door angles between 15–30° before increasing from 30–45° and remaining near constant for 45–60°. The increase in discharge coefficient between 30–45° is explained by the minimum geometric flow area being limited to the area of the door. The Mid-hinge type exhibits a decreasing discharge coefficient for door angles between 15–30° before increasing for increasing door angles. The increase in discharge coefficient from 45–60° is partially explained by the minimum geometric flow area being limited by the door area, similar to the Gooseneck-hinge type. The discharge coefficient for the Gooseneck-hinge type ranges from a minimum of 0.57 at 15° to a maximum of 0.82 at 60°. For the Mid-hinge type, a minimum of 0.5 at 30° and a maximum of 0.75 at 60°. The discharge coefficient for the Mid-hinge type is greater for door angles less than 25°, while above 25°, the discharge coefficient for the Gooseneck-hinge type is greater.

Figure 4.9a compares the discharge coefficient behavior for varying freestream altitudes. The symbol color corresponds to variations in freestream altitude. The red symbols correspond to sea level altitude, the blue symbols correspond to an altitude of 25,000 ft., and the green symbols correspond to an altitude of 45,000 ft. Additional altitude cases were simulated but were not included in the figure to improve reader clarity. The figure illustrates that an increase in freestream altitude results in an increase in discharge coefficient. The discharge coefficient for the Gooseneck-hinge type at 60° increases from 0.72 at sea level altitude to 0.82 at an altitude of 45,000 ft. Door angle has a pronounced effect on the discharge coefficient as illustrated by the Gooseneck-hinge type which increases from 0.57 at the 15° door angle to 0.72 at 60°. An altitude of 45,000 ft. and door angle of 60° corresponds to

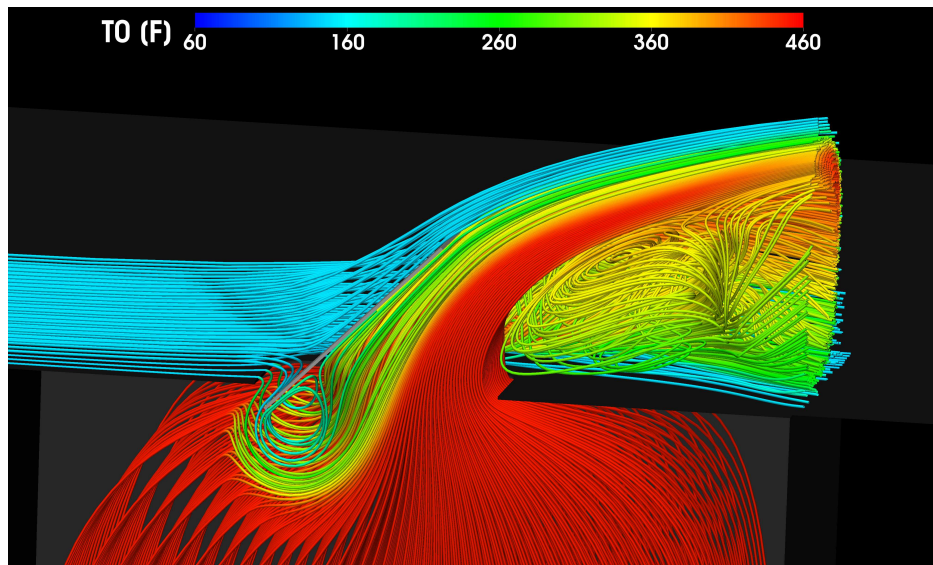
the maximum discharge coefficient of 0.82 and 0.75 for the Gooseneck-hinge and Mid-hinge types, respectively. As mentioned previously, at an altitude of 25,000 ft., a complex shock structure develops on the perimeter of the door thereby choking the exit mass flow rate. Recall that increasing freestream altitude corresponded to decreasing exit mass flow rate, however; the opposite trend is observed for the discharge coefficient. Despite the reduced exit mass flow rate magnitude, the reduced freestream density, temperature, and pressure at increasing freestream altitudes result in a larger calculated discharge coefficient. Increasing altitude corresponds to an increased discharge coefficient for both hinge types.

Figure 4.9b compares the discharge coefficient behavior for varying freestream Mach numbers. The symbol color corresponds to variations in freestream Mach number. The red symbols correspond to a freestream Mach number of 0.1, the blue symbols correspond to a Mach number of 0.5, and the green symbols correspond to a Mach number of 0.9. Additional Mach number cases were simulated but were not included in the figure to improve reader clarity. The figure shows that the discharge coefficient behaviors vary depending on door angle. Typically, the freestream Mach number of 0.5 corresponds to the greatest discharge coefficient for both hinge types. For the Gooseneck-hinge type at  $60^\circ$ , a freestream Mach number of 0.9 corresponds to the highest discharge coefficient near 0.75. For the Mid-hinge type at a door angle of  $15^\circ$ , the  $Ma_\infty = 0.9$  case corresponds to the greatest discharge coefficient, however, with increasing door angle a freestream Mach number of 0.9 corresponds to the lowest discharge coefficient. The varying discharge coefficient behavior at a freestream Mach number of 0.9 is attributed to the variation in leading edge flow behavior. Figure 4.10 compares total temperature streamlines at a freestream Mach number of 0.9 at the  $45^\circ$  door angle. Figure 4.10a illustrates that for the Gooseneck-hinge type, flow enters the leading

edge and exits the trailing edge without significant losses. Figure 4.10a illustrates that for the Mid-hinge type, flow enters the leading edge flows around the door and into the plenum domain before exiting out of the trailing edge. The losses associated the Mid-hinge case help to explain the variation in discharge coefficient behavior at a freestream Mach number of 0.9.



(a) Gooseneck-hinge



(b) Mid-hinge

FIGURE 4.10. Comparison of streamlines colored by total temperature for freestream  $Ma_\infty = 0.9$  and  $45^\circ$  door angle observed from the symmetry plane for Gooseneck-hinge and Mid-hinge types. Note the variation in leading edge flow behavior.

Figure 4.9c compares the discharge coefficient behavior for varying plenum pressures. The symbol color corresponds to variations in plenum pressure. The red symbols correspond to a plenum pressure of 1 psig, the blue symbols correspond to a plenum pressure of 5 psig, and the green symbols correspond to a plenum pressure of 12 psig. Additional plenum pressure

cases were simulated but were not included in the figure to improve reader clarity. The figure illustrates that discharge coefficient increases with increasing plenum pressure. However for the Gooseneck-hinge type and door angles greater than  $45^\circ$ , the 1 psig plenum pressure corresponds to the greatest discharge coefficient. The result is in part to the increased reversed flow leading edge mass flow rate. As freestream flow enters the leading edge of the door, it is accelerated and exhausted out of the trailing edge surface. The impact of the negative leading edge mass flow rate corresponds to greater discharge coefficient values. The discharge coefficient increases with increasing plenum pressure for the Mid-hinge type ranging from 0.59 at  $15^\circ$  to 0.69 at  $60^\circ$ . Plenum pressure has an impact on the discharge coefficient behavior with increasing plenum pressure typically corresponding to an increase in discharge coefficient.

Figure 4.9d compares the discharge coefficient behavior for varying plenum temperatures. The symbol color corresponds to variations in plenum temperature. The red symbols correspond to a plenum temperature of  $-80^\circ\text{F}$ , the blue symbols correspond to a plenum temperature of  $450^\circ\text{F}$ , and the green symbols correspond to a plenum temperature of  $1200^\circ\text{F}$ . Additional plenum temperature cases were simulated but were not included in the figure to improve reader clarity. The figure illustrates that increasing plenum temperature does not have a significant impact on the discharge coefficient behavior. The discharge coefficient varied from 0.57 at  $15^\circ$  for the Gooseneck-hinge type to 0.72 at  $60^\circ$ . The discharge coefficient calculation is a function of plenum temperature which explains the collapse of the discharge coefficient values for all temperatures despite the variation in exit mass flow rates.

Figure 4.9e compares the discharge coefficient behavior for varying door aspect ratios. The symbol color corresponds to variations in door aspect ratio. The red symbols correspond

to a door aspect ratio of 0.75, the blue symbols correspond to a door aspect ratio of 1, and the green symbols correspond to a door aspect ratio of 1.5. Additional door aspect ratio cases were simulated but were not included in the figure to improve reader clarity. The figure shows that increasing door aspect ratio corresponds to non-linear discharge coefficient behavior. For the Gooseneck-hinge type at door angles less than  $23^\circ$ , an aspect ratio of 0.75 exhibits a greater discharge coefficient compared with a door aspect ratio of 1.5. However, for door angles greater than  $23^\circ$  the  $AR = 1.5$  corresponds to the greatest discharge coefficient. A similar behavior is observed with the Mid-hinge type, but the equilibrium point is near  $38^\circ$ . The decrease in discharge coefficient between  $15\text{--}30^\circ$  for the  $AR = 0.75$  case can be explained by the reduced strength of the trailing edge vortices.

Figure 4.9f compares the discharge coefficient behavior for varying vertical hinge offsets. The symbol color corresponds to variations in vertical hinge offset. The red symbols correspond to no vertical hinge offset and the blue symbols correspond to a vertical hinge offset of 0.7 in. The figure shows that vertical hinge offset corresponds to a slight increase in discharge coefficient for all door angles for both types. The increased exit mass flow rate of the vertically hinge offset geometry results in an increase in discharge coefficient from 0.71 for the non-offset case to 0.73 for the offset case. Hinge offset results in a subtle increase in the discharge coefficient.

Discharge coefficient provides a useful metric for the PRD designer to evaluate discharge performance in a non-dimensional manner. The Gooseneck-hinge type consistently had a greater exit mass flow rate for door angles greater than  $23^\circ$ . Variations in freestream altitude, freestream Mach number, plenum pressure, and door aspect ratio were have an impact on the discharge coefficient.

4.1.3.3. *Effective Flow Area.* The effective area is an important parameter in evaluating PRD performance as it takes into account the non-linearities and losses associated for flow exiting an opening. Figure 4.11 compares non-dimensional effective flow areas for varying freestream altitude, freestream Mach number, plenum pressure, door aspect ratio, and vertical hinge offset conditions. The effective flow area increases with increasing door angle before approaching a limit, the value of the limit is dependent on hinge type. The Gooseneck-hinge type approaches a maximum near  $60^\circ$ , while the Mid-hinge type approaches a maximum that is outside of the door angles examined. The larger geometric flow area associated with the Gooseneck-hinge type corresponds to a greater effective flow area. Despite the differences in discharge coefficient, both hinge types exhibit a similar response to variations in parameters.

(a) Freestream altitude

(b) Freestream Mach

(c) Plenum pressure

(d) Plenum temperature

(e) Door aspect ratio

(f) Vertical hinge offset

FIGURE 4.11. Effective area comparison for Gooseneck-hinge and Mid-hinge types.

Figure 4.11a compares the non-dimensional effective area behavior for varying freestream altitudes. The figure illustrates that an increase in freestream altitude results in an increase in effective flow area for both hinge types. For the Gooseneck-hinge type, the effective flow

area is consistently 12–15% greater for an altitude of 45,000 ft. compared to the sea level altitude. The effective flow area for the Gooseneck-hinge type exhibits a rapid increase from 15-45° before approaching a limit at 60°. The Mid-hinge type exhibits a consistent, non-linear, increase from 15-60°. At a door angle of 15°, the Gooseneck-hinge type effective flow area is 1.5 times greater than the Mid-hinge hinge compared with 1.1 times greater at 60°. Freestream altitude is shown to correspond to an increase in the non-dimensional effective flow area.

Figure 4.11b compares the non-dimensional effective area behavior for varying freestream Mach numbers. The symbol color corresponds to variations in freestream Mach number. The figure shows that a freestream Mach number of 0.5 corresponds to the greatest effective flow area across all door angles except the 60° Gooseneck-hinge type case where a freestream Mach number of 0.9 results in the greatest effective area. For the Gooseneck-hinge type, the effective area is maximized for the  $Ma_\infty = 0.5$  followed by the  $Ma_\infty = 0.9$  and  $Ma_\infty = 0.1$  cases. At a door angle of 60°, the  $Ma_\infty = 0.9$  case results in the greatest effective flow area due to the acceleration of the reversed flow at the leading edge. Effective area for the Mid-hinge type is maximized at a freestream Mach number of 0.5 followed by a freestream Mach of 0.1 and 0.9. The variation in behavior for the  $Ma_\infty = 0.9$  case is largely in part to losses associated with the reverse flow freestream flow as detailed previously. Mach number has an impact on the effective flow area, particularly at door angles greater than 30° where the maximum effective flow area occurs at a freestream Mach number of 0.5.

Figure 4.11c compares the non-dimensional effective area behavior for varying plenum pressures. The symbol color corresponds to variations in plenum pressure. The figure illustrates that increases in plenum pressure correspond to increases in effective flow area for

both hinge types. The increased effective area observed for the Gooseneck-hinge type at a plenum pressure of 1 psig is due to the dramatic rise in discharge coefficient at door angles greater than  $45^\circ$ .

Figure 4.11d compares the non-dimensional effective area behavior for varying plenum temperatures. The symbol color corresponds to variations in plenum temperature. The figure illustrates that increasing plenum temperature results in negligible variation in the effective flow area.

Figure 4.11e compares the non-dimensional effective area behavior for varying door aspect ratios. The figure shows that increasing door aspect ratio corresponds to an increase in effective flow area as expected. The significant increase in lateral edge flow area associated with the  $AR = 1.5$  case corresponds to greater exit mass flow rates. For the Gooseneck-hinge type, the effective flow area approaches a limit near  $60^\circ$  regardless of door aspect ratio. Increasing door aspect ratio results in an increase effective flow area.

Figure 4.11f compares the non-dimensional effective area behavior for varying vertical hinge offsets. The symbol color corresponds to variations in vertical hinge offset. The figure shows that vertical hinge offset corresponds to a marginal increase in effective flow area. The 2% increase in discharge coefficient corresponds to a 2% increase in effective flow area.

Effective flow area is an important metric in evaluating PRD performance as it takes into account the discharge coefficient and geometric flow area. The effective flow area is shown to be the most sensitive to freestream altitude, plenum pressure, and door aspect ratio. The PRD designer can use the data obtained to optimize the PRD design. If discharge characteristics are the primary concern, doors of aspect ratio 1.5 provide an increased effective flow area thereby permitting more flow to exit the plenum.

4.1.3.4. *Mass Flow Rate Distribution.* The distribution of mass flow rate through the leading, lateral, and trailing edge surfaces provides the PRD designer with valuable insight into developing novel PRD designs. The ability to measure the relative distribution of the exit mass flow rate has never been done before. Understanding the distribution of flow helps to explain the behavior of flow characteristics and to gain a deeper understanding of the impact that operating conditions and geometric configurations have. The relative mass flow rate was obtained by normalizing the exit mass flow rate from the leading, lateral, and trailing surface by the total exit mass flow rate. Figure 4.12 compares the leading edge mass flow rate distribution for varying freestream altitude, freestream Mach number, plenum pressure, door aspect ratio, and vertical hinge offset conditions. Geometric differences between the Gooseneck-hinge and Mid-hinge types result in different leading edge mass flow distributions. Flow exiting the leading edge of the Mid-hinge type, tends to be entrained and remain attached to the top surface of the door before entering the freestream, this is reflected by the positive values for leading edge mass flow rate for nearly all parameters examined. Leading edge mass flow tends to increase from 8% at  $15^\circ$  to 11% at  $60^\circ$  for most Mid-hinge cases. Negative leading edge flow is observed for the  $Ma_\infty = 0.9$  and  $P = 1$  psig cases. Flow exiting the Gooseneck-hinge geometries tends to remain slightly positive until an equilibrium angle is reached where flow enters the plenum from the freestream. The exact equilibrium angle is compared in Figure 4.13 and is highly dependent flow conditions.

Figure 4.12a compares the relative leading edge mass flow rate distribution behavior for varying freestream altitudes. The figure illustrates that an increase in freestream altitude results in a greater percentage of flow exiting the leading edge. At a door angle of  $60^\circ$ , the most significant variation in leading edge flow behavior exists. For the Mid-hinge geometry

(a) Freestream altitude

(b) Freestream Mach

(c) Plenum pressure

(d) Plenum temperature

(e) Door aspect ratio

(f) Vertical hinge offset

FIGURE 4.12. Leading edge mass flow rate comparison for Gooseneck-hinge and Mid-hinge types.

at  $60^\circ$ , the relative mass flow rate through the leading edge accounts for 11% of the total exit mass flow rate at sea level altitude compared to 13% of the total flow at an altitude of 45,000 ft. The Gooseneck-hinge type exhibits negative leading edge mass flow rates at  $60^\circ$

ranging from -11% at sea level to -0.2% at an altitude of 45,000 ft. The reduced momentum of the freestream flow at higher altitudes corresponds to greater leading edge mass flow rates.

Figure 4.12b compares the relative leading edge mass flow rate distribution behavior for varying freestream Mach numbers. The figure shows that increasing freestream Mach number corresponds to decreasing leading edge mass flow rate. The figure illustrates that at the  $Ma_\infty = 0.9$  condition the leading edge mass flow rate is negative for all door angles for the Gooseneck-hinge type. The Mid-hinge type has a negative leading edge mass flow rate near  $25^\circ$ . Figure 4.12c compares the relative leading edge mass flow rate distribution behavior for varying plenum pressures. The figure illustrates that increasing plenum pressure corresponds to an increase in leading edge mass flow rate. The leading edge mass flow rate is negative for all door angles for the Gooseneck-hinge type. Negative leading edge flow occurs near  $20^\circ$  for the Mid-hinge type.

Figure 4.12d compares the relative leading edge mass flow rate distribution behavior for varying plenum temperatures. The symbol color corresponds to variations in plenum temperature. The figure illustrates that increasing plenum temperature has minimal impact on the Mid-hinge type leading edge mass flow rate. For the Gooseneck-hinge geometry, a variation in the leading edge mass flow rate distribution occurs at the  $60^\circ$  door angle where the  $T = 1200^\circ\text{F}$  case permits 14% of the total exit mass flow rate to enter the leading edge.

Figure 4.12e compares the relative leading edge mass flow rate distribution behavior for varying door aspect ratios. The symbol color corresponds to variations in door aspect ratio. The figure shows that increasing door aspect ratio corresponds to decreasing leading edge mass flow rate distribution. The wider door width of the  $AR = 0.75$  case permits more mass flow to exit the leading edge compared to the trailing edge.

Figure 4.12f compares the relative leading edge mass flow rate distribution behavior for varying vertical hinge offsets. The figure indicates that vertical hinge offset corresponds to a decrease in the leading edge mass flow rate distribution for the Mid-hinge type, but an increase in leading edge mass flow rate for the Gooseneck-hinge type.

The equilibrium reverse mass flow rate angle is the angle that flow enters the plenum from the freestream which provides a useful metric in examining the relative mass flow distribution and helps to comprehend the high-temperature wall surface temperature characteristics. As mentioned previously, in nearly all of the operating and geometric configurations for the Gooseneck-hinge type, reversed leading edge mass flow rate is observed. In certain cases, particularly low pressure and high Mach number, reversed leading edge flow is observed for the Mid-hinge type. Figure 4.13 compares the reverse leading edge mass flow rate equilibrium angle.

Figure 4.13a compares the leading edge reverse mass flow rate equilibrium angles for freestream pressure altitudes ranging from -2,000 ft. to 45,000 ft. The leading edge reverse mass flow angle is shown to have a slight positive relationship with altitude ranging from  $33^\circ$  at -2,000 ft. to  $60^\circ$  at 45,000 ft. The lower freestream density at an altitude of 45,000 ft. results in reduced freestream momentum which delays the leading edge reverse mass flow rate equilibrium angle.

Figure 4.13b compares the leading edge reverse mass flow rate equilibrium angles for freestream Mach numbers ranging from 0 to 0.9. Increasing Mach number results in a non-linear decrease in reverse mass flow equilibrium angle ranging from  $78^\circ$  at  $Ma_\infty = 0$  to  $4^\circ$  at  $Ma_\infty = 0.9$  for the Gooseneck-hinge type. The Mid-hinge type exhibits a negative leading edge mass flow rate for Mach numbers greater than 0.75.

(a) Freestream altitude

(b) Freestream Mach

(c) Plenum pressure

(d) Plenum temperature

(e) Door aspect ratio

(f) Vertical hinge offset

FIGURE 4.13. Leading edge reverse massflow distribution comparison for Gooseneck-hinge and Mid-hinge types.

Figure 4.13c compares the leading edge reverse mass flow rate equilibrium angles for plenum pressures ranging from 1 psig to 12 psig. An increase in plenum pressure corresponds to a non-linear increase in the leading edge equilibrium angle as it approaches a maximum

near  $40^\circ$ . The equilibrium angle for a plenum pressure of 1 psig is near  $20^\circ$  for the Mid-hinge type and negative for the Gooseneck-hinge type. A negative equilibrium angle indicates that regardless of door angle, the leading edge mass flow rate is negative.

Figure 4.13d compares the leading edge reverse mass flow rate equilibrium angles for plenum temperatures ranging from  $-80^\circ\text{F}$  to  $1500^\circ\text{F}$ . The figure illustrates a slight negative relationship with increasing temperature. At the  $-80^\circ\text{F}$  plenum temperature the leading edge equilibrium angle is near  $38^\circ$  while at a plenum temperature of  $1500^\circ\text{F}$  the equilibrium angle is near  $34^\circ$ .

Figure 4.13e compares the leading edge reverse mass flow rate equilibrium angles for door aspect ratios ranging from 0.75 to 1.5. The figure illustrates that with increasing door aspect ratio a linear decrease in the leading edge equilibrium angle occurs. For the door aspect ratio of 0.75, the equilibrium angle is near  $37^\circ$  compared to an equilibrium angle near  $31^\circ$  for a door aspect ratio of 1.5. The increased door width associated with the  $\text{AR} = 0.75$  configuration creates more of a blockage at the leading edge of the door delays the reverse leading edge flow compared with the  $\text{AR} = 1.5$  configuration.

Figure 4.13f compares the leading edge reverse mass flow rate equilibrium angles for vertical hinge offset ranging from non-offset to 0.75-inch offset. The increased blockage created at the leading edge by the vertically hinge offset configuration delays the reverse flow equilibrium angle for the Gooseneck-hinge type from  $35^\circ$  for the non-offset configuration to  $40^\circ$  for the offset configuration.

Figure 4.12 compares the lateral edge mass flow rate distribution for varying freestream altitude, freestream Mach number, plenum pressure, door aspect ratio, and vertical hinge offset conditions. The relative flow exiting the Gooseneck-hinge type is typically 10% greater

than the Mid-hinge type for all cases. The decreased lateral edge flow area coupled with the geometric difference of the leading edge of the door extending into the plenum domain results in decreased lateral edge mass flow percentages. With increasing door angle, the relative mass flow rate shifts from the lateral edge to the trailing edge surface due to a reduction in the strength of the lateral edge vortices and an increase in the low-pressure region created aft of the door opening with increasing door angle.

Figure 4.14a compares the relative lateral edge mass flow rate distribution behavior for varying freestream altitudes. The figure illustrates that an increase in freestream altitude has a minor impact on the relative lateral edge flow. At lower door angles the lateral edge flow for increasing altitudes remains near 50% for the Gooseneck-hinge type and 41% for the Mid-hinge type. As the door angle increases, a decrease in the relative lateral edge mass flow which is near 28% for the Gooseneck-hinge type and 20% for the Mid-hinge type. The increase in door angle results in a 20% decrease in the relative flow and an apparent shift towards the trailing edge opening.

Figure 4.14b compares the relative lateral edge mass flow rate distribution behavior for varying freestream Mach numbers. The symbol color corresponds to variations in freestream Mach number. The figure shows that the behavior of the relative flow exiting the lateral surfaces with increasing freestream Mach number is dependent on hinge location. For both hinge types, the  $Ma_\infty = 0.1$  condition corresponds to the greatest lateral edge flow for angles less than  $35^\circ$ . At door angles greater than  $35^\circ$ , the  $Ma_\infty = 0.5$  condition corresponds to the greatest relative lateral edge mass flow for the Gooseneck-hinge type while the  $Ma_\infty = 0.9$  case corresponds to the greatest relative lateral edge mass flow for the Mid-hinge type.

(a) Freestream altitude

(b) Freestream Mach

(c) Plenum pressure

(d) Plenum temperature

(e) Door aspect ratio

(f) Vertical hinge offset

FIGURE 4.14. Lateral edge mass flow distribution comparison for Gooseneck-hinge and Mid-hinge types.

Figure 4.14c compares the relative lateral edge mass flow rate distribution behavior for varying plenum pressures. The figure illustrates that no strong relationship exists between an increase in plenum pressure and the relative flow exiting the lateral surface. No consistent

trends are observed for the Gooseneck-hinge type, however, for the Mid-hinge type the  $P = 5$  psig corresponds to the greatest relative lateral edge flow at door angles less than  $30^\circ$  but for door angles greater than  $30$ -deg, the  $P = 1$  psig condition corresponds to the greatest lateral edge flow.

Figure 4.14d compares the relative lateral edge mass flow rate distribution behavior for varying plenum temperatures. The figure illustrates that increasing plenum temperature results in a negligible difference in the relative lateral edge mass flow rate.

Figure 4.14e compares the relative lateral edge mass flow rate distribution behavior for varying door aspect ratio. The figure shows that increasing door aspect ratio corresponds to an increase in the lateral edge mass flow rate. High aspect ratio doors tend to promote greater lateral edge mass flow due to the increased lateral edge flow area. For the Gooseneck-hinge type at a door angle of  $15^\circ$ , nearly 63% of the total exit mass flow exits through the lateral edge surface for the  $AR = 1.5$  geometry compared with 42% for the  $AR = 0.75$  case. At a door angle of  $60^\circ$ , the lateral edge flow appears to approach a constant lateral edge flow near  $27^\circ$  for the Gooseneck-hinge type due to the near constant exit mass flow rates for all door aspect ratios.

Figure 4.14f compares the relative lateral edge mass flow rate distribution behavior for varying vertical hinge offsets. The figure shows that vertical hinge offset has an impact on the Gooseneck-hinge type, resulting in less flow exiting the lateral edges at door angles greater than  $30^\circ$ . Vertical hinge offset does not make an impact for the Mid-hinge type on the relative lateral mass flow.

Figure 4.15 compares the trailing edge mass flow rate distribution for varying freestream altitude, freestream Mach number, plenum pressure, door aspect ratio, and vertical hinge

offset conditions. the trailing edge mass flow increases with increasing door angle. A sharp increase in trailing edge mass flow rate for door angles greater than  $30^\circ$  occurs due to the recombination of the lateral edge vortices with the trailing edge vortices. The increased strength of the trailing edge vortices at higher door angles creates the sharp increase in trailing edge flow. For door angles less than  $30^\circ$  the Mid-hinge type tends to have a greater trailing edge mass flow distribution while at higher door angles the Gooseneck-hinge type has a greater percentage of trailing edge mass flow.

Figure 4.15a compares the relative trailing edge mass flow rate distribution behavior for varying freestream altitudes. The figure illustrates that an increase in freestream altitude results in a decrease in trailing edge mass flow rate. Variations in altitude have an impact on the trailing edge flow behavior for door angles greater than  $30^\circ$ . For the Gooseneck-hinge type at a door angle of  $30^\circ$  and sea level altitude, the trailing edge flow accounts for 50% of the total exit mass flow compared with 82% at a door angle of  $60^\circ$ . The Mid-hinge type corresponds to greater percentage of exit mass flow for door angles less than  $35^\circ$  while at greater door angles, the Gooseneck-hinge type promotes a greater percentage of trailing edge mass flow. The behavior is partially attributed to the increase in negative leading edge flow.

Figure 4.15b compares the relative trailing edge mass flow rate distribution behavior for varying freestream Mach numbers. The symbol color corresponds to variations in freestream Mach number. The figure shows that increasing Mach number corresponds to a greater percentage of flow exiting the trailing edge. The behavior at  $Ma_\infty = 0.9$  is due to the negative leading edge mass flow rates. As mentioned previously, flow at  $Ma_\infty = 0.9$  enters the leading edge and is discharged through the trailing edge.

(a) Freestream altitude

(b) Freestream Mach

(c) Plenum pressure

(d) Plenum temperature

(e) Door aspect ratio

(f) Vertical hinge offset

FIGURE 4.15. Trailing edge relative mass flow distribution comparison for Gooseneck-hinge and Mid-hinge types.

Figure 4.15c compares the relative trailing edge mass flow rate distribution behavior for varying plenum pressures. The symbol color corresponds to variations in plenum pressure. The figure illustrates that increasing plenum pressure decreases the percentage of flow exiting

the trailing edge. The decreased strength of the lateral edge vortices and the reversed leading edge flow associated with the  $P = 1$  psig plenum condition result in a near linear behavior in the relative trailing edge mass flow percentage.

Figure 4.15d compares the relative trailing edge mass flow rate distribution behavior for varying plenum temperatures. The symbol color corresponds to variations in plenum temperature. The figure illustrates that increasing plenum temperature results in a slight increase in the trailing edge mass flow percentage at door angles greater than  $30^\circ$ . For the Gooseneck-hinge type at  $60^\circ$ , the relative flow exiting the trailing edge surface is near 84% for the  $T = -80^\circ\text{F}$  plenum temperature compared with 81% for the  $T = 1200^\circ\text{F}$  plenum temperature. For door angles less than  $30^\circ$ , plenum temperature does not have an impact on the relative flow exiting the trailing edge.

Figure 4.15e compares the relative trailing edge mass flow rate distribution behavior for varying door aspect ratios. The symbol color corresponds to variations in door aspect ratio. The figure shows that increasing door aspect ratio corresponds to decreasing trailing edge mass flow percentage. The longer chord length associated with the  $AR = 1.5$  configuration permits more mass flow out of the trailing edges, particularly at lower door angles. However, as the door angle increase the trailing edge flow approaches a constant value near 85% for the Gooseneck-hinge type and 70% for the Mid-hinge type.

Figure 4.15f compares the relative trailing edge mass flow rate distribution behavior for varying vertical hinge offsets. The symbol color corresponds to variations in vertical hinge offset. The red symbols correspond to no vertical hinge offset and the blue symbols correspond to a vertical hinge offset of 0.75 inches. The figure shows that vertical hinge offset corresponds to a 3-5% increase in the relative flow exiting the trailing edge surface.

Figure 4.16 compares the lateral to trailing equilibrium angle for varying freestream altitude, freestream Mach number, plenum pressure, door aspect ratio, and vertical hinge offset conditions. The lateral to trailing equilibrium angle is defined as the door angle where the mass flow exiting the lateral surface is equal to the mass flow exiting the trailing surface. The figure shows that the equilibrium angle is consistently  $10^\circ$  greater for the Gooseneck-hinge type compared with the Mid-hinge type. A detailed comparison is provided below.

(a) Freestream altitude

(b) Freestream Mach

(c) Plenum pressure

(d) Plenum temperature

(e) Door aspect ratio

(f) Vertical hinge offset

FIGURE 4.16. Lateral to trailing equilibrium comparison for Gooseneck-hinge and Mid-hinge types.

Figure 4.16a compares the lateral to trailing mass flow rate equilibrium angles for freestream pressure altitudes ranging from -2,000 ft. to 45,000 ft. The figure illustrates that a negative relationship is observed for increasing altitude for the Mid-hinge type, ranging from  $11^\circ$  at

an altitude of -2,000 ft. to  $0^\circ$  at an altitude of 45,000 ft. The gooseneck geometry does not exhibit the same relationship instead remains at  $22^\circ$  regardless of altitude.

Figure 4.16b compares the lateral to trailing mass flow rate equilibrium angles for freestream Mach numbers ranging from 0 to 0.9. The figure shows that an increase in freestream Mach number exhibit corresponds to a negative relationship with the lateral to trailing mass flow distribution equilibrium. For the Mid-hinge type, the equilibrium angle at  $Ma_\infty = 0$  is near  $10^\circ$  while at  $Ma_\infty = 0.9$  the equilibrium angle is near  $5^\circ$ . The impact of the increased freestream momentum functions to redirect more of the flow towards the trailing edge.

Figure 4.16c compares the lateral to trailing mass flow rate equilibrium angles for plenum pressures ranging from 1 psig to 12 psig. The figure shows that increasing plenum pressure corresponds to an increase in the lateral to trailing equilibrium angle. For the Gooseneck-hinge type, at  $P = 1$  psig, the equilibrium angle is near  $10^\circ$  while at a plenum pressure of 12 psig, the equilibrium angle is near  $24^\circ$ . The Mid-hinge type exhibits similar behavior ranging from  $0^\circ$  at 1 psig to  $5^\circ$  at 12 psig.

Figure 4.16d compares the lateral to trailing mass flow rate equilibrium angles for plenum temperatures ranging from  $-80^\circ\text{F}$  to  $1500^\circ\text{F}$ . The figure shows that plenum temperature has a negligible impact on the lateral to trailing equilibrium angle. The Gooseneck-hinge type achieves an equilibrium near  $22^\circ$  while the Mid-hinge type achieves an equilibrium near  $9^\circ$ .

Figure 4.16e compares the lateral to trailing mass flow rate equilibrium angles for door aspect ratios ranging from 0.75 to 1.5. The figure shows that an increase in aspect ratio corresponds to an increase in the lateral to trailing equilibrium angle. For the Gooseneck-hinge type at  $AR = 0.75$ , the equilibrium angle is near  $8^\circ$  while at an  $AR = 1.5$ , the equilibrium angle is near  $35^\circ$ . The Mid-hinge type reflects a similar behavior ranging from

10° at AR = 1 to 30° at AR = 1.5. The larger lateral flow area associated with higher aspect ratio doors permits more mass flow to exit through the lateral areas compared with the trailing edge surface.

Figure 4.16f compares the lateral to trailing mass flow rate equilibrium angles for vertical hinge offset ranging from no offset to an offset of 0.75 inches. The figure shows that hinge offset does not exhibit a significant relationship with the lateral to trailing equilibrium angle.

4.1.4. THRUST. Depending on flow conditions, a thrust force is created by the PRD opening. While thrust is not a primary concern of the core compartment PRD, an understanding of the impact of flow behaviors on a thrust characteristics is important. Similar geometries to the PRD are observed for alternate applications in the aerospace industry. The thrust force was defined as a positive stream-wise component of force acting on the door. A negative thrust coefficient indicates the door is creating drag on the aircraft. Figure 4.17 compares thrust coefficients for the varying freestream altitude, freestream Mach number, plenum pressure, door aspect ratio, and vertical hinge offset conditions. An increase in door angle corresponds to a decrease in thrust coefficient. The Mid-hinge type consistently has a greater thrust coefficient due to the reduced door area exposed to the freestream flow as shown previously.

Figure 4.17a compares the thrust coefficient behavior for varying freestream altitudes. The figure illustrates that an increase in freestream altitude results in an increase in thrust coefficient. At the 15° door angle and Gooseneck-hinge type, the thrust coefficient is 7 times greater at an altitude of 45,000 ft. compared to sea level altitude. The non-dimensionalization procedure inflates the thrust coefficient calculation for the high altitude case due to the reduced freestream density and pressure.

(a) Freestream altitude

(b) Freestream Mach

(c) Plenum pressure

(d) Plenum temperature

(e) Door aspect ratio

(f) Vertical hinge offset

FIGURE 4.17. Thrust coefficient comparison for Gooseneck-hinge and Mid-hinge types.

Figure 4.17b compares the thrust coefficient behavior for varying freestream Mach numbers. The figure shows that an increase in Mach number corresponds to a decrease in thrust coefficient. Note that the increased Mach number reduces the equilibrium thrust coefficient

angle from  $40^\circ$  at  $Ma_\infty = 0.5$  to  $22^\circ$  at  $Ma_\infty = 0.9$ . The increased freestream momentum associated with the high Mach number cases creates a substantial streamwise force on the door and thus limits the thrust characteristics.

Figure 4.17c compares the thrust coefficient behavior for varying plenum pressures. The figure illustrates that increasing plenum pressure corresponds to an increase in thrust coefficient. The 12 psig plenum pressure at  $15^\circ$  for the Mid-hinge type has a thrust coefficient near 1.8 compared with the 1 psig plenum pressure that has a thrust coefficient near 0.04.

Figure 4.17d compares the thrust coefficient behavior for varying plenum temperatures. The symbol color corresponds to variations in plenum temperature. The figure illustrates that increasing plenum temperature results in a negligible impact on the resulting thrust characteristics.

Figure 4.17e compares the thrust coefficient behavior for door angles ranging from  $15^\circ$  to  $60^\circ$  for the Gooseneck-hinge and Mid-hinge types at varying door aspect ratios. The figure shows that increasing door aspect ratio corresponds to a decreased thrust coefficient. The shorter chord length associated with the  $AR = 0.75$  geometric configuration redirects the flow exiting the plenum in a shorter distance compared to the  $AR = 1.5$  configuration.

Figure 4.17f compares the thrust coefficient behavior for varying vertical hinge offsets. The figure shows that vertical hinge offset corresponds to a decrease on the order of 2-3% in the thrust coefficient.

Thrust characteristics are shown to be the most sensitive to variation in freestream altitude, plenum pressure, and door aspect ratio. While thrust characteristics are not paramount to the analysis of a core-compartment PRD, it is important to understand the direct impact on the aircraft flight performance of PRD's on the nacelle casing.

4.1.5. SURFACE TEMPERATURE. Bleed duct failures can result in plenum temperatures in the range of 450–1500°F exiting onto the surface of the engine shroud during a burst duct event. The surface temperature characteristics on the engine shroud are important to the PRD designer as it dictates whether high-temperature materials or thermal insulating blankets are necessary. The regions of high-temperature and average wall temperature are two important quantities in understanding the surface temperature characteristics. An overview of the wall surface temperature behavior at varying door angles for the baseline case is provided and a detailed discussion of the non-dimensional high-temperature area is discussed below. Figure 4.18 compares the total temperature contours on the wall surface for the Gooseneck-hinge type for door angles ranging from 15° to 60°. Figure 4.18a shows that high-temperature regions exist downstream of the lateral edges of the door. At a door angle of 30°, high-temperature flow remains in contact with the bottom wall surface as shown in Figure 4.18b. For larger door angles, the high-temperature contact area is reduced as shown in Figures 4.18c–4.18d.

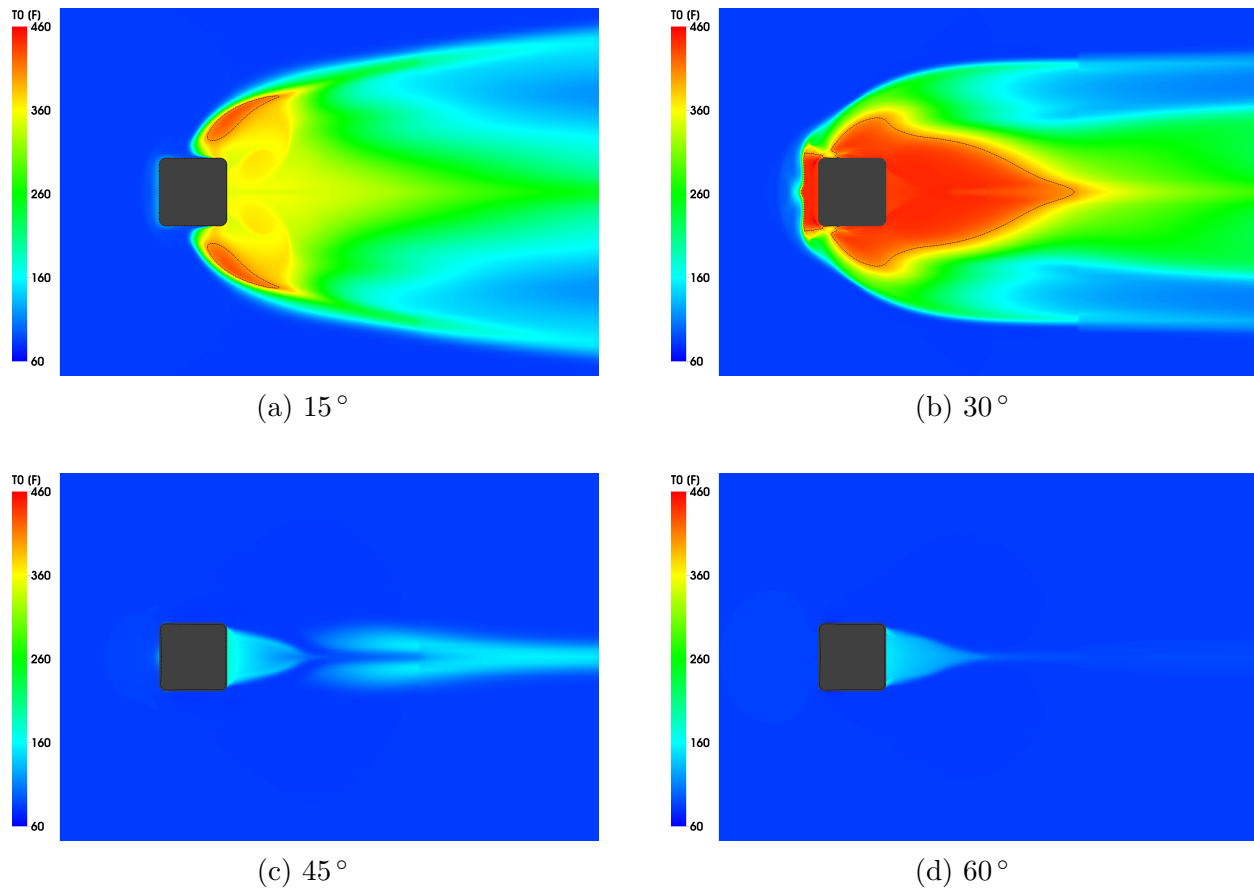


FIGURE 4.18. Comparison of total temperature contours on bottom wall surface for Gooseneck-hinge type baseline case. Note the black contour line corresponds to temperatures greater than 400°F.

Overall, the Gooseneck-hinge type tends to have a greater high-temperature area due to the increased lateral flow area. Differences in the leading edge flow behavior also contribute to differences in the wall surface temperature characteristics at door angles less than 30°. Figure 4.19 provides a contour of total temperature symmetry which illustrates that flow exiting the Mid-hinge type tends to remain entrained and attached to the top surface of the door while flow exiting the Gooseneck-hinge type will exit through the leading edge and remain attached to the bottom wall before encountering the freestream flow.

4.1.5.1. *Non-dimensional High-Temperature Area.* Figure 4.20 compares the high-temperature area and non-dimensional average wall temperature for varying freestream altitude, freestream

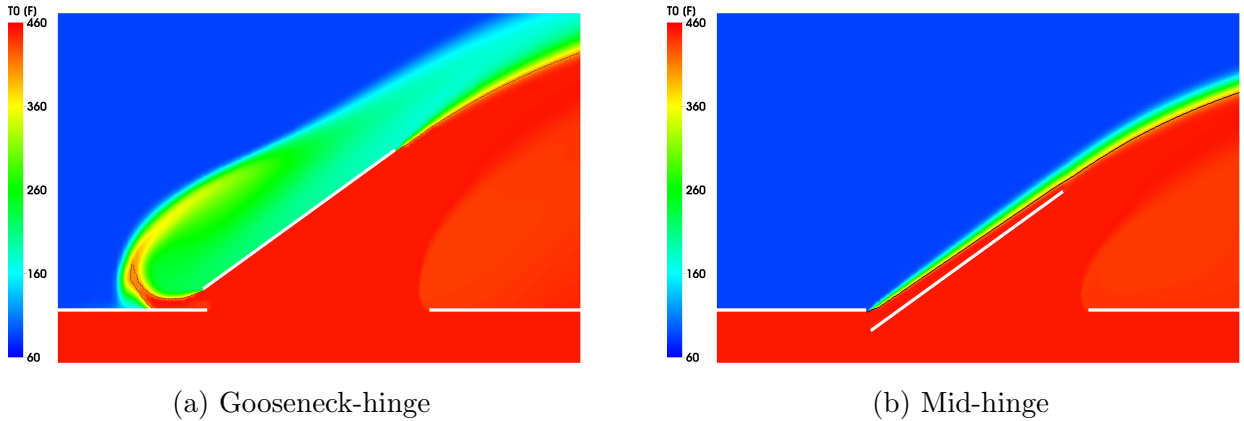


FIGURE 4.19. Comparison of total temperature contours on symmetry plane at  $30^\circ$  for Gooseneck-hinge and Mid-hinge type baseline case.

Mach number, plenum pressure, door aspect ratio, and vertical hinge offset conditions. Both figures indicate that door angle has a pronounced effect on the wall surface temperature characteristics, the exact behavior is dependent on the operating conditions and geometric configuration.

Figure 4.20a compares the non-dimensional high-temperature area behavior for varying freestream altitudes. The figure illustrates that the maximum high-temperature contact area occurs at an altitude of 25,000 ft. at  $30^\circ$ . A 6 fold reduction in the high-temperature area is shown between the  $30$  and  $45^\circ$  door angles for a freestream altitude of 25,000 ft. As mentioned previously, the primary mechanism behind the reduction in wall temperature is the increased strength of the trailing edge vortices that lift the flow off of the bottom wall surface. The figure also shows that the wall surface temperature characteristics at 45,000 ft. exhibit a decreasing high-temperature area for increasing door angles due to the complex shock structure that exists at the leading, lateral, and trailing edge openings as discussed previously. Figure 4.21 provides total temperature streamlines (left) and contours (right) at altitudes of 0, 25,000, and 45,000 ft. The figure shows that an increase in freestream altitude reduces the strength of the lateral edge vortices. The high-velocity jet created at the lateral

(a) Freestream altitude

(b) Freestream Mach

(c) Plenum pressure

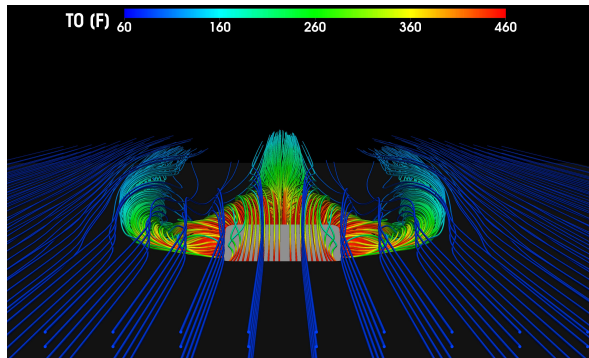
(d) Plenum temperature

(e) Door aspect ratio

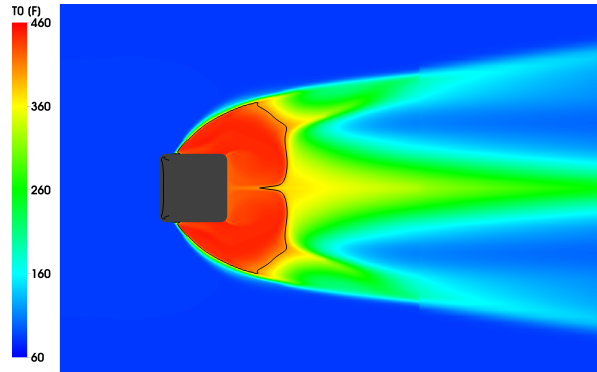
(f) Vertical hinge offset

FIGURE 4.20. Non-dimensional high surface temperature area comparison for Gooseneck-hinge and Mid-hinge types. edge extends laterally from the door opening. The reduced high-temperature area observed for a freestream altitude of 45,000 ft. is due to the increased strength of the lateral edge jet and the reduced impact that the freestream flow has on constraining the lateral edge flow.

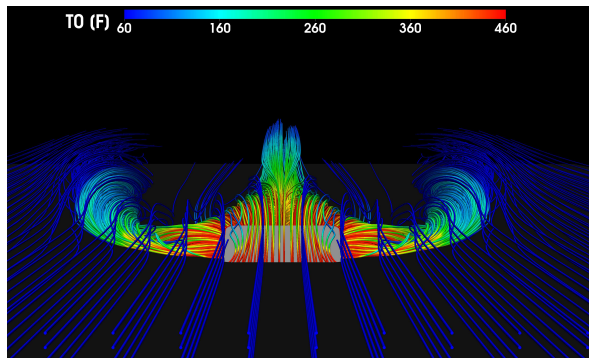
This is illustrated in Figures 4.21e and 4.21f where the increased contact region is shown to extend farther laterally for the 45,000 foot condition than for the sea level condition.



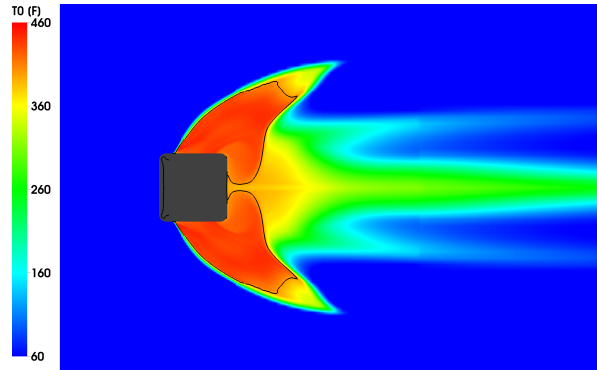
(a) Altitude = 0 ft.



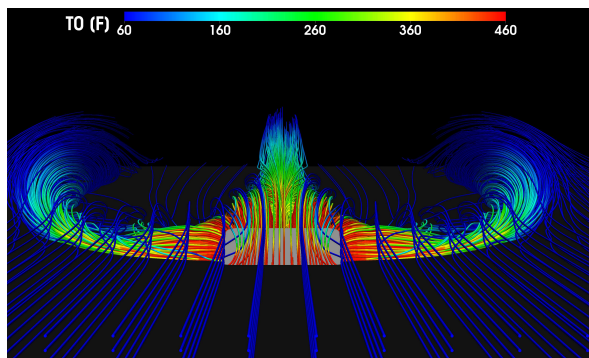
(b) Altitude = 0 ft.



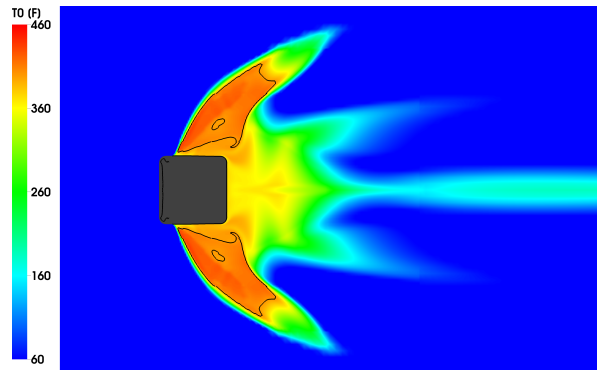
(c) Altitude = 25,000 ft.



(d) Altitude = 25,000 ft.



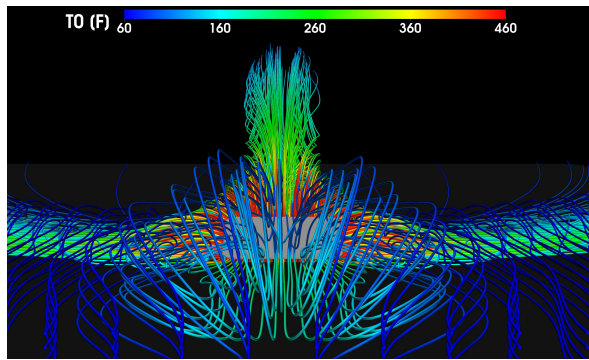
(e) Altitude = 45,000 ft.



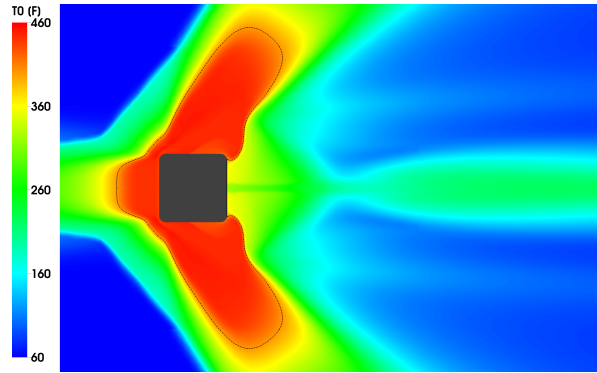
(f) Altitude = 45,000 ft.

FIGURE 4.21. Comparison of streamlines colored by total temperature (left) and total temperature contours (right) for Mid-hinge type at  $15^\circ$  for variation in freestream altitude.

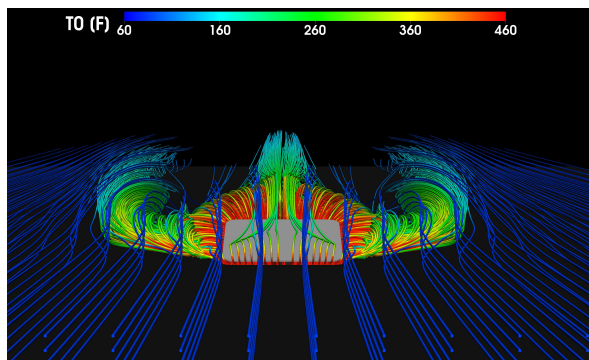
Figure 4.20b compares the non-dimensional high-temperature area behavior for varying freestream Mach numbers. The figure shows that the high-temperature contact area behaves in a non-linear manner that is unexpected. For the Gooseneck-hinge type, the greatest high-temperature area occurs at the 15-deg door angle for freestream Mach numbers of 0.1 and 0.9 yet the greatest high-temperature area for a freestream Mach number of 0.5 occurs at the 30° door angle. For the freestream  $Ma_\infty = 0.1$  and  $Ma_\infty = 0.9$  conditions, increasing door angle corresponds to a reduction in high-temperature area by 6.7 times between 15° and 60°. Figure 4.22 compares the variation in freestream Mach number with total temperature streamlines (left) and contours (right) at 15° for the Gooseneck-hinge type. Figure 4.22a illustrates that at  $Ma_\infty = 0.1$  flow exiting the leading, lateral, and trailing edge surfaces is unconstrained. The unconstrained flow results in increased wall surface temperatures as shown in Figure 4.22b where the primary regions of high-temperature are at the leading and lateral edges. At  $Ma_\infty = 0.9$ , the flow exiting the plenum is highly constrained as illustrated by the redirection of the lateral edge vortices downstream and the reduced height of the trailing edge vortices as shown in Figure 4.22e. The corresponding wall surface contour in Figure 4.22f shows that the increased freestream Mach number forces flow to remain in contact with the bottom wall further downstream of the door. The impact of freestream Mach number on the resulting wall surface temperatures results in a non-linear behavior. Varying flow dynamics at  $Ma_\infty = 0.1$  and  $Ma_\infty = 0.9$  contribute to an increased wall surface temperature at 15° before decaying with increasing door angle.



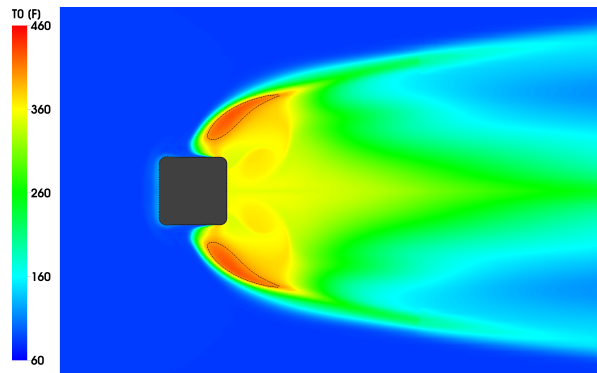
(a) Mach = 0.1



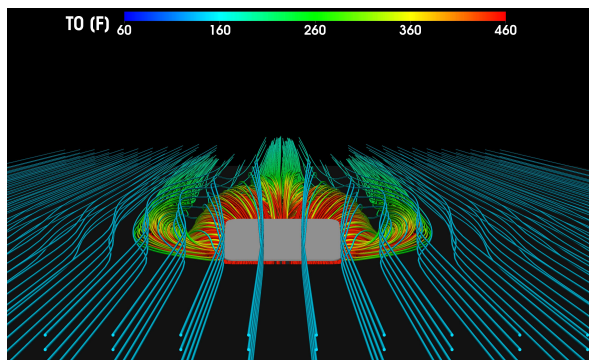
(b) Mach = 0.1



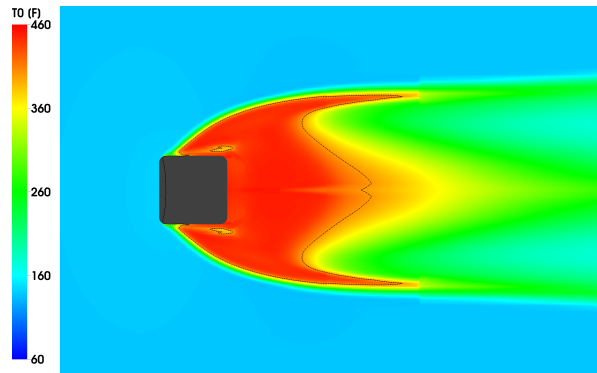
(c) Mach = 0.5



(d) Mach = 0.5



(e) Mach = 0.9



(f) Mach = 0.9

FIGURE 4.22. Comparison of streamlines colored by total temperature (left) and total temperature contours (right) for Gooseneck-hinge type at  $15^\circ$  for variation in freestream Mach number.

Figure 4.20c compares the non-dimensional high-temperature area behavior for varying plenum pressures. The figure illustrates that increasing plenum pressure corresponds to an increase in high-temperature area. At a plenum pressure of 12 psig the high-temperature

area is 1.4 times greater than at the baseline 5 psig case. Figure 4.23 compares the total temperature contours on the bottom wall and the symmetry plane for plenum pressures of 1 psig and 5 psig. The figure illustrates that flow associated with the 12 psig case exits the plenum and tends to remain attached to the bottom wall surface as depicted by the leading edge jet.

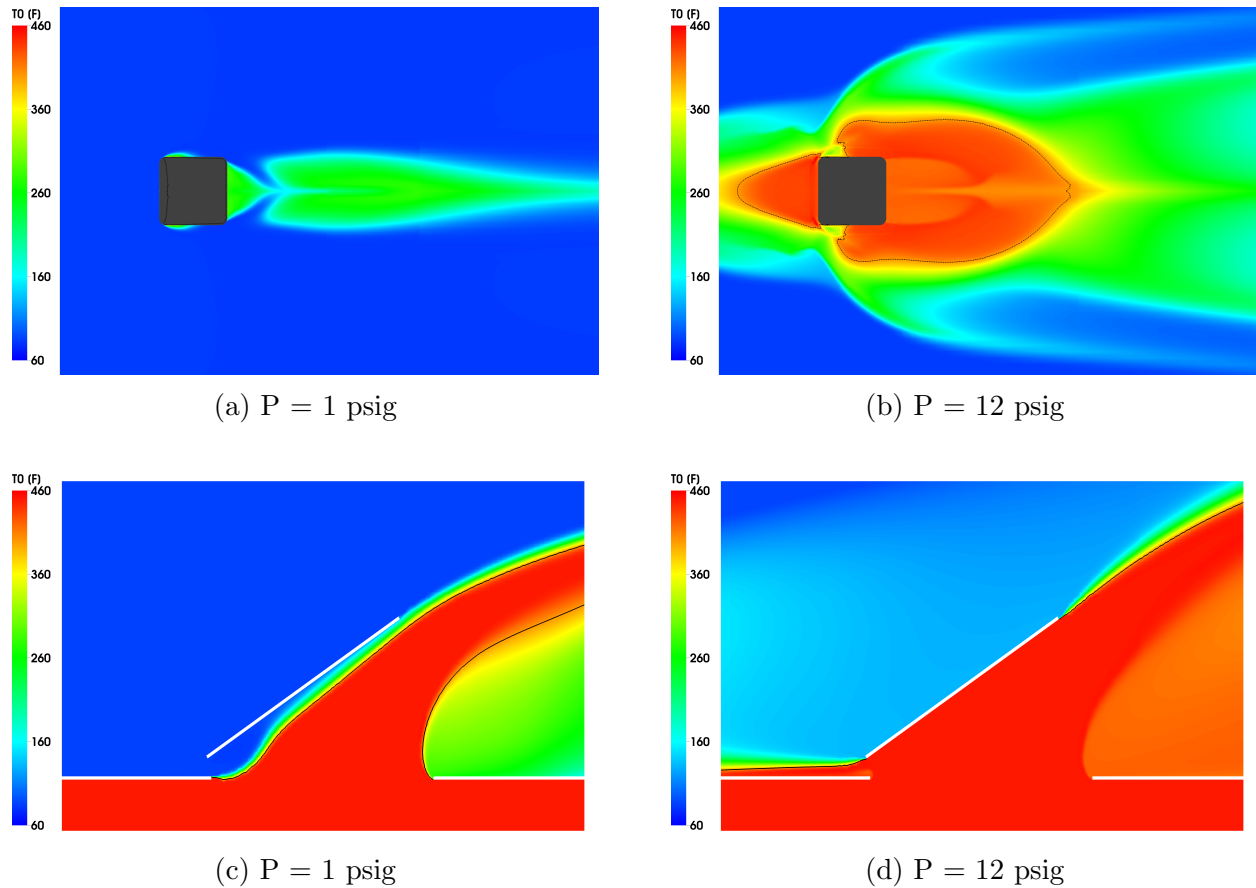


FIGURE 4.23. Comparison of total temperature contours for Gooseneck-hinge type at  $30^\circ$  for variation in plenum pressure; bottom wall view (top) symmetry plane (bottom).

Figure 4.20d compares the non-dimensional high-temperature area behavior for varying plenum temperatures. The figure illustrates that increasing plenum temperature results in increased high-temperature area. Note that the Y-axis extends to 25 instead of 8 for the comparison. A plenum temperature. At a door angle of  $30^\circ$  for the Gooseneck-hinge type, the

1200°F plenum temperature increases the high-temperature area by a factor of 5 compared with the 450°F plenum temperature case. The dramatic increase in high-temperature area illustrates the need for high-temperature resistant materials near the PRD opening and motivated further study of novel geometric PRD configurations as discussed in Section 4.2.

Figure 4.20e compares the non-dimensional high-temperature area behavior for varying door aspect ratios. The figure shows that increasing door aspect ratio corresponds to significant variation in the surface temperature characteristics depending on door angle. At the 15° door angle, the AR = 1.5 configuration results in the greatest high-temperature area due to the longer chord length and increased lateral edge flow. For door angles greater than 30°, the high-temperature area is the greatest for the AR = 0.75 configuration. The figure shows that the Mid-hinge type at 15° the AR = 1.5 configuration results in a high-temperature area that is 1.75 times greater than the AR = 0.75 configuration. The higher aspect ratio door reduces the wall surface temperature due to the longer chord length which creates a low-pressure region that extends higher into the freestream flow which allows the trailing edge vortices to lift off from the bottom wall surface due to the blockage created by the door opening. Figure 4.24 illustrates the relative comparison of the increased high-temperature area at 15° for the AR = 0.75 and AR = 1.5 configurations for the Mid-hinge type.

Figure 4.20f compares the non-dimensional high-temperature area behavior for varying vertical hinge offsets. The figure shows that vertical hinge offset corresponds to an increase in high-temperature area for lower door angles. At 15°, the hinge offset case results in an increase in high-temperature area by a factor of 4.75 for the Gooseneck-hinge type. The increased blockage at the lateral edge permits greater leading and lateral edge flow compared with the non-offset geometry. Figure 4.25 compares the behavior of the wall surface

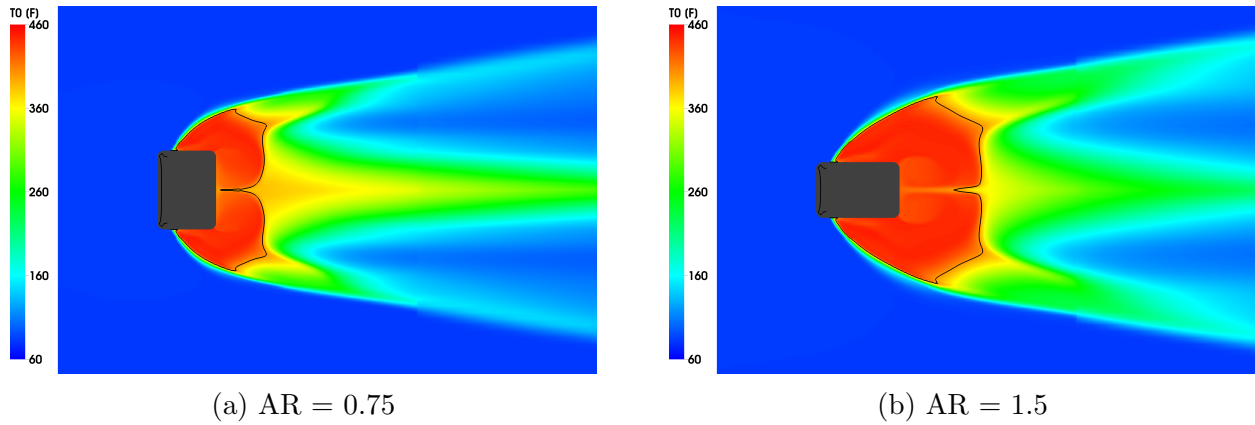
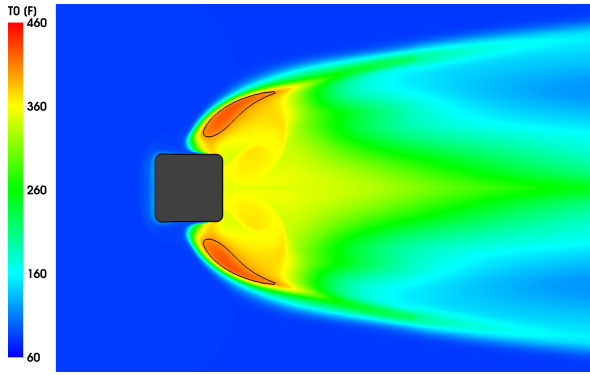
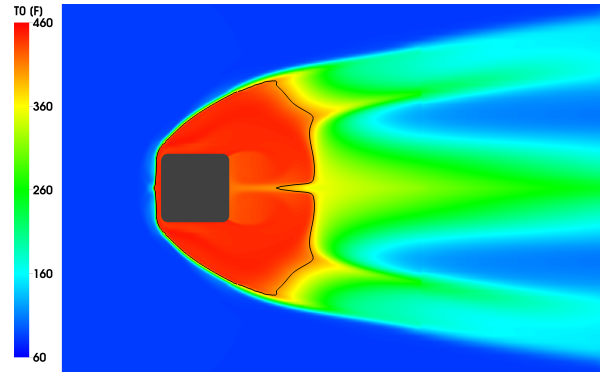


FIGURE 4.24. Comparison of total temperature contours on bottom wall for variation in door aspect ratio at  $15^\circ$  for Mid-hinge type.

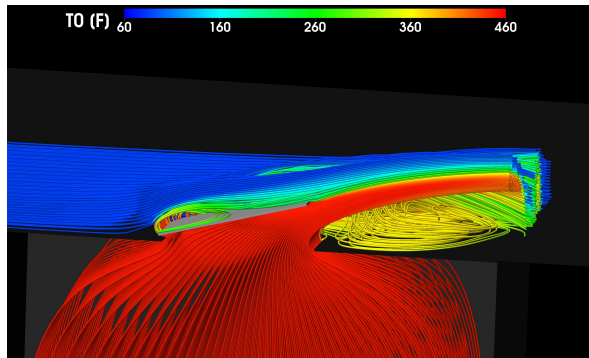
total temperature contours and streamlines colored by total temperature observed from the symmetry plane. The increased high-temperature area is illustrated in Figures 4.25a–4.25b. The impact of the increased leading edge blockage and corresponding high-temperature recirculation is illustrated in Figures 4.25c–4.25d.



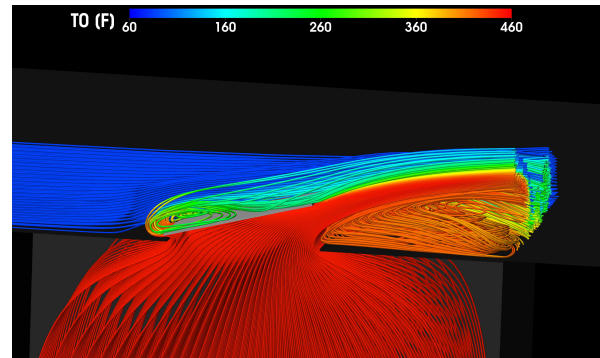
(a) Offset = 0 in.



(b) Offset = 0.75 in.



(c) Offset = 0 in.



(d) Offset = 0.75 in.

FIGURE 4.25. Comparison of total temperature contours and streamlines colored by total temperature for Gooseneck-hinge type at  $15^\circ$  for variation in vertical hinge offset.

The non-dimensional high-temperature area is shown to be sensitive to variations in freestream, plenum, and geometric configurations. Typically, the maximum wall temperature occurs near a door angle of  $30^\circ$  before sharply decreasing due to the elevation of the trailing edge vortices off of the bottom wall surface. The behavior of the exiting gas is strongly governed by the lateral and trailing vortex pairs. The lateral vortices tend to force the fluid to remain attached to the wall while the trailing edge vortices tend to lift the flow from the wall. The presence of the stable vortices is potentially the result of using a steady-state simulation and a symmetry plane. In reality, there is a potential for turbulence to break up the vortex pairs so that the lifting behavior is disrupted which will have an impact on

the downstream wall temperature. The results obtained from the high-temperature area comparison provide useful insight into the impact the operating conditions and geometric configurations have on the resulting wall surface temperature characteristics.

4.1.6. FLOW STRUCTURE. It is necessary for the PRD designer to have a detailed understanding of the complex flow physics associated with a burst duct event. When a PRD opens, complex flow features such as leading and lateral edge vortices, jets, and shockwaves develop. The development of these flow features is dependent on door angle, geometric configuration, and flow parameters. One of the benefits of a computational analysis is the ability to visualize and analyze the complex flow features observed that would otherwise be impossible. A detailed discussion of the flow features for the baseline Gooseneck-hinge and Mid-hinge cases will be presented.

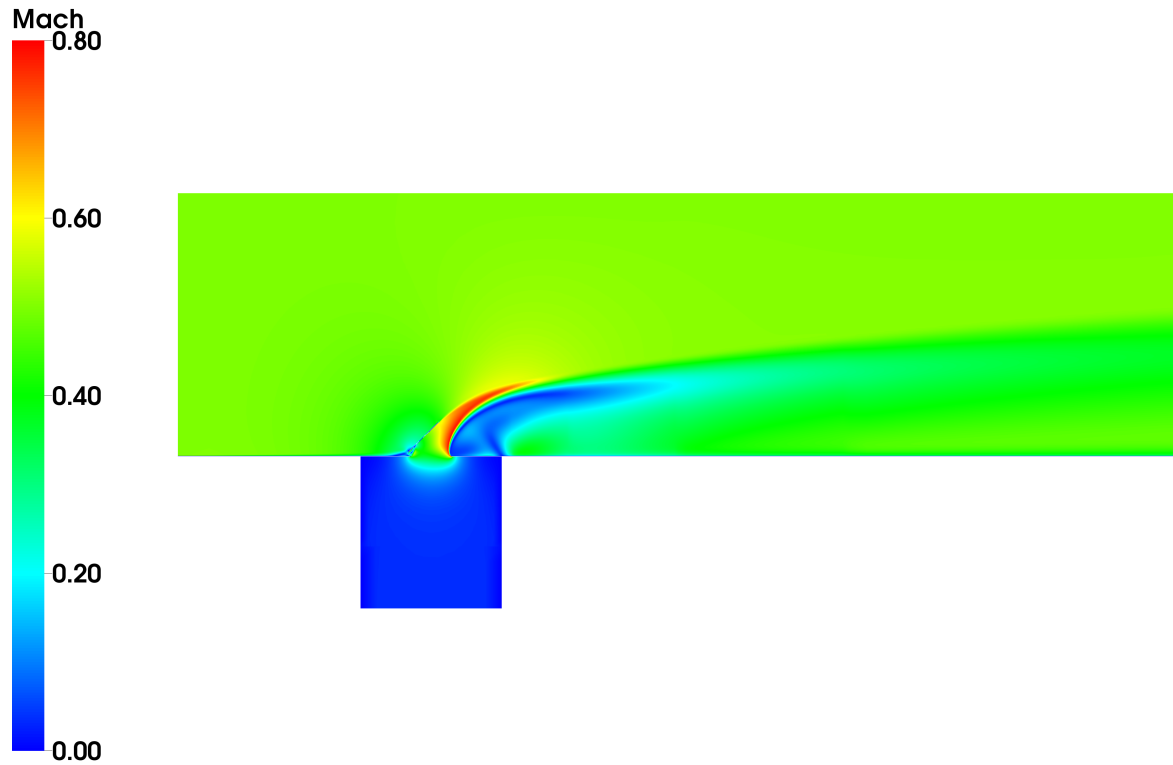


FIGURE 4.26. Contours of Mach number on the symmetry plane view for baseline Gooseneck-hinge  $45^\circ$  case.

Figure 4.26 provides an overall view of the computational domain on the symmetry plane.

It is evident that the PRD opening creates a low Mach number and low-pressure region aft of the door opening. A jet created at the lateral edge opening dissipates as it interacts with the freestream flow. A detailed comparison of contours of Mach number along the symmetry plane for the Gooseneck-hinge type are shown in Figure 4.27.

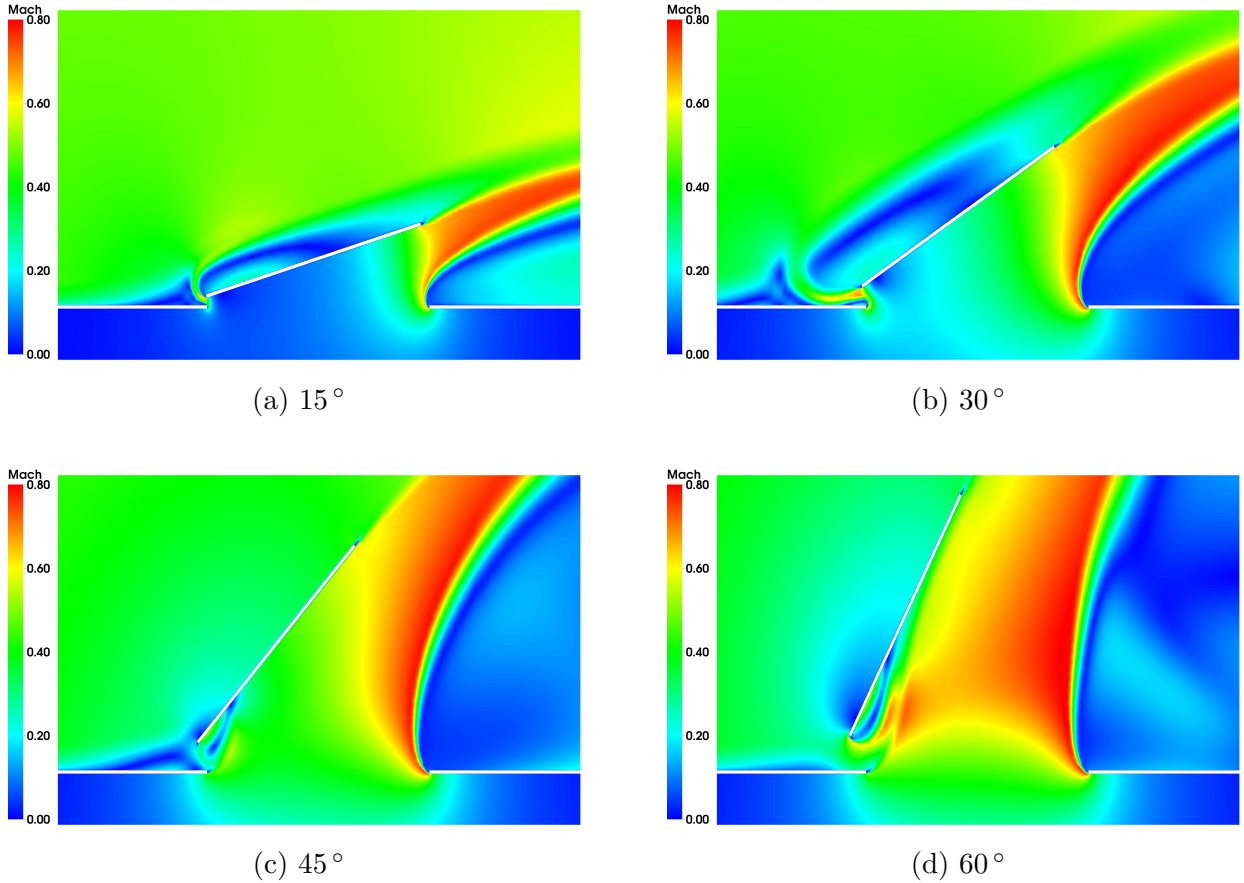


FIGURE 4.27. Contours of Mach number for door angles ranging from 15-60°, baseline case, Gooseneck-hinge type.

Increasing door angle results in a shift in the location of the trailing edge jet. A leading edge jet is observed for door angles less than 30°, which creates a low-velocity region on the top surface of the door that is exposed to the freestream. As the door angle increases, the leading edge flow reverses and flow from the freestream enters the plenum compartment as illustrated in Figure 4.28.

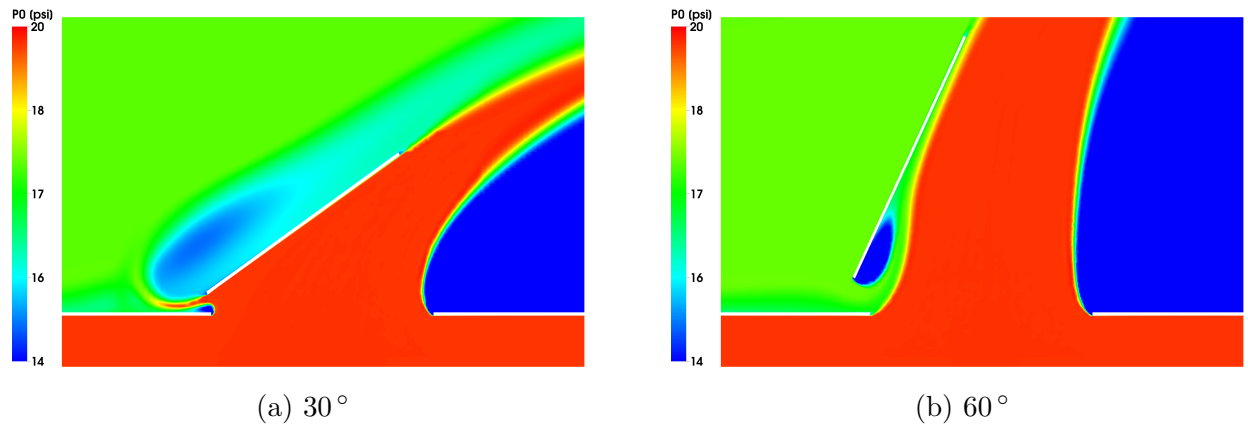


FIGURE 4.28. Contours of total pressure for Gooseneck-hinge type at 30° and 60°.

Figure 4.29 depicts that similar flow behavior exists for the Mid-hinge type. The trailing edge jet behaves in a similar manner but with a decreased flow exit area. The leading jet, however, is significantly different. The leading edge of the Mid-hinge door extends into the plenum domain allowing for the development of a leading jet that is entrained in the plenum domain and extends the length of the door before mixing with the trailing edge exiting jet. The behavior of the leading edge jet is sensitive to door angle, plenum conditions, and freestream conditions.

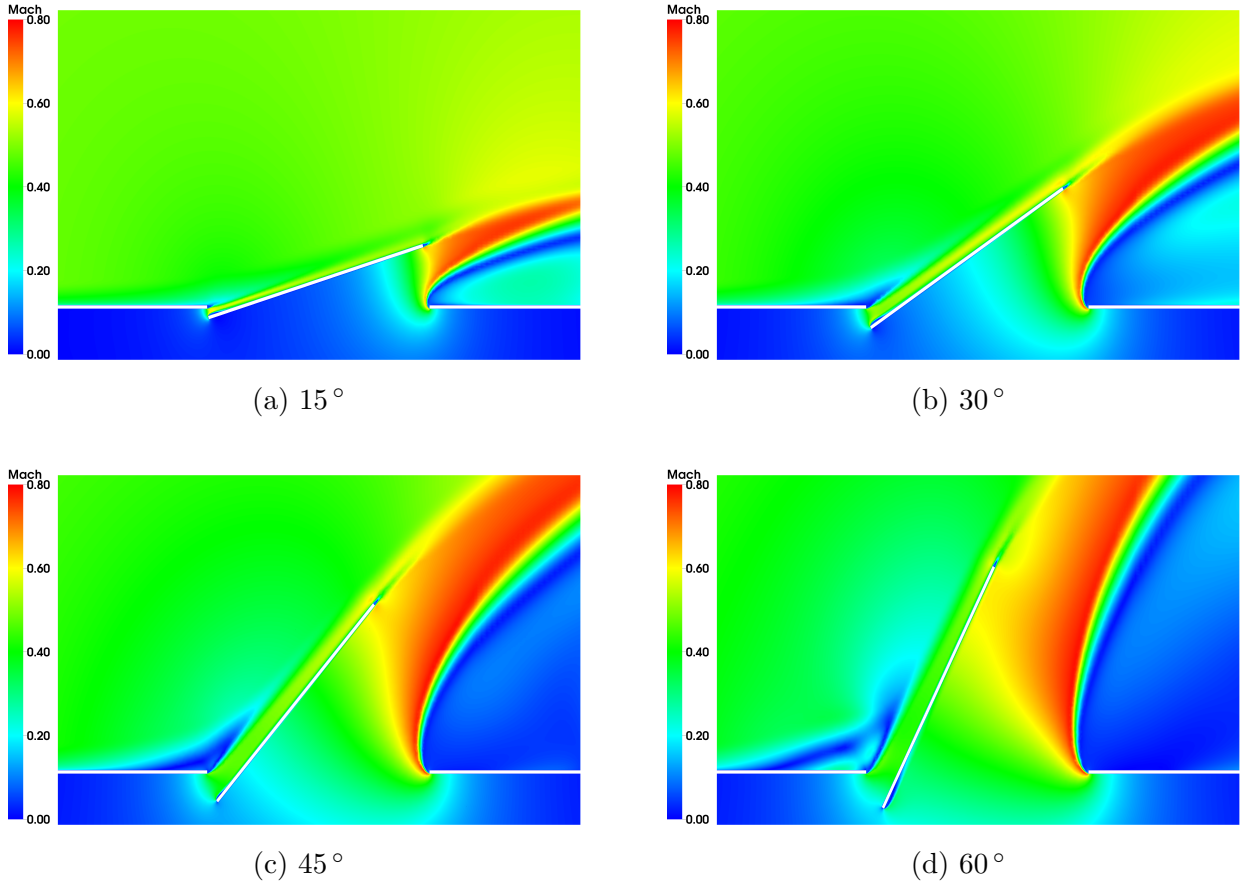
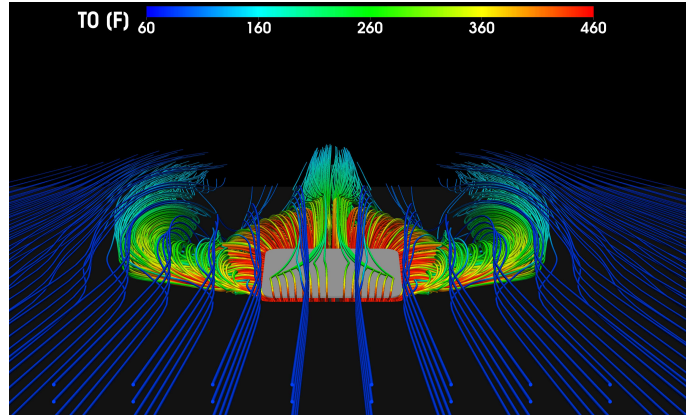
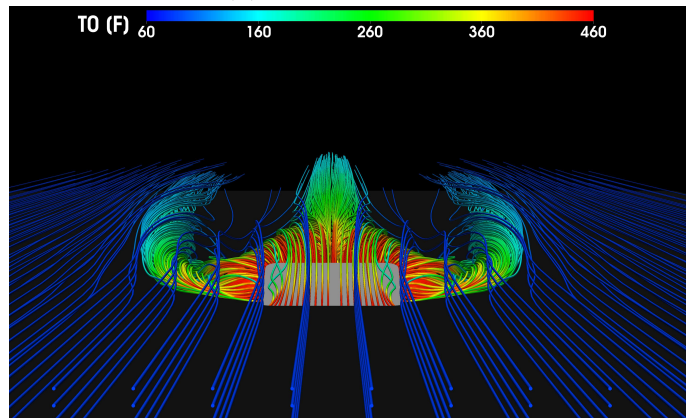


FIGURE 4.29. Contours of Mach number for door angles ranging from 15-60°, baseline case, Mid-hinge type.

A burst duct event is fundamentally three-dimensional in nature. Figure 4.30 depicts the complex flow exiting the plenum where lateral and trailing edge vortices are observed for the Gooseneck-hinge type at a 15° door angle.



(a) Gooseneck-hinge



(b) Mid-hinge

FIGURE 4.30. Streamlines colored by total temperature for baseline Gooseneck-hinge and Mid-hinge geometries at  $15^\circ$ .

Figure 4.31 provides a detailed view from the symmetry plane depicting the trailing edge jet behavior and the stationary recirculations created aft of the door opening for the Gooseneck-hinge type. The leading edge jet and corresponding leading edge vortex are also evident.

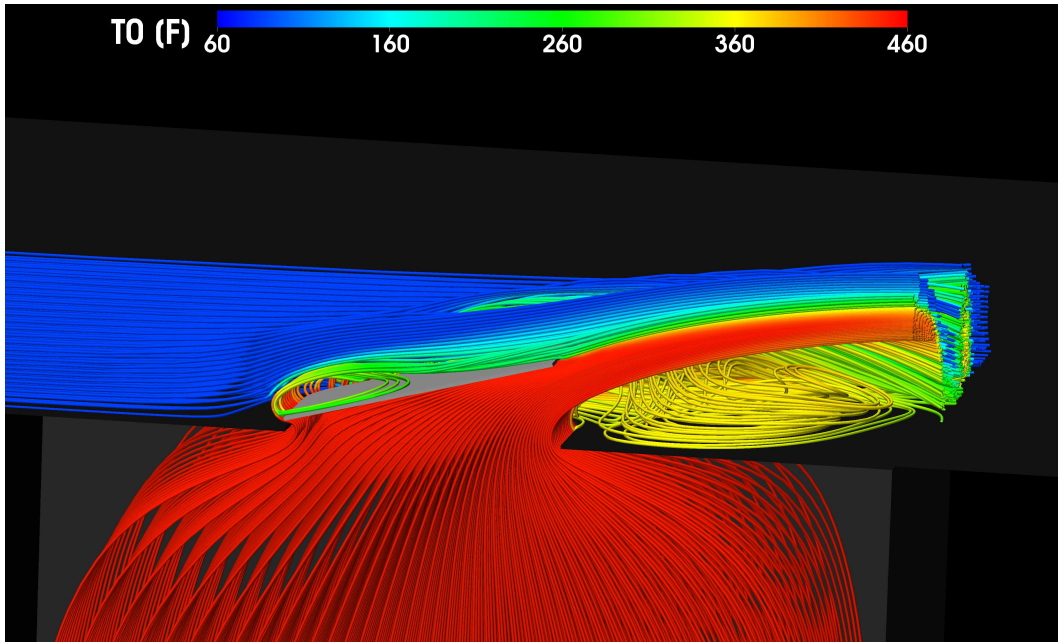
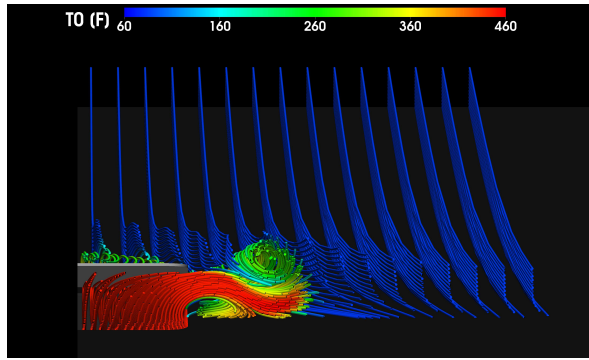
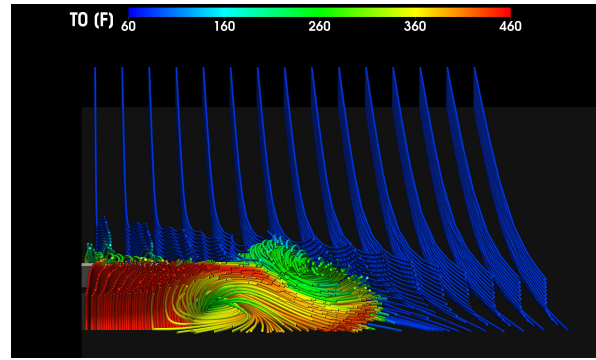


FIGURE 4.31. Streamlines colored by total temperature for baseline Gooseneck-hinge 15° geometry observed from symmetry plane.

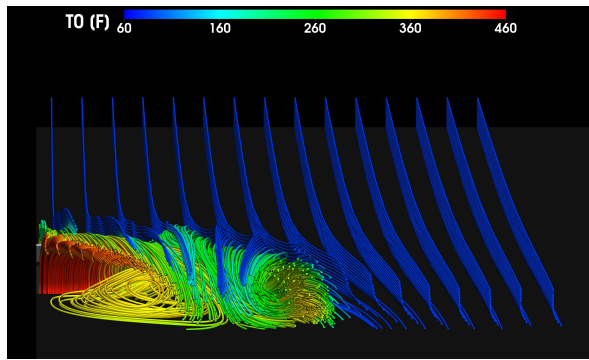
To gain a deeper understanding of the flow exiting the lateral and trailing edges, a series of slices extending normal to the symmetry plane measured from the trailing edge of the door opening are shown in Figure 4.32. This figure illustrates that the lateral edge vortex initiates from the leading edge corner opening. As flow exits the plenum, it is redirected by the bottom surface of the door and is enveloped into the lateral edge vortex. A portion of the flow exiting the leading edge flows towards the low-pressure region created aft of the door opening creating the recirculation observed in Figure 4.32c. A detailed observation 34 inches downstream illustrates the development of the trailing edge vortices.



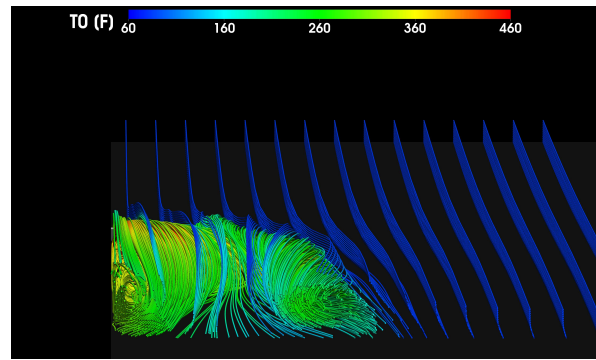
(a) Door Mid Plane



(b) 1 inch Downstream



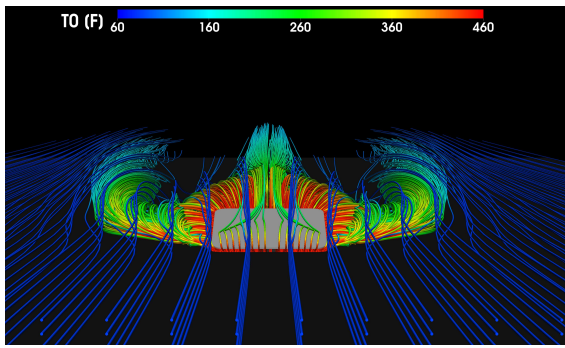
(c) 12.5 inches Downstream



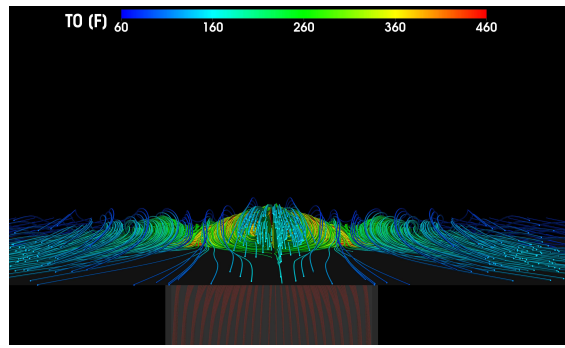
(d) 34 inches Downstream

FIGURE 4.32. Detailed slice view of streamlines colored by total temperature at varying mid-plane slices for 15 deg door angle Gooseneck-hinge type with view looking upstream.

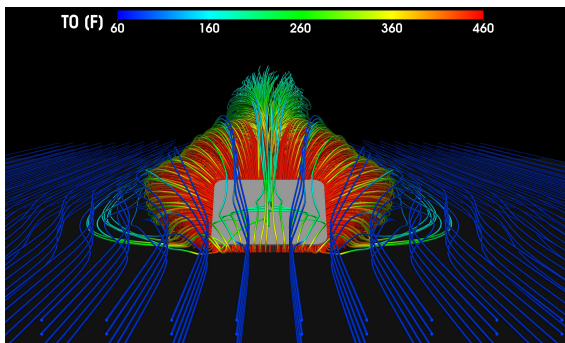
The exit flow behavior has a strong dependence on door angle as illustrated in Figures 4.33–4.34. With increasing door angle, the lateral edge vortices shown at  $15^\circ$  combine with the trailing edge vortices and begin to elevate off of the bottom wall of the freestream domain. At door angles of  $45^\circ$  and greater, the trailing edge vortices are completely lifted off the bottom wall surface which helps to explain the 10 fold decrease in wall surface temperatures between  $30^\circ$  and  $45^\circ$ . Figure 4.34 provides a detailed comparison of the trailing edge flow features from a slice taken just downstream of the door opening.



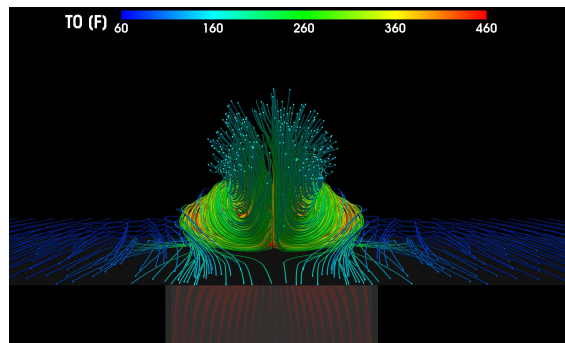
(a) 15°



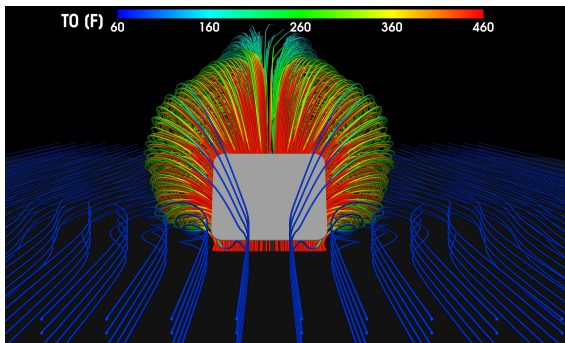
(b) 15°



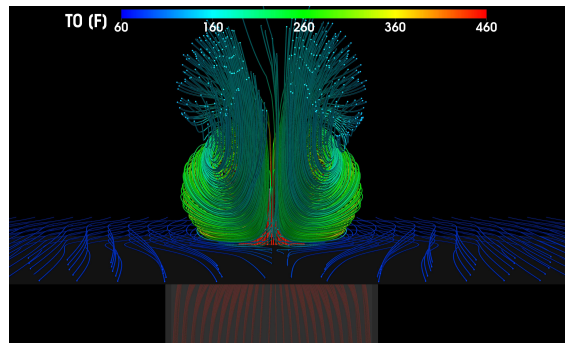
(c) 30°



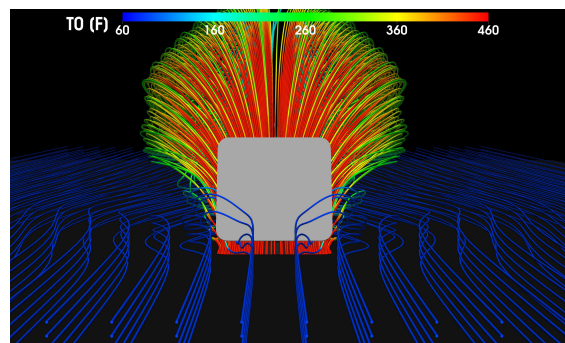
(d) 30°



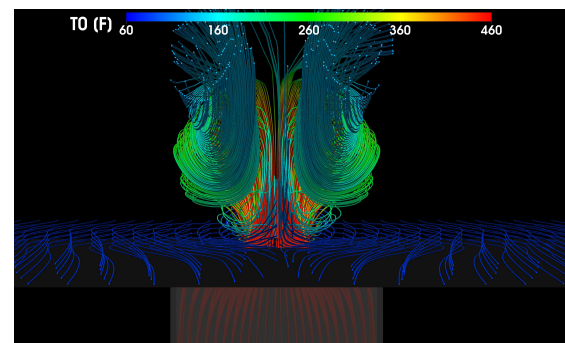
(e) 45°



(f) 45°

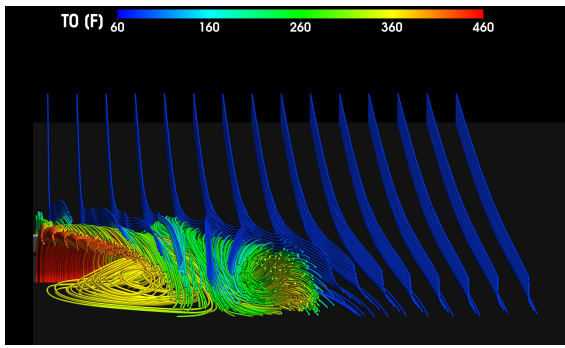


(g) 60°

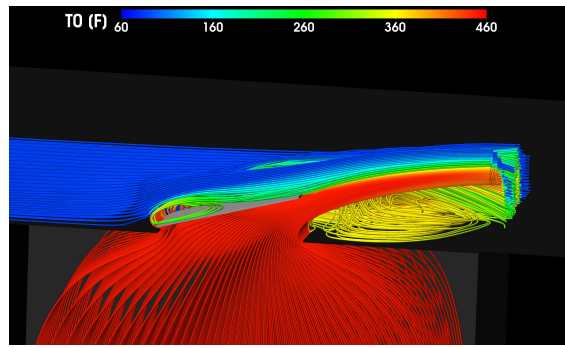


(h) 60°

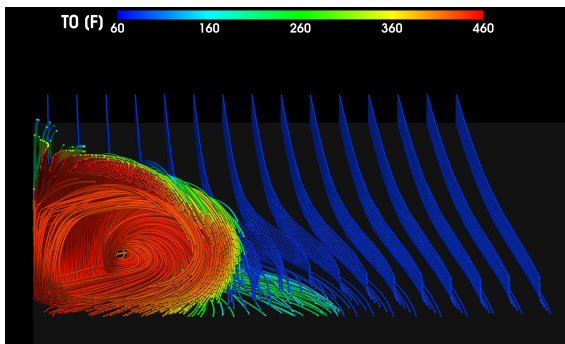
FIGURE 4.33. Streamlines colored by total temperature for varying door angle for Gooseneck-hinge hinge with views looking downstream (left) and upstream (right).



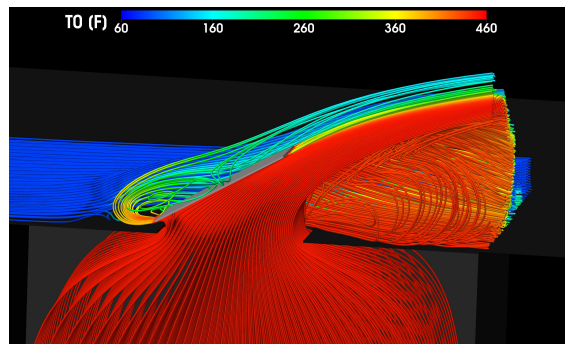
(a) 15°



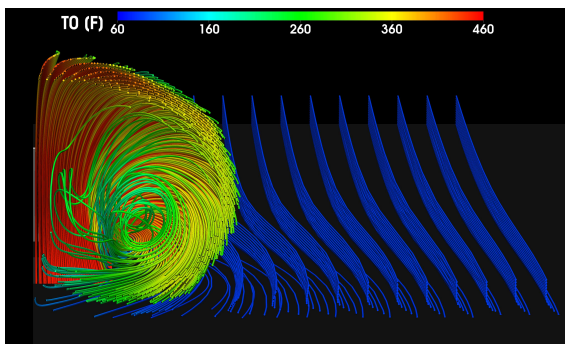
(b) 15°



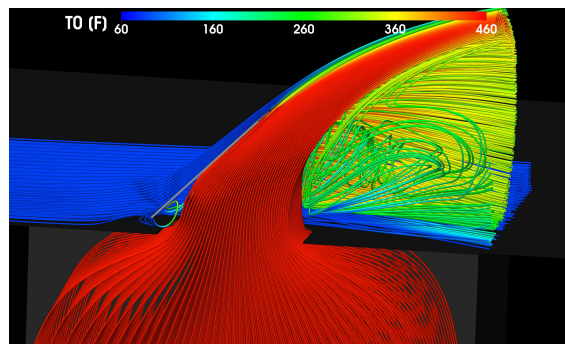
(c) 30°



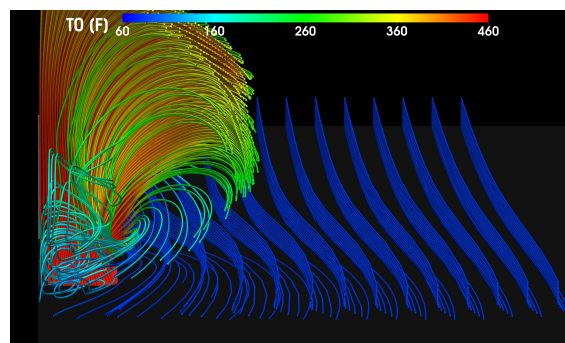
(d) 30°



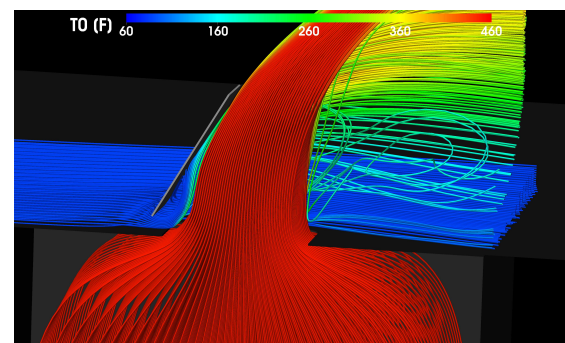
(e) 45°



(f) 45°



(g) 60°



(h) 60°

FIGURE 4.34. Detailed comparison views of streamlines colored by total temperature for varying door angle for Gooseneck-hinge type. Slice view observed looking upstream from a slice 12.5 in. downstream of the trailing edge opening (left) and symmetry plane view (right).

## 4.2. GEOMETRIC COMPARISON STUDY

A subsequent study was performed to investigate the surface temperature characteristics of novel PRD geometric designs for Gooseneck-hinge, Mid-hinge, and Piano-hinge types. The study investigated geometric configurations for Gooseneck-hinge, Mid-hinge, and Piano-hinge types for door angles ranging from  $15^\circ$  to  $60^\circ$  and plenum temperatures of  $T = 450^\circ\text{F}$  and  $T = 1200^\circ\text{F}$ .

4.2.1. GOOSENECK-HINGE GEOMETRIC COMPARISON. The Gooseneck-hinge type was chosen for the Geometric comparison study as it is the most commonly used PRD hinge type. A comparison of four geometric embodiments were examined to investigate the impact of geometric configuration on the surface temperature characteristics of Gooseneck-hinge type PRD designs. Specific details on the geometrical configurations are discussed in Chapter 3. The Gooseneck-hinge geometric comparison study investigated the impact of door shape, corner rounding, and the addition of lateral edge fences on the wall surface temperature characteristics as illustrated in Figure 4.35.

(a) Non-dimensional high-temperature area comparison.

(b) Average non-dimensional wall temperature comparison.

FIGURE 4.35. Surface temperature comparison plots for Gooseneck-hinge types.

Figure 4.35a compares the non-dimensional high-temperature area behavior for door angles ranging from  $15^\circ$  to  $60^\circ$  for the Gooseneck-hinge types at varying plenum temperatures and geometric configurations. The square symbol denotes the baseline rectangular, 1-inch rounded corner, geometry, the diamond symbol represents the trapezoidal geometry with 1-inch rounded corners, the diamond symbol denotes the square corner rectangular geometry, and the star symbol indicates the square corner geometry with lateral edge fences. The symbol color corresponds to variations in plenum temperature. The red symbols correspond to a plenum temperature of  $450^\circ\text{F}$  and the blue symbols correspond to a plenum temperature of  $1200^\circ\text{F}$ . The same convention is followed for Figure 4.35b which compares the non-dimensional average wall temperature as well as for Figures 4.38–4.39.

Figure 4.36 compares total temperature contours on the wall surface for the four Gooseneck-hinge geometric embodiments at  $15^\circ$  (left) and  $45^\circ$  (right). The impacts of door shape, corner rounding, and the addition of lateral edge fences are discussed below.

A comparison of the baseline rectangular and trapezoidal door shapes indicates that the trapezoidal geometry results in a slight increase in high-temperature areas for all door angles investigated. The greatest difference occurs at a door angle of  $30^\circ$  and a plenum temperature of  $1200^\circ\text{F}$ , where the trapezoidal geometry has a high-temperature area that is 1.2 times greater than the baseline rectangular geometry. Figure 4.35b illustrates that the average wall temperature remains similar for door angles less than  $30^\circ$  but is 3 times greater at a door angle of  $45^\circ$  as shown in Figure 4.36. The increased leading edge door width associated with the trapezoidal geometry corresponds to a greater leading edge flow area and leading edge mass flow rate. Additionally, increased blockage created at the leading edge functions to promote more mass flow to exit the lateral edge of the door instead of the

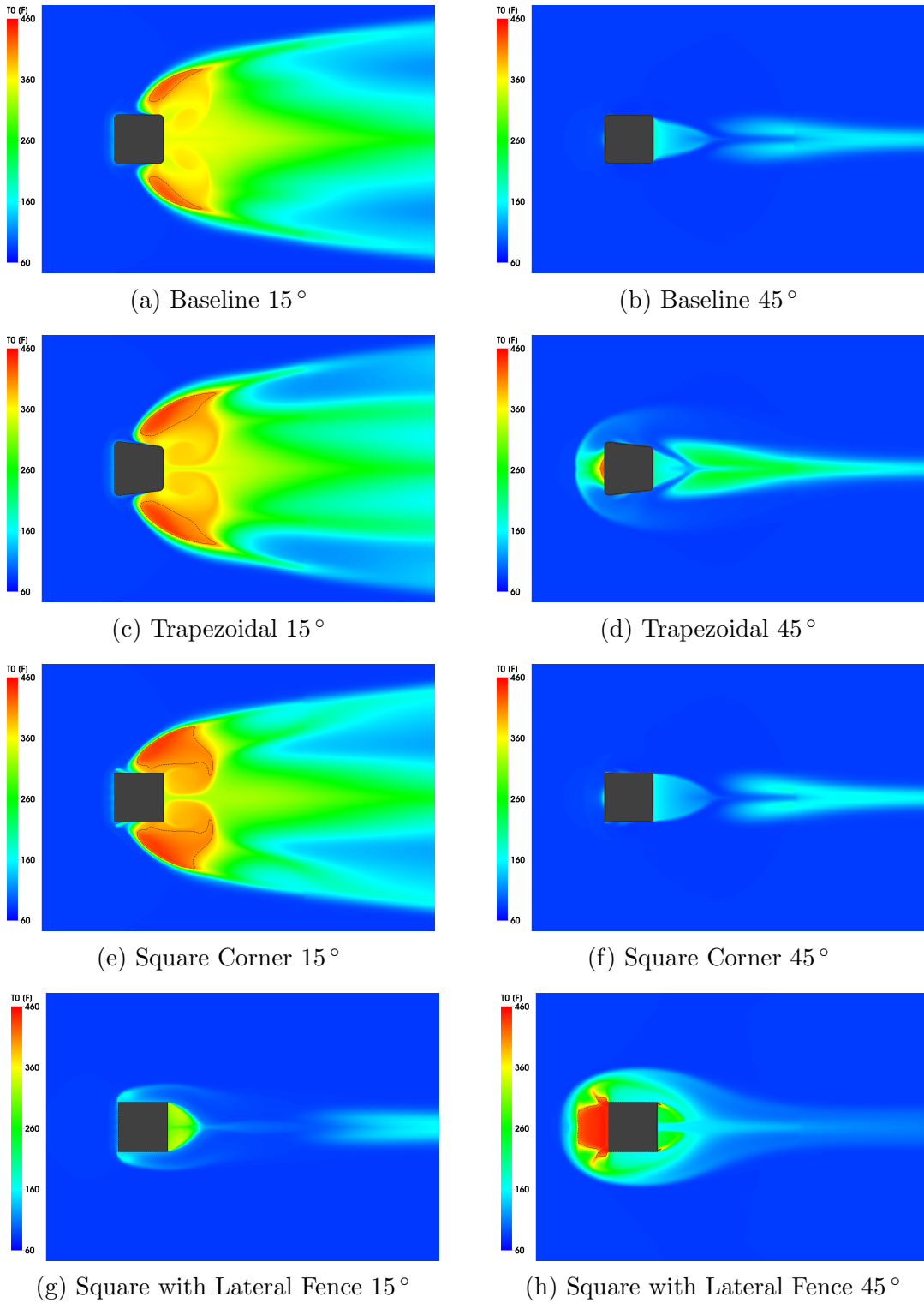
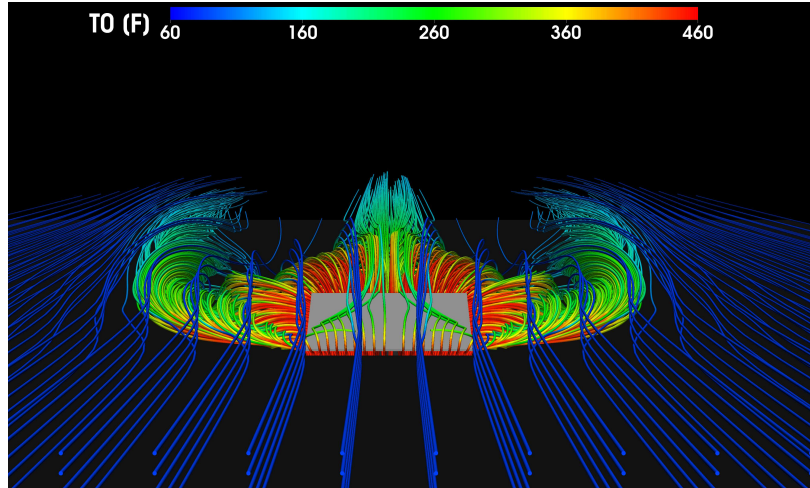


FIGURE 4.36. Total temperature contours for 15° (left) and 45° (right) Gooseneck-hinge geometric hinge type comparison.

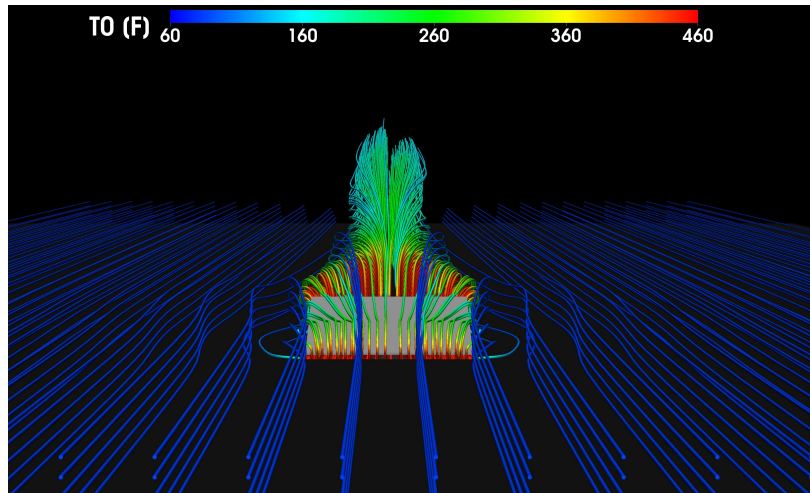
trailing edges. This is illustrated in Figure 4.39 which compares the relative distribution of exit mass flow rate through the leading, lateral, and trailing edge surfaces.

Corner rounding is shown to have a minimal impact on the high-temperature area. For all door angles, the high-temperature area of the square corner geometry is within 2% of the baseline rounded corner geometry. Figure 4.35b illustrates that at a door angle of  $15^\circ$  the square corner geometry average wall temperature is 1.2 times greater than the baseline door geometry. The relative difference in height temperature area is shown in Figure 4.36a and Figure 4.36e where the square corner geometry contributes to a noticeable increase in high-temperature area at  $15^\circ$ . At a door angle of  $30^\circ$ , the square corner geometry results in a 4% reduction in average wall temperature while at door angles of  $45\text{--}60^\circ$  the square corner geometry results in an increase in wall temperature by a factor of 1.5. The increase in surface temperature is attributed to a greater percentage of leading and lateral edge mass flow rate at the  $15\text{--}30^\circ$  door angles where a greater percentage of the total exit flow remains attached to the bottom wall surface. The impact of the corner rounding was unexpected; it was thought that the sharp corners would function to increase thermal mixing and reduce the overall wall surface temperature.

The inclusion of lateral edge fences are shown to have a dramatic impact on the high-temperature area characteristics for door angles less than  $45^\circ$ . The fences act as walls and prevent flow from exiting the lateral edges of the door by redirecting a majority of the flow rearward through the trailing edge opening. The phenomenon is illustrated in Figure 4.37 where streamlines colored by total temperature for a square corner geometry at a  $15^\circ$  door angle with and without lateral edge fences is compared for a plenum temperature of  $450^\circ\text{F}$ .



(a) Square Corner



(b) Square Corner with Lateral Fence

FIGURE 4.37. Streamlines colored by total temperature for comparison of Gooseneck-hinge type square corner geometry at  $15^\circ$  door angle.

At a door angle of  $30^\circ$  and a plenum temperature of  $T = 1200^\circ\text{F}$ , the lateral edge fences function to reduce the non-dimensional high-temperature area by a factor of 12.8, a significant improvement in the wall surface temperatures. The subtle increase in high-temperature area at a door angle of  $45^\circ$  is due to flow exiting through the leading edge surface and remaining attached to the wall as observed in Figure 4.36. Compared to the square corner geometry, the lateral edge fences delay the leading edge reverse flow equilibrium angle from  $39^\circ$  to  $50^\circ$  as illustrated in Figure 4.39. The addition of lateral edge fences

presents a tradeoff between improved wall surface temperatures and a reduction in the exit mass flow rate for all door angles. For door angles less than  $37^\circ$ , more flow exits through the lateral edge surface per unit area as shown in Figure 4.38. The redirection of flow through the trailing edge surface corresponds to an increase in thrust coefficient and hinge moment coefficient. If wall surface temperatures are a primary concern, lateral edge fences should be used but at the expense of a reduction in the total exit mass flow rate and increased hinge moment.

4.2.2. MID-HINGE GEOMETRIC COMPARISON. The Mid-hinge type is commonly used on commercial aircraft today, thus was desired to include in the geometric comparison study. Specific details on the geometrical configurations of Mid-hinge type PRD designs are discussed in Chapter 3. The Mid-hinge geometric comparison investigated the impact of corner rounding and the addition of lateral edge fences on the surface temperature characteristics. A comparison of three geometric embodiments shown in Figure 3.5 were examined.

(a) Minimum Geometric Flow Area

(b) Discharge Flow Ratio

(c) Hinge Moment Coefficient

(d) Corrected Mass Flow Rate

(e) Thrust Coefficient

(f) Non-dimensional Effective Area

FIGURE 4.38. Gooseneck-hinge geometric comparison of discharge, thrust, and moment characteristics.

(a) Leading Mass Flow Distribution

(b) Lateral Mass Flow Distribution

(c) Trailing Mass Flow Distribution

FIGURE 4.39. Gooseneck-hinge geometric comparison of relative mass flow rate distribution.

(a) Non-dimensional high-temperature area comparison.

(b) Average non-dimensional wall temperature comparison.

FIGURE 4.40. Surface temperature comparison plots for Mid-hinge types.

Figure 4.40a compares the non-dimensional high-temperature area behavior for door angles ranging from  $15^\circ$  to  $60^\circ$  for the Mid-hinge types at varying plenum temperatures and geometric configurations. The square symbol denotes the baseline rectangular, 1 inch rounded corner, geometry, the diamond symbol represents the square corner geometry, and the diamond symbol denotes the square corner rectangular geometry with lateral fences. The symbol color corresponds to variations in plenum temperature. The red symbols correspond to a plenum temperature of  $450^\circ\text{F}$  and the blue symbols correspond to a plenum temperature of  $1200^\circ\text{F}$ . The same convention is followed for Figure 4.40b which compares the non-dimensional average wall temperature as well as for Figures 4.43–4.44.

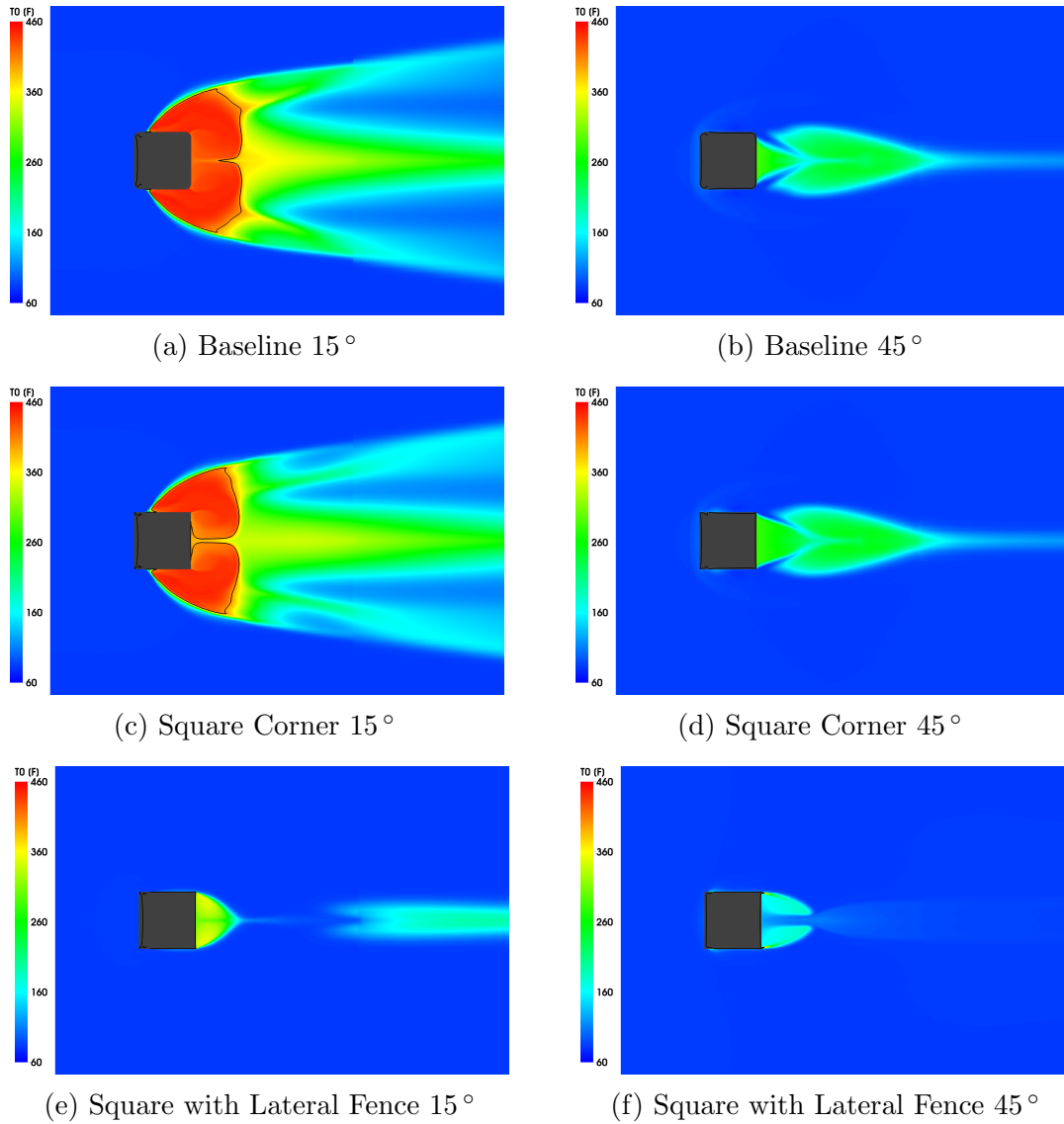


FIGURE 4.41. Total temperature contours for  $15^\circ$  (left) and  $45^\circ$  (right) Mid-hinge geometric hinge type comparison.

Figure 4.36 compares total temperature contours on the wall surface for the three Mid-hinge geometric embodiments at  $15^\circ$  (left) and  $45^\circ$  (right). The impacts of corner rounding and the addition of lateral edge fences are discussed below.

Corner rounding has a noticeable impact on the surface temperature characteristics for the Mid-hinge type. The square corner geometry has a greater non-dimensional high-temperature area but a lower non-dimensional average wall temperature for all door angles as shown Figure 4.40. A comparison of the total temperature contours shown in Figure 4.41,

reflect subtle differences in the high-temperature regions at the  $15^\circ$  door angle but nearly identical behavior at the  $45^\circ$  door angle. The mass flow distribution plots are shown in Figure 4.44 indicate that a greater percentage of the exit mass flow rate was directed through the trailing edge surface. The reduction in lateral edge flow corresponds to a lower average wall temperature. Corner rounding is shown to have minimal influence on the discharge and thrust characteristics but corresponded to an increased hinge moment for door angles less than  $45^\circ$ .

The addition of lateral edge fences is shown to reduce the high-temperature area near the PRD opening by a factor of 18 times at a door angle of  $30^\circ$ . The lateral edge fences redirect the lateral edge flow downstream of the hinge rearward through the trailing edge opening as shown in Figure 4.42. The lack of lateral edge vortices allows the lower temperature freestream gas to flow towards the low-pressure region created aft of the door opening and prevents the high-temperature flow exiting the trailing edge surface from remaining attached to the bottom wall surface as illustrated by the significant reduction in the recirculation created aft of the door opening.

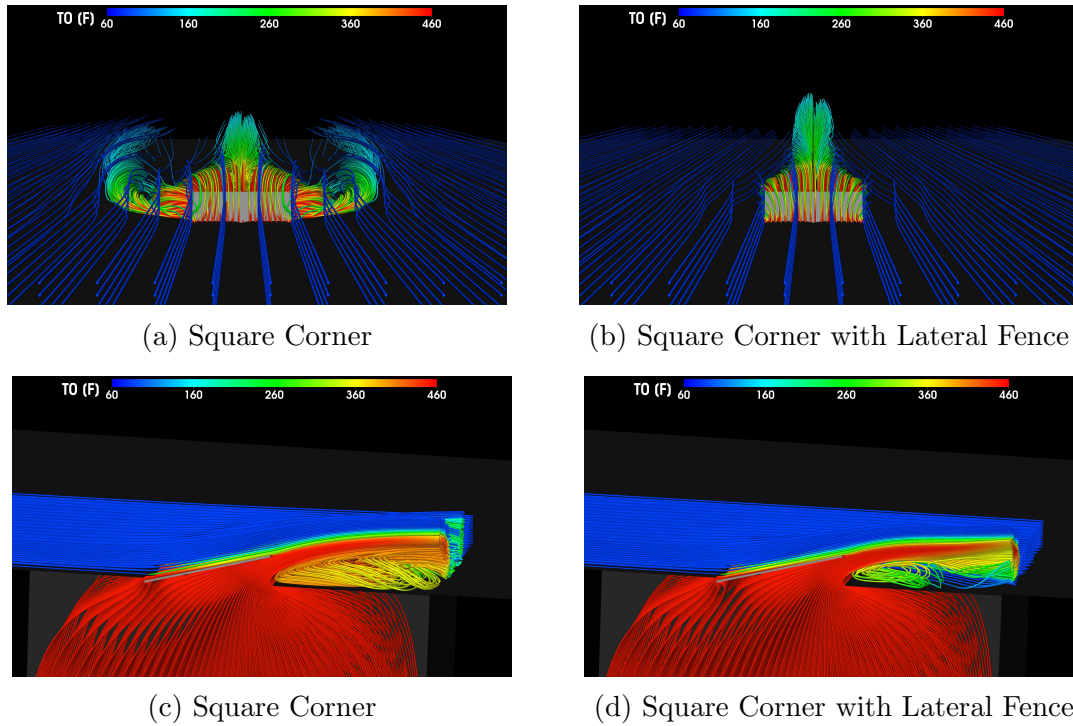


FIGURE 4.42. Streamlines colored by total temperature for  $15^\circ$  door angle for Mid-hinge type geometric embodiments for views looking downstream (top) and from symmetry plane (right).

Similar to the Gooseneck-hinge comparison, the lateral edge fences provide a substantial improvement in high-temperature regions near the door opening. At a door angle of  $30^\circ$  and plenum temperature of  $1200^\circ\text{F}$ , the lateral edge fences result in a reduction in high-temperature area by a factor of 18. The lateral fences for the Mid-hinge type correspond to minimal high-temperature regions on the wall surface. The improved surface temperature characteristics are due in part to the increased trailing edge mass flow rate increases the strength of the trailing edge vortices which lift the exit plenum flow off of the bottom wall of the plenum domain. Without the fences, lateral edge vortices tend to remain attached for door angles less than  $30^\circ$ . The reduction in exit flow area associated with the lateral fences corresponds to a reduced exit mass flow rate and increased hinge moment as shown in

Figure 4.43. Although the total exit mass flow rate is reduced, the lateral edge fences correspond to an increase in DFR, an indication that flow is accelerated through the trailing edge opening. As expected the redirection of flow corresponds to an increased thrust coefficient.

4.2.3. PIANO-HINGE GEOMETRIC COMPARISON. While the Piano-hinge geometry is not commonly used due to challenges associated with the hinge assembly geometry, it was desired to investigate the claims asserted in the 1997 patent awarded to Balzer [20]. The Piano-hinge geometric comparison study investigated the impact of door shape and the addition of lateral edge fence. A rectangle and trapezoid door shapes both with square corners were investigated. Balzer indicated that the trapezoidal geometry featuring lateral edge fences provided the most significant improvement on wall surface temperature behavior. A comparison of four geometric embodiments shown in Figure 3.6 were examined to investigate the impact of door shape and the addition of lateral edge fences on the surface temperature characteristics of Piano-hinge type PRD designs.

(a) Minimum Geometric Flow Area

(b) Discharge Flow Ratio

(c) Hinge Moment Coefficient

(d) Corrected Mass Flow Rate

(e) Thrust Coefficient

(f) Non-dimensional Effective Area

FIGURE 4.43. Mid-hinge geometric comparison of discharge, thrust, and moment characteristics.

(a) Leading Mass Flow Distribution

(b) Lateral Mass Flow Distribution

(c) Trailing Mass Flow Distribution

FIGURE 4.44. Mid-hinge geometric comparison of relative mass flow rate distribution.

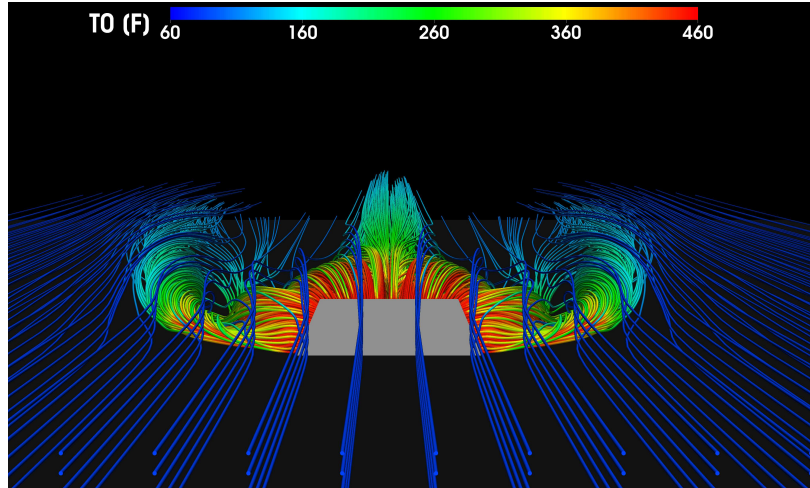
(a) Non-dimensional high-temperature area comparison.

(b) Average non-dimensional wall temperature comparison.

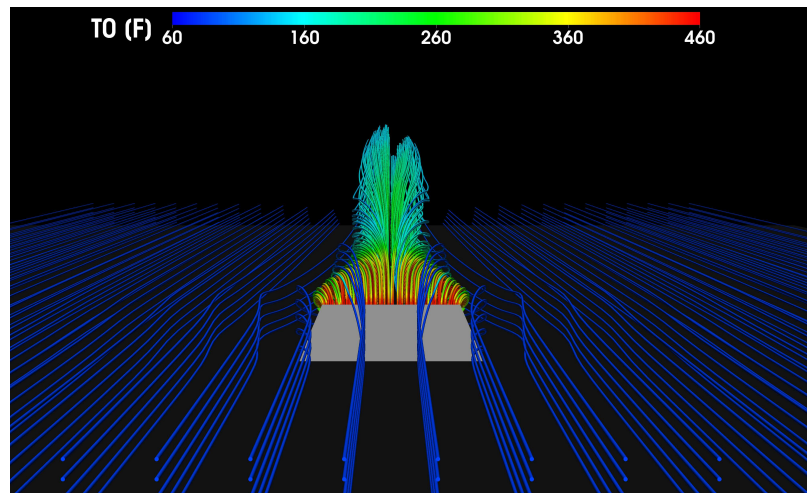
FIGURE 4.45. Surface temperature comparison plots for Piano-hinge types.

Figure 4.45a compares the non-dimensional high-temperature area behavior for door angles ranging from  $15^\circ$  to  $60^\circ$  for the Piano-hinge types at varying plenum temperatures and geometric configurations. The square symbol denotes the square corner rectangular geometry, the diamond symbol represents the square corner geometry with lateral fences, the diamond symbol denotes the square corner trapezoidal geometry, and the star depicts the square corner trapezoidal geometry with lateral fences. The symbol color corresponds to variations in plenum temperature. The red symbols correspond to a plenum temperature of  $450^\circ\text{F}$  and the blue symbols correspond to a plenum temperature of  $1200^\circ\text{F}$ . The same convention is followed for Figure 4.45b which compares the non-dimensional average wall temperature as well as for Figures 4.48–4.49.

Comparison of the square corner rectangular and square corner trapezoidal door shapes indicates that the trapezoidal geometry results in an increase in high-temperature areas for all door angles investigated. The greatest difference occurs at a door angle of  $30^\circ$  and a plenum temperature of  $1200^\circ\text{F}$ , where the trapezoidal geometry has a high-temperature area that is 1.2 times greater than the square corner rectangular geometry. Similar to the Gooseneck-hinge and Mid-hinge geometries, the maximum high-temperature area occurred at a door angle of  $30^\circ$  before decreasing by a factor of 13 at the  $45^\circ$  door angle for the trapezoidal geometry at  $1200^\circ\text{F}$ . Figure 4.45b illustrates that the average wall temperature remain within 2% for all door angles. Figure 4.47 compares the total temperature contours on the wall surface where the behavior of the square corner and trapezoidal geometries exhibit similar qualitative characteristics.



(a) Trapezoid



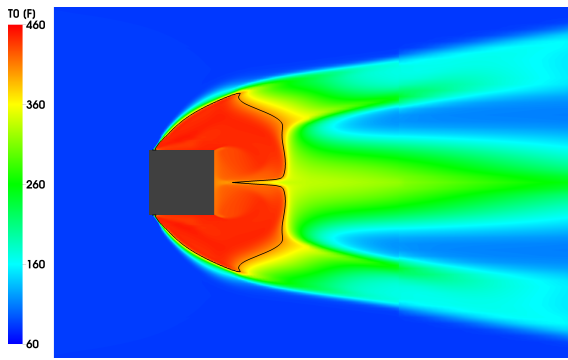
(b) Trapezoid with Lateral Fence

FIGURE 4.46. Streamlines colored by total temperature for  $15^\circ$  door angle for Piano-hinge type geometric embodiments for views looking downstream (left) and upstream (right).

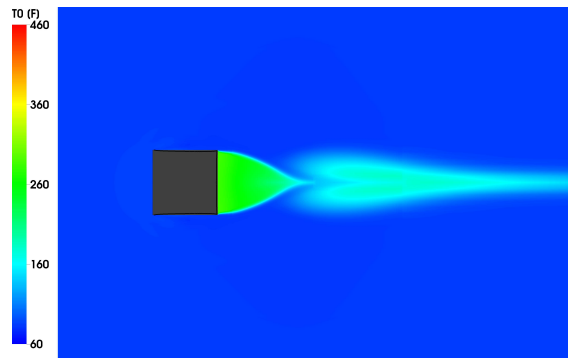
The addition of the lateral edge fences for both the square and trapezoidal geometries corresponds to a dramatic reduction in wall surface temperature. For a door angle of  $30^\circ$  and plenum temperature of  $T = 1200^\circ\text{F}$ , the lateral edge fences provided a reduction in high-temperature area by a factor of 19.1 for the rectangular geometry 20.8 for the trapezoidal geometry. Figure 4.47 highlights the dramatic reduction in high-temperature area. The result is consistent with the result presented by Balzer. Figure 4.46 depicts the impact of the lateral edge surfaces on redirecting the flow rearward. Figure 4.45b illustrates that the lateral fences

result in a greater non-dimensional wall temperature for door angles greater than  $45^\circ$ . The figure illustrates that the fenced geometries maintain a near constant non-dimensional wall temperature near 0.15 for door angles greater than  $30^\circ$ . Figure 4.47 illustrates the dramatic reduction in total temperature on the wall with the addition of the lateral edge fences. The addition of the lateral edge fences provides is very useful for the PRD designer, not only is there a significant reduction in the high-temperature area but a consistent average wall temperature. The lack of severe temperature gradients allows for inexpensive materials to be specified.

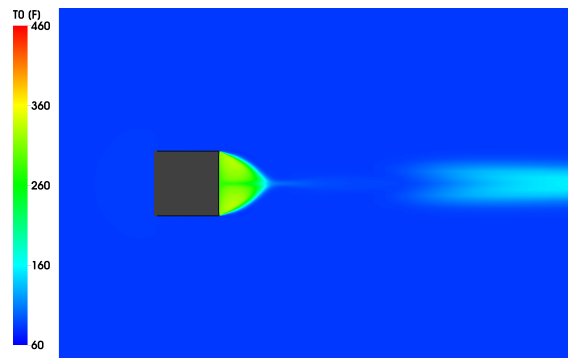
Figure 4.48 illustrates that the addition of lateral edge fences corresponds to a significant change in the discharge, thrust and moment characteristics. The lateral edge fences reduce the total exit mass flow rate and increase the hinge moment for all door angles. The trapezoidal geometry is shown to have a greater impact on the hinge moment and thrust characteristics. Geometries featuring lateral fences result in increasing effective flow area for increasing door angle, unlike the non-fenced geometries.



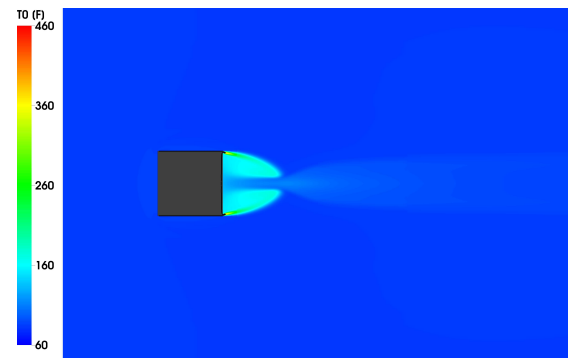
(a) Square Corner  $15^\circ$



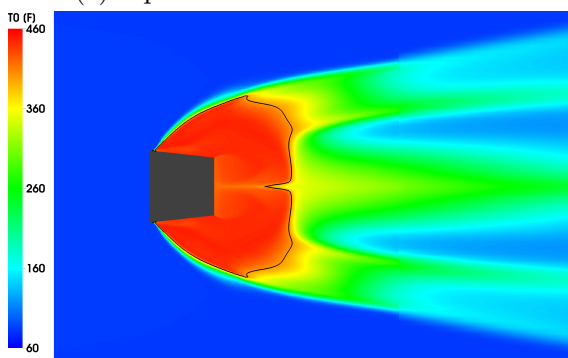
(b) Square Corner  $45^\circ$



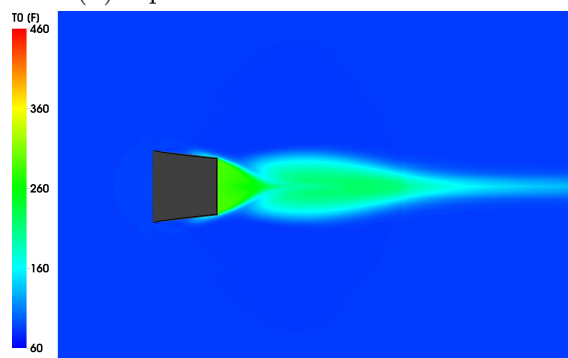
(c) Square with Lateral Fence  $15^\circ$



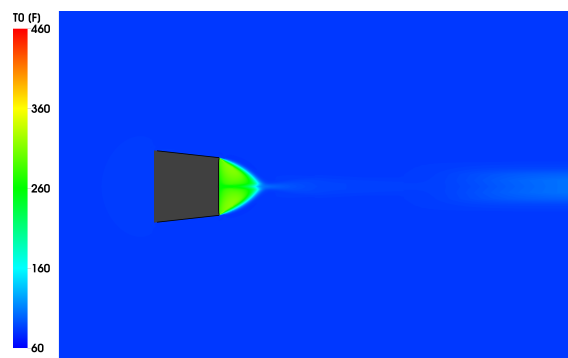
(d) Square with Lateral Fence  $45^\circ$



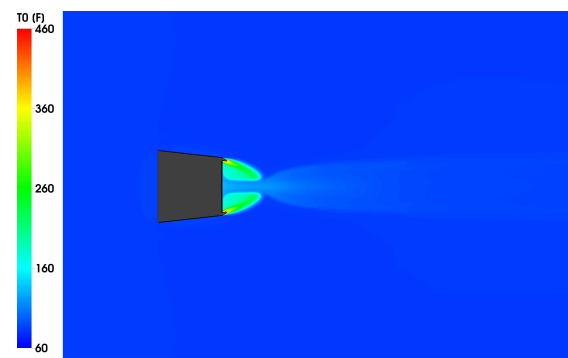
(e) Trapezoidal  $15^\circ$



(f) Trapezoidal  $45^\circ$



(g) Trapezoidal with Lateral Fence  $15^\circ$



(h) Trapezoidal with Lateral Fence  $45^\circ$

FIGURE 4.47. Total temperature contours for  $15^\circ$  (left) and  $45^\circ$  (right) Piano-hinge geometric hinge type comparison.

(a) Minimum Geometric Flow Area

(b) Discharge Flow Ratio

(c) Hinge Moment Coefficient

(d) Corrected Mass Flow Rate

(e) Thrust Coefficient

(f) Non-dimensional Effective Area

FIGURE 4.48. Piano-hinge geometric comparison of discharge, thrust, and moment characteristics.

(a) Leading Mass Flow Distribution

(b) Lateral Mass Flow Distribution

(c) Trailing Mass Flow Distribution

FIGURE 4.49. Piano-hinge geometric comparison of relative mass flow rate distribution.

## CHAPTER 5

# CONCLUSIONS AND FUTURE WORK

### 5.1. CONCLUSIONS

The work presented in this thesis has contributed to an in-depth understanding of the complex flow dynamics associated with variations in freestream, plenum, and geometric configurations and their influence on the aerodynamic performance of a core compartment pressure relief door. The results of the study have been extensively discussed in Chapter 4. Final conclusions are drawn below.

5.1.1. MOMENTS. The primary findings concerning the moment characteristics are listed below.

- (1) The Gooseneck-hinge type was shown to correspond to greater hinge moments due to more exposed door area exposed to the freestream flow.
- (2) Hinge location was shown to have an impact on the moment equilibrium angle with the Mid-hinge type consistently having an equilibrium angle that was  $1^{\circ}$ – $5^{\circ}$  greater than the Gooseneck-hinge type.
- (3) The equilibrium moment angle was shown to increase with increasing freestream altitude and plenum pressure while increasing freestream Mach number decreased it.
- (4) An equilibrium point existed for all door aspect ratios near the equilibrium moment angle of  $47^{\circ}$ .

5.1.2. DISCHARGE. The primary findings concerning the discharge characteristics are listed below.

- (1) Exit mass flow rates were shown to increase with increasing door angle before approaching a maximum.
- (2) Hinge type was shown to have an impact on the discharge characteristics with the Gooseneck-hinge type corresponding to greater exit mass flow rates due to the greater effective flow area.
- (3) Increasing plenum pressure and decreasing plenum temperature corresponded to the greatest exit mass flow rates.
- (4) Freestream altitudes of 25,000 ft. or greater correspond to the greatest discharge coefficient due to the development of shock waves the perimeter of the door opening.
- (5) The leading edge mass flow rate equilibrium angle, which described the angle at which flow no longer exits the leading edge of the door opening, was shown to increase with increasing plenum pressure and freestream altitude, but decreased with increasing freestream Mach number for the Gooseneck-hinge type. Reversed flow was observed for the Mid-hinge type at low plenum pressure, high Mach numbers, and vertically hinge offset conditions.
- (6) Flow exiting the plenum primarily exited through the lateral surface at door angles less than  $23^\circ$  before transitioning to the trailing edge surface. The exit mass flow rate behavior is due to the orientation and direction of the complex three-dimensional vortices that are shed from the lateral and trailing edges of the door.

5.1.3. THRUST. The primary findings concerning the thrust characteristics are listed below.

- (1) The thrust coefficient was shown to decrease with increasing door angle.

- (2) Thrust coefficient was shown to be the most sensitive to plenum pressure, freestream altitude, and freestream Mach number.
- (3) The thrust coefficient equilibrium angle was shown to increase with increasing plenum pressure and freestream altitude and decrease with increasing freestream Mach number.

5.1.4. SURFACE TEMPERATURE. The primary findings concerning the surface temperature characteristics are listed below.

- (1) The maximum non-dimensional average wall surface temperature and non-dimensional high temperature area occurs at a door angle of  $30^\circ$  due to the lateral edge vortices combining with the trailing edge longitudinal vortices.
- (2) At door angles greater than  $30^\circ$ , the trailing edge longitudinal vortices lift the flow off of the bottom wall surface resulting in reduced wall surface temperatures for both hinge types.
- (3) The Gooseneck-hinge type consistently had a greater high temperature area for all door angles due to the leading edge flow behavior and greater lateral edge flow area.
- (4) Increasing plenum temperature and plenum pressure corresponded to greater regions of high temperature flow remaining attached to the wall.
- (5) The addition of lateral edge fences were shown to dramatically reduce the non-dimensional high temperature area near the door opening.
- (6) The trapezoidal Piano-hinge geometry with lateral edge fences was shown to provide a significant reduction in the non-dimensional average wall temperature. The result was consistent with that presented in a patent awarded to Balzer [20].

## 5.2. FUTURE WORK

Several recommendations are proposed to further the understanding of PRD performance and CFD modeling of a core compartment PRD.

- (1) An investigation into geometry more representative of a core casing PRD including the hinge and latch geometry, curvature of the wall surfaces, spring constants and door weights, and the interaction of flow for multiple radially mounted doors.
- (2) A refined parameter study to fully capture the non-linearities that exist in the data set.
- (3) An investigation into the use of the large eddy simulation (LES) turbulence model for a complete domain to gain a better insight into the complicated flow physics downstream of the door and to remove error introduced by using the compressible RANS approach,  $k$ - $\epsilon$  turbulence model, and symmetry boundary condition
- (4) A transient, moving door analysis to gain an understanding of the complex phenomena that occur during a burst duct event.

## BIBLIOGRAPHY

- [1] U. S. D. of the Federal Register, U. S. F. R. Division, and U. S. O. of the Federal Register, *The Code of Federal Regulations of the United States of America*. U.S. Government Printing Office, 1982.
- [2] B. Olmstead and B. Campbell, “Burst duct pressure relief analysis.” Presentation, jul 2014.
- [3] P. R. Pratt, J. K. Watterson, E. Benard, and S. Hall, “Performance of a flapped duct exhausting into a compressible external flow,” in *24th International Congress of the Aeronautical Sciences*, ICAS, aug 2004. ICAS2004-04.2.R.
- [4] J. Banke, “Shhhh! keep it down, please.” online, jul 2009.
- [5] P. Smith, “Beauty or a beast? up close and personal with the 787..” online, aug 2014. <http://www.askthepilot.com/787-beauty-or-a-beast/>.
- [6] A. Vick and U. S. N. A. C. for Aeronautics, *An Investigation of Discharge and Thrust Characteristics of Flapped Outlets for Stream Mach Numbers from 0.40 to 1.30*. Technical note, National Advisory Committee for Aeronautics, 1957.
- [7] P. R. Pratt, J. Watterson, and E. Benard, “Computational and experimental studies of pressure relief doors in ventilated nacelle compartments,” in *CFD and Experiments Symposium*, 2003.
- [8] F. Rogallo and U. S. N. A. C. for Aeronautics, *Internal-flow Systems for Aircraft*. National Advisory Committee for Aeronautics: Report, National Advisory Committee for Aeronautics, 1941.

- [9] P. Dewey and L. A. Laboratory, *A Preliminary Investigation of Aerodynamic Characteristics of Small Inclined Air Outlets at Transonic Mach Numbers*. NACA research memorandum, National Advisory Committee for Aeronautics, 1953.
- [10] P. Dewey, A. Vick, and U. S. N. A. C. for Aeronautics, *An Investigation of the Discharge and Drag Characteristics of Auxiliary-air Outlets Discharging Into a Transonic Stream*. National Advisory Committee for Aeronautics technical note, National Advisory Committee for Aeronautics, 1955.
- [11] A. D. Young, J. H. Patterson, and J. L. Jones, “Aircraft excrescence drag,” Tech. Rep. AG-264, AGARD, Jul 1981.
- [12] P. R. Pratt, J. Watterson, and E. Benard, “Computational and experimental studies of pressure relief doors in ventilated nacelle compartments,” 2003. Presentation.
- [13] E. Benard, J. K. Watterson, R. Gault, and J. Richardson, “Review and experimental survey of flapped exhaust performance,” *J Aircraft*, vol. 45, no. 1, pp. 349–352, 2008.
- [14] G. Vedeshkin, A. Dubovitskiy, D. Bondarenko, and O. Verseux, “Experimental investigations of hydraulic devices performance in aviation engine compartment,” in *28th International Congress of the Aeronautical Sciences*, ICAS, 2012.
- [15] O. Verseux and Y. Sommerer, “New challenges for engine nacelle compartments pressure and thermal loads management with aircraft engine evolution,” in *29th Congress of the International Council of the Aeronautical Sciences*, ICAS, 2014.
- [16] R. J. Siems and A. B. Voorhees, “Blow-out safe aircraft doors,” 1956.
- [17] P. C. Abeel, “Access and pressure release door latch mechanism,” 1971.
- [18] K. A. Pearson and M. D. Moorhouse, “Pressure relief panel for aircraft powerplant,” 1980.

- [19] R. Bubello and J. L. Ream, “Ventilation system for a nacelle,” 1989.
- [20] R. Balzer, D. T. Jensen, and M. L. Sangwin, “Flow control apparatus for gas turbine installation pressure relief doors,” 1997.
- [21] M. E. Armstrong, M. D. Jones, and K. W. Dunstan, “Spring loaded pressure relief door,” 2013.
- [22] M. E. Armstrong, “Spring loaded pressure relief door for a nacelle cowl,” 2012.
- [23] C. R. Tuchimaa and S. D. Palsh, “Aircraft pressure management system,” 2014.
- [24] M. Technologies, “<http://www.metacomptech.com/>.” Online, 2016.
- [25] C. P. T. Groth, “Turbulence modelling.” AER1310 Course Notes.
- [26] D. Wilcox, *Turbulence Modeling for CFD*. DCW Industries, 1998.
- [27] S. B. Pope, *Turbulent Flows*. Cambridge University Press, 2011.
- [28] H. Childs, E. Brugger, B. Whitlock, J. Meredith, S. Ahern, D. Pugmire, K. Biagas, M. Miller, C. Harrison, G. H. Weber, H. Krishnan, T. Fogal, A. Sanderson, C. Garth, E. W. Bethel, D. Camp, O. Rübél, M. Durant, J. M. Favre, and P. Navrátil, “VisIt: An End-User Tool For Visualizing and Analyzing Very Large Data,” in *High Performance Visualization—Enabling Extreme-Scale Scientific Insight*, pp. 357–372, Oct 2012.
- [29] P. Inc., “<http://www.pointwise.com/>.” Online, 2016.